NANO-DOMAIN ANALYSIS VIA MASSIVE CLUSTER SECONDARY ION MASS SPECTROMETRY IN THE EVENT-BY-EVENT MODE

A Dissertation

by

VERONICA TIFFANY PINNICK

Submitted to the Office of Graduate Studies of
Texas A&M University
in partial fulfillment of the requirements for the degree of

DOCTOR OF PHILOSOPHY

December 2009

Major Subject: Chemistry

NANO-DOMAIN ANALYSIS VIA MASSIVE CLUSTER SECONDARY ION MASS SPECTROMETRY IN THE EVENT-BY-EVENT MODE

A Dissertation

by

VERONICA TIFFANY PINNICK

Submitted to the Office of Graduate Studies of
Texas A&M University
in partial fulfillment of the requirements for the degree of

DOCTOR OF PHILOSOPHY

Approved by:

Chair of Committee,	Emile A. Schweikert
Committee Members,	Wayne Goodman
	David H. Russell
	Andreas Holzenburg
Head of Department,	David H. Russell

December 2009

Major Subject: Chemistry

ABSTRACT

Nano-Domain Analysis via Massive Cluster Secondary Ion Mass Spectrometry in the Event-by-Event Mode. (December 2009)

Veronica Tiffany Pinnick, B.A., Minot State University

Chair of Advisory Committee: Dr. Emile A. Schweikert

Secondary ion mass spectrometry (SIMS) is a surface analysis technique which characterizes species sputtered by an energetic particle beam. Bombardment with cluster projectiles offers the following notable advantages over bombardment with atomic ions or small clusters: enhanced emission of molecular ions, low damage cross-section, and reduced molecular fragmentation. Additionally, in the case of Au_{400}^{4+} and C_{60}^{+} impacts, desorption originates from nanometric volumes. These features make clusters useful probes to obtain molecular information from both nano-objects and nano-domains. The "event-by-event bombardment/detection mode" probes nano-objects one-at-a-time, while collecting and storing the corresponding secondary ion (SI) information.

Presented here are the first experiments where free-standing nano-objects were bombarded with keV projectiles of atomic to nanoparticle size. The objects are aluminum nano-whiskers, 2 nm in diameter and ~250 nm in length. Au_{400}^{4+} has a diameter of ~2 nm, comparable to the nominal diameter of the nanowhiskers. There are notable differences in the SI response from sample volumes too small for full projectile energy deposition. The whisker spectra are dominated by small clusters—the most

abundant species being AlO^- and AlO_2^-. Bulk samples have larger yields for AlO_2^- than for AlO^-, while this trend is reversed in whisker samples. Bulk samples give similar abundances of large SI clusters, while whisker samples give an order of magnitude lower yield of these SIs. Effective yields were calculated in order to determine quantitative differences between the nano-objects and bulk samples.

The characterization of individual nano-objects from a mixture is demonstrated with negatively charged polymer spheres that are attracted to and retained by the nano-whiskers. The spheres are monodisperse polystyrene nanoparticles (30nm diameter). Our results show that the event-by-event mode can provide information on the nature, size, relative location, and abundance of nano-objects in the field of view. This study presents the first evidence of quantitative molecular information originating from nano-object mixtures.

Biologically relevant systems (solid-supported lipid bilayers) were also characterized using Au_5^+, Au_{400}^{4+} and C_{60}^+. Organization-dependent SI emission was observed for phosphocholine bilayers. Lipid domain formation was also investigated in bilayers formed from cholesterol and a mixed lipid system. Trends in the correlation coefficient suggest that cholesterol segregates from the surrounding lipid environment during raft formation.

DEDICATION

To

Mom and Dad,

The Cavallo's and Pinnick's,

But most of all,

To Aaron

ACKNOWLEDGEMENTS

I would like to take this opportunity to thank the many people who have provided their support for me during my years as a graduate student at Texas A&M University. First and foremost, I would like to thank my advisor, Dr. Schweikert, for his encouragement, patience, and advice. To me, you are the model of a scientist—knowledgeable, open-minded, and able to communicate complex concepts "pedagogically." Thank you for knowing exactly how much to push me to keep me moving forward.

To Dr. Verkhoturov, thank you for having endless enthusiasm for our "very strong results." It always amazed me how you could derive a mathematical equation for anything. To Dr. Guillermier, your dedication and enthusiasm for science has been an inspiration to me. I hope one day you start your own lab—you are a great mentor to young scientists. To Dr. Della-Negra, I thank you very much for your help with the gold instrument. Sometimes that instrument was "not so obvious."

To past Schweikert group members, thank you for taking me in and showing me the mass spec ropes. To Dr. Hager, Georgie, it was great to work with you during my first few years. I always enjoyed our interesting conversations—mostly I enjoyed your poking at Jay. I wish you and Sara (and the puppies) all the best. To Dr. Locklear, thanks for always having a wordy description of even the simplest concepts. To Dr. Li, thanks for keeping Marcus and me afloat after George and Jay graduated. I also appreciate all the mechanical help you've given me on the Miata.

The past five years would not have been the same without Mr. Marcus. We've seen a lot of the country together: from hiking in Denver, to clubbing in Miami, to standing in the rain at the Liberty Bell. I will always cherish the memories we've shared. You're a great friend. Maybe one day, I'll get to eat authentic Sri Lankan food in Colombo. To Li-Jung, thank you for teaching me all the Chinese phrases, sorry if our pronunciation hurt your ears. Thanks also for all the tasty treats you introduced us to. I wish you luck finishing your graduate work. To Mikey, thanks for introducing me to Aggie baseball and for always being willing to go out to lunch. Please don't go blind looking for electron spots. To Daniel, you have amazed me with how quickly you learned all about the gold instrument. Unfortunately, that means that you get to inherit all the problems! Thanks for always being such a gracious host and always having the bonfire ready. To Dr. Fernandez-Lima, thanks for all your help during crunch time. To Atashi, I wish you all the best with graduate school. Thanks to Dennis James for always being ready to throw some strange sample into your XRF instrument for me. I am amazed that we always got something interesting out of them. To Mike Raulerson, thanks for all the fun political discussions, even if we could never agree.

To my family, the Cavallo's and Pinnick's who have always encouraged me to pursue my education and have always been there with encouragement and support, I cannot thank you guys enough. In particular, Pop, you've been an inspiration to me. And finally, to my husband, Aaron, your love and patience, your humor and perspective, and your endless belief in me have given me the strength to accomplish this goal. Thank you for everything. I could not have done any of this without you—I love you.

TABLE OF CONTENTS

CHAPTER Page

LIST OF FIGURES

FIGURE Page

FIGURE Page

FIGURE Page

LIST OF TABLES

CHAPTER I

INTRODUCTION

Secondary ion mass spectrometry (SIMS) involves the use of energetic projectiles (primary ions) to bombard analyte surfaces, which induces the sputtering of secondary species (electrons, photons, atomic and polyatomic ions, and neutrals). A general schematic for the SIMS experiment is presented in figure 1-1. The secondary species emitted after primary particle impacts derive from the topmost layers of a sample surface and are separated based on their mass to charge ratio. This technique can provide molecular and isotopic information from analyte surfaces, as well as depth profiling information obtained from sputtering overlayers. Less than a decade ago, secondary ion mass spectrometry (SIMS) appeared to have reached its maturity as a surface analysis technique, mainly focusing on the analysis of thin films and semiconductor materials[1]. Many improvements, including the use of cluster projectiles, have allowed SIMS to find increasing application in molecular imaging and biological investigations. The aim of this chapter is to briefly review the principles of secondary ion mass spectrometry as it relates to the research presented here.

Dynamic vs. Static Regime

Secondary ion mass spectrometry can be classified into two categories based on the primary ion dose delivered to the sample surface. When the dose is higher than ~10^{12} ions/cm^2, this mode of operation is termed “dynamic” SIMS.

This dissertation follows the style of *Analytical Chemistry*.

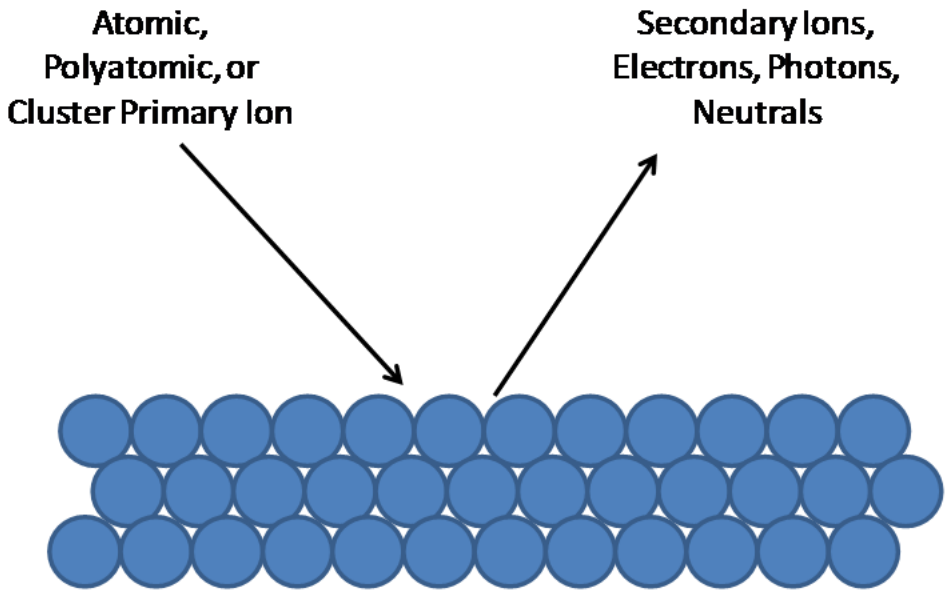

Figure 1-1. General schematic of secondary ion mass spectrometry process.

Studies involving dynamic SIMS utilize high fluence ion beams to sputter material from a small area. Layers of material are removed and secondary ions are monitored to obtain three-dimensional chemical information (depth profiling)[2]. Secondary ions produced from this technique undergo extensive fragmentation, which confine most studies to elemental and isotopic distribution studies.

When the dose of primary ions on analyte surfaces is reduced to less than 10^{12} ions/cm^2, this mode of operation is termed "static" SIMS. Studies of this nature aim to minimize sample destruction by sampling only the topmost layers of the sample surface. In this case, the dose is small enough that the probability of sampling a damaged area is very low. Beam damage and beam mixing effects are minimized, which allow for the reliable detection of larger, more analytically significant molecular species from sample surfaces. Furthermore, the secondary ion information can be traced to the area perturbed by impacting projectiles[3]. While this technique is attractive for its non-destructive nature, the low dose of primary ions imposes limitations due to the inefficiency of primary ions to produce significant secondary ion signal. A major innovation in improving the efficiency of secondary ion production in SIMS is the utilization of cluster projectiles.

Cluster-SIMS

In recent years, polyatomic ions have been increasingly used as primary projectiles in SIMS, due to the non-linear increase in secondary ion yield they produce. This observation, termed the "cluster" or "collective" effect dates back to the 1960's, when Rol et al. and Grønlung et al. found that impacting metallic surfaces with small

clusters (e.g. KI^+) produced larger sputter yields than the sum of that obtained from bombardment of individual constituents alone(e.g. K^+ and I^- alone)[4, 5]. Theoreticians Anderson and Bay, and Thompson et al. also observed large increases in the total sputter yield when bombarding surfaces with diatomics and triatomics rather than atomic projectiles[6-8].

The performance of SIMS depends on the efficiency of a projectile to produce secondary ions. As such, it is useful to define a term to compare the efficiencies of the projectiles used for various sample surface analyses. One measure of the performance of a projectile is the enhancement factor[9], κ, which is defined as

$$\kappa = \frac{Y_{An}(E)}{nY_A(E/n)} \qquad \text{Eq. 1-1}$$

where $Y_{An}(E)$ is the yield of ions under cluster (A_n) projectile bombardment with kinetic energy *E*, and $Y_A(E/n)$ is the yield of ions under atomic (A) projectile bombardment with kinetic energy *(E/n)*. This relationship implies that comparisons should be made between projectiles with the same impact velocities and that κ values greater than one show "supralinear" enhancement.

Using this concept, in 1989 Appelhans and Delmore were among the first to demonstrate that cluster projectiles could offer not only increased sputter yields, but also increased secondary ion yields. The authors investigated organic surfaces with SF_6^- and SF_6^0 projectiles and compared the emission to that obtained from Cs^+ bombardment at the same energies. Results showed that enhancement factors of 10-25 were obtained from the cluster projectiles over the atomic projectile. Further, the damage induced by

the projectile (as measured by the disappearance of molecular signal over time) decreased with cluster projectile use[10].

In the same year, similar work was being conducted at Texas A&M and the Institut de Physique Nucleaire at Orsay (France). The first comprehensive studies on the effect of the number of projectile constituents on secondary ion yields were published by Blain, et al. The investigations involved the bombardment of a variety of surfaces with complex projectiles (e.g. $(CsI)_nCs$, n=1,2) of 5-28 keV impact energies. The authors found that secondary ion yields increase proportional to the square of the projectile momentum. They also found that this enhancement is more pronounced for molecular secondary ion species than it is for atomic secondary ions[11].

In 1991, Benguerba et al. extended enhancement studies to include large gold projectiles Au_n^{q+} (n=1-5, q=1,2). Again it was found that secondary ion yields strongly increase with the increasing number of constituents in a projectile[12]. Studies showed, however that yield enhancement is not supralinear for projectiles with greater than ~9 constituents. Similar observations were made using carbon clusters by Boussofian-Baudin et al. who compared enhancement effects from MeV C_{10} and C_{60} cluster projectiles[13]. Van Stipdonk et al. studied the secondary ion yields from phenylalanine and CsI targets bombarded by $C_{60}^+$and Cs^+ with the same primary ion energy[14]. The authors report secondary ion yields for these targets are 5-80 times higher when samples were bombarded with C_{60}^+ as compared to the monatomic Cs^{+15}.

In 1994, Szymczak and Wittmaack investigated the role of the charge state of both the impacting projectile as well as the sputtered ions on the enhancement factor[16].

They found that the enhancement is not strongly related to the charge state of the primary ion, but that the enhancement is more pronounced for negative secondary ions than for positively charged ions.

Vickerman et al. greatly expanded SIMS research using C_{60} projectiles by developing and commercializing an effusion source in 2003[17, 18]. The source could produce $C_{60}^{1,2+}$ at energies up to ~25 keV. Major innovations in depth profiling have been accomplished utilizing this projectile due to the decreased damage caused to underlayers via C_{60} bombardment[19-24].

In 2004, Tempez et al. reported massive cluster emission from a gold liquid metal ion source. Cluster sizes were produced as Au_n^{q+} (n=1-1000, q=1-10)[25, 26]. Authors report molecular ion yield enhancement for Gramicidin of ~1000 for Au_{400}^{4+} when compared to Au^+. Guillermier et al. observed yield enhancement of Au_{400}^{4+} over that of Au_5^+ for glycine targets[27]. Intensities of molecular peaks (Gly_n, $1 < n < 4$) are ~5 times larger for Au_{400}^{4+}. The intensity of the CN^- fragment is also considerably enhanced with such a projectile, i.e ~ 10 times.

Much larger clusters have been utilized for SIMS analysis than the projectiles described above. Mahoney et al., for example, has produced massive glycerol projectiles with masses greater than 10^7 amu and more than 100 charges[28, 29]. Though the process demonstrated to be efficient (having low chemical noise and good signal-to-noise ratio), studies of glycerol impacts have been limited to few research groups[2]. Massive noble gas clusters (e.g. $Ar_{1\text{-}2000}^+$) have been utilized by Matsuo et al. in molecular dynamic simulations as well as for the analysis of depth profiling on silicon[30,

[31]. Argon clusters showed one to two orders of magnitude greater sputtering yields than atomic argon.

Coincidence Ion Mass Spectrometry

A coincidence experiment involves the detection of several different types of emission that originate from a particular event. The use of coincidental signals is not a new concept—nuclear scientists, for example, have monitored coincidental emission from the nuclear decay of radioisotopes for decades. Background noise can be reduced by using two or more photomultiplier tubes to monitor the decay[32]. Very few mass spectrometry groups, however, have taken advantage of coincidence counting to provide information complementing conventional analysis. Coincidence ion mass spectrometry (CIMS) is a derivative technique of SIMS in which statistical correlations of secondary ions emitted from a single primary projectile impact can give insight into the chemical composition of nano-environments[33]. Since the signal derives from the emission volume of a single projectile, co-emitted secondary ions must originate from molecules co-located within the nano-volume. CIMS has been used in metrology of semiconductor material[34] and to study various organic samples such as gramicidin S as well as the MALDI matrix 2,5-dihydroxybenzoic acid[35]. LeBeyec et al. use CIMS for investigations of metastable secondary ion decay[36]. Schweikert et al. have also been able to utilize this technique for the investigation of ion metastability[37-39] as well as for monitoring the chemical homogeneity of surfaces[37, 40, 41]. However, the literature remains sparse on the subject.

In order to obtain an understanding of the morphology and chemical homogeneity of the sample surface, it is useful to monitor coincidental emission of secondary ions. The event-by-event bombardment/detection mode used here allows one to not only monitor ions in coincidence with one another, but also to monitor ions in coincidence with the electrons produced from the projectile impact. As such, it is possible to obtain information from single projectile impacts, allowing for co-localization of chemical species from the region perturbed by the impact.

Secondary Ion Multiplicity

When coincidental secondary ion information is sought, it becomes increasingly important that projectile impacts result in multiple ion emission. Secondary ion multiplicity be defined in two ways. One definition of the SI multiplicity refers to the number of secondary ions of any type detected per desorption event. A more restrictive, and perhaps more informative definition of SI multiplicity refers to the number of ions detected per projectile impact when co-emitted with a selected secondary ion. Beyond coincidental studies, increases in secondary ion multiplicity may also produce an increase in analytically significant signal from the sample surface.

Secondary ion multiplicity has been shown to increase as a result of cluster bombardment as opposed to atomic ion bombardment. Zubarev et al. found that impacting targets with large bio-molecules of differing mass and energies changed the observed multiplicity of secondary ions[42]. Indeed, authors determined that higher mass projectiles produced larger multiplicities when compared to lower mass projectiles at equal energy. They also determined that multiplicity increases with increasing projectile

energy. In these studies, the authors monitored ions of any m/z to define the SI multiplicity.

Multiple ion emission has also been extensively studied by Schweikert and co-workers. Theory-based discussion of the concept of secondary ion multiplicity in the event-by-event mode was discussed by da Silveira, et al[43]. Here the statistical model of multiple ion emission is discussed and the randomness of emission is analyzed. Experimental studies focused on characterizing secondary ion multiplicities from a wide range of projectile sizes and energies. Rickman et al. investigated multiplicity from Au clusters (Au^+, Au_3^+, Au_9^+, Au_{400}^{4+}) at energies ranging from 26 to 134 keV[44, 45]. Results suggest the same trend as those previously discussed: larger more energetic projectiles increase multi-ion emission. For example, the author reports for a phenylalanine surface, 28.6 keV Au_9^+ produces ~1 Phe- molecule per impact, whereas 134.6 keV Au_{400}^{4+} produces ~10 Phe- molecules. The secondary ion multiplicities for carbon clusters C_{60}^+, $C_{24}H_{12}^+$, and $C_{60}F_{40}^+$ were reported by Locklear et al. The author compares carbon cluster emission to that from atomic Au bombardment, again showing that clusters were 3-4 times more efficient at producing multiple ion emission.

Nano-Analysis in Mass Spectrometry

The need for obtaining molecular information from individual nano-sized components is a challenge in many scientific fields. For example, the reliable production of microelectronics devices requires the ability to identify and quantify individual nano-dopants or contaminants[46]. In biology, toxicology and drug delivery studies are concerned with localization of nanoparticles in subcelluar components within

this size regime[47]. The characterization of single nano-objects beyond their size and shape, however, is limited by the capabilities of current analytical techniques[48]. Few studies, however, focus on the characterization of individual nano-objects, particularly ones which are free-standing in nature. Johnston et al. analyze individual aerosol particles in environmental mass spectrometry[49] using custom-build LDI instruments. These particles are ablated by the laser, and thus only provide elemental and isotopic information. The goal of this work is to utilize surface mass spectrometry to obtain molecular information from individual nano-domains and nano-objects. This will require and understanding of the capabilities and limitations of SIMS for nano-analysis, a topic which is not defined in the literature. Further, it will require an understanding of how SIMS analysis of confined-volume samples compares to bulk analysis.

Present Study

In this dissertation, two main topics are investigated and discussed: 1) the application of cluster ToF-SIMS to the analysis of model lipid membranes, and 2) the application of cluster ToF-SIMS for the characterization of individual nano-objects.

The first topic was investigated using solid-supported lipid bilayers which are widely used in proteomics and biosensing to mimic behavior observed in biological membranes. The goals of the studies were two-fold: a) to devise a methodology for preparation of bilayers for vacuum environment, and b) to investigate domain formation in the bilayers. Bilayer organization was investigated in dehydrated samples with and without polyethylene glycol protection. Bilayers were analyzed in the positive ion mode using Au_5^+ and in negative ion mode using Au_{400}^{4+}. Bilayer domain formation (lipid

rafts) were analyzed in a mixed lipid/cholesterol system in the negative ion mode using C_{60}^{+}. Both studies were conducted in the event-by-event bombardment/detection mode, which provides the basis for calculation of secondary ion yields as well as correlation coefficients.

The second topic was investigated using free-standing nano-objects. The goals of the studies were two-fold: a) to determine if SIMS signal from nano-objects can be compared to bulk reference signals, and b) to determine if individual nano-objects can be analyzed in a mixture. Studies were carried out using bulk aluminum oxide samples (foil and aluminum oxide coated silicon wafer) and aluminum oxide nano-objects (nano-whiskers and nanoparticles). Samples were investigated with a suite of Au projectiles (Au_n^{q+}, $1 \leq n \leq 400$, $1 \leq q \leq 4$) in the negative ion mode. Nano-object mixtures were prepared from alumina nano-whiskers and polystyrene nanospheres. These mixtures were analyzed with Au_{400}^{4+} in the negative ion mode. Both studies were carried out in the event-by-event bombardment/detection mode which allowed for the calculation of correlation coefficients, effective yields and the number of effective impacts on a component.

CHAPTER II

INSTRUMENTATION AND METHODOLOGY

The following chapter describes two time-of-flight (ToF) SIMS instruments which were used for the studies described in chapters III through V, including hardware, detection and supporting electronics. Each instrument has two main components: a primary ion leg for production, focusing and delivery of single projectile impacts onto a target; and a secondary ion leg for extraction, separation and detection of the ejecta emitted from the primary ion impacts on the target. The specifications for each instrument will be outlined in more detail below. This chapter also outlines the current state of method development for the positive ion mode.

C_{60} Effusion Source Mass Spectrometer

The C_{60} effusion source mass spectrometer was used in the analysis of the lipid bilayers presented in chapter III. A detailed description of the instrument is available elsewhere[50, 51].

A schematic of the instrument is presented in figure 2-1. Briefly, the C_{60} effusion source is housed in a custom-built stainless steel chamber. The ultimate pressure in this chamber is $1x10^{-6}$ Torr when not in use, ~$5x10^{-6}$ Torr when the source is operating. This vacuum is maintained by a 60 L/s turbomolecular pump (Pfeiffer Vacuum, Nashua, NH) backed by an 8 CFM two-stage rotary vane mechanical pump (Varian Inc., Palo Alto, CA). The C_{60} effusion source designed and manufactured in our lab is similar in design to the C_{60} source developed by Vickerman's group[17, 18]. C_{60}

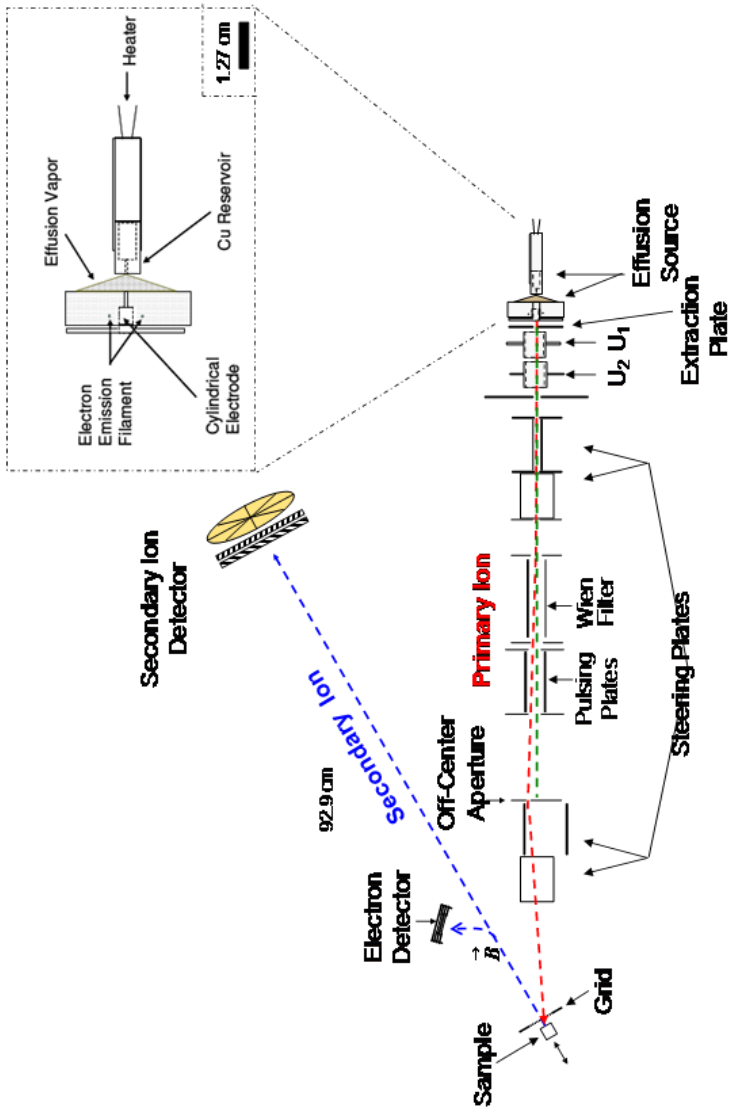

Figure 2-1. Schematic of the C_{60} effusion source mass spectrometer (source region drawn to scale, instrument not to scale).

powder (Sigma Aldrich, Milwaukee, WI) is heated in a copper reservoir to its sublimation temperature (~450°C). The C_{60} vapor effuses through an aperture in the reservoir into the ionization chamber. A tungsten wire (0.1mm diameter, Alfa Aesar, Ward Hill, MA) is set ~5 mm from the cylindrical electrode with a 90 V potential drop such that upon heating the filament, thermal electrons are produced and accelerated toward the electrode. Some of these electrons pass through the open space of the electrode and impact the C_{60} vapor present in this region, resulting in electron impact ionization of the C_{60}. Primary ions are extracted (16 kV applied to source) and accelerated toward a grounded collimator through a set of electrostatic lenses which focus the beam. The beam is then steered into the Wien filter which allows for the mass selection of C_{60}^+ from the other fragment and contaminant ions in the beam (Wien filter described in more detail below). Verification of the primary ion mass is achieved by pulsing the mass-filtered beam over an aperture and measuring its time of flight. Neutrals are also present in the beam, but are unaffected by steering potentials or Wien filter mass selection. These neutrals must be removed from the beam prior to impact at the target. To this end, an off-center aperture is introduced after the Wien filter, which steers the ion beam enough to pass through, while neutrals remain on a straight-line path and do not pass through the aperture to the target. After passing through the off-center aperture, C_{60}^+ ions are steered toward the target in a manner that the resulting secondary ions are centered in the 8-anode detector (which can be monitored while changing the position of the impacts). The total impact energy of the C_{60}^+ primary ions is 26 keV. Secondary ions are extracted by a 10 kV potential drop to a grounded 90% transmission

grid. Electrons are steered by a weak magnetic field (<100 Gauss) toward an electron detector (start signal for ToF). The secondary ions travel down a 92.9 cm field free flight tube and are detected by an 8-anode detector (stop signal for ToF).

Au Liquid Metal Ion Source Mass Spectrometer

The experimental results described in Chapters III, IV, and V were obtained using the Au Liquid Metal Ion Source (LMIS) Mass Spectrometer. A detailed description of the instrument is available elsewhere[52, 53].

A schematic of the instrument is presented in figure 2-2. Briefly, vacuum in the primary ion leg is maintained at ~$5x10^{-7}$ Torr (idle) or ~$2x10^{-6}$ Torr (LMIS operational) using a 60L/s turbomolecular pump (Pfeiffer Vacuum, Nashua, NH) backed by a 3.8 CFM two-stage rotary vane mechanical pump (Alcatel Vacuum Prod., Hingham, MA). The Au-LMIS consists of a tungsten spring reservoir filled with a Au/Si eutectic (97% Au, 3% Si by mass, Academy Precious Metals, Albuquerque, NM). A 20 mm tungsten needle passes through the center—the needle tip is electrolytically etched to ~90° in order to facilitate the formation of a Taylor cone during primary ion extraction. A full description of LMIS arrangement and production is available in Appendix A. Primary ions are produced by heating the Au/Si eutectic to its melting point (~363°C) and maintaining an extraction potential of 6.9-7.4 kV between the needle tip and extraction electrode (0.5 mm apart). The LMIS emits a wide range of projectiles Au_n^{q+} where $1 \leq n \leq 1000$ and $1 \leq q \leq 10$. Once the source is emitting primary ions, the beam current can be controlled by varying the extraction current control, which adjusts the extraction voltage for a specified current. For reference, typical primary ion beam currents for

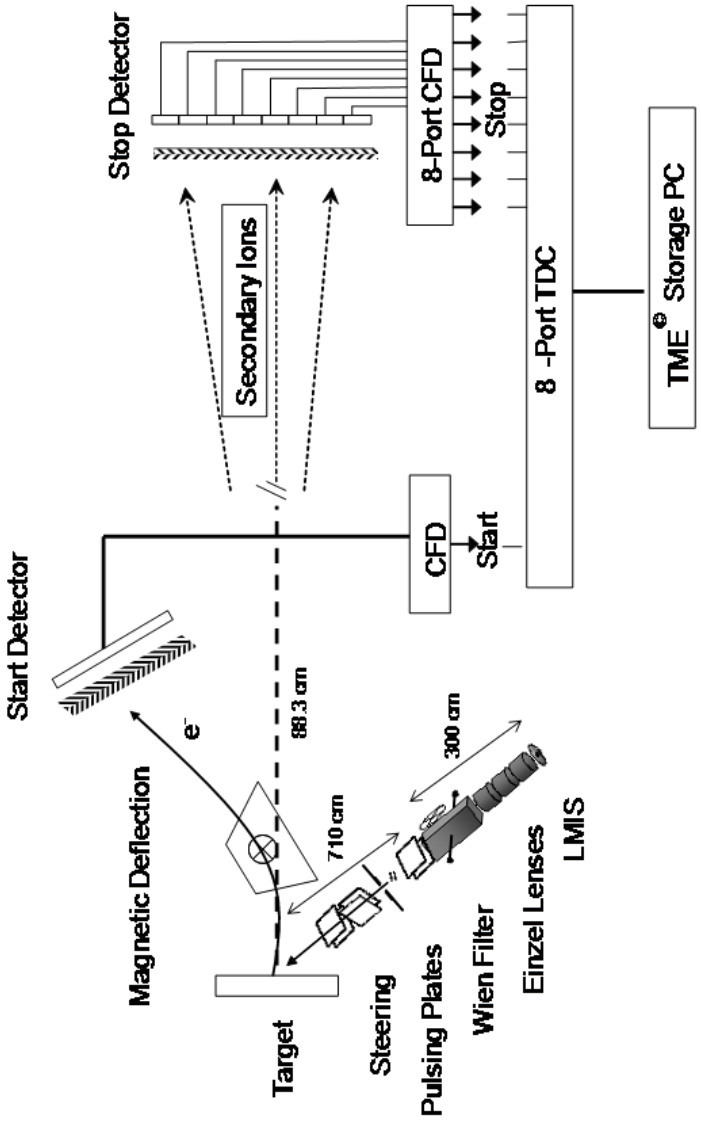

Figure 2-2. Schematic of the Au LIMS mass spectrometer (not drawn to scale).

Au_1^+-Au_5^+ and Au_{400}^{4+} (full beam without pulsing, at 20 μA extraction current) have been measured using a faraday cup at the target and are reported in table 2-1. The Au beam is focused by an einzel lens assembly, where U2 is maintained at ground while U1 and U3 are variable potentials (figure 2-3). The details for the einzel lens potential adjustments for this instrument can be found elsewhere[53].

After focusing, the Au beam enters the Wien filter where the desired primary ion may be mass selected. The Wien filter uses a variable electric field perpendicular to a constant magnetic field (0.3 T). By varying the potentials on the deflection plates, only Au projectiles with a specific velocity (i.e. mass to charge ratio) are allowed to pass through the exit aperture. The velocity of ions passing straight through the filter can be described as follows:

$$v = (10^8 \frac{V_d}{dB}) \qquad \text{Eq. 2-1}$$

where v is the velocity of the ion (cm/sec), V_d is the potential applied to the electric plates (volts), d is the distance between the electric plates (cm), and B is the strength of the magnetic field (Gauss). The relationship between an ion's mass/kinetic energy and the potential on the Wien filter deflection can be obtained (Eq. 2-2) by combining Eq. 2-1 with the relationship between kinetic energy and velocity of ions to give:

$$V_d = K_1 \sqrt{\frac{E_K}{m}} \qquad \text{Eq. 2-2}$$

where V_d is the applied voltage on the deflection plate (volts), K_1 is a constant that incorporates the working conditions of the Wien filter (magnetic field strength and distance between the deflection plates), E_K is the kinetic energy of the ion (eV), and m is

Table 2-1. Currents of Au_n^{q+} beams experimentally measured at the target with a faraday cup. These values are representative of a stable LMIS.

Au_1^+	40
Au_2Si^{2+}	4.2
$AuSi^+$	1.8
Au_3^{2+}	0.6
Au_3Si^{2+}	0.55
Au_2^+	4.1
Au_2Si^+	0.64
Au_3^+	2
Au_3Si^+	0.56
Au_4^+	0.146
Au_5^-	0.2
Au_{400}^{4+}	0.05

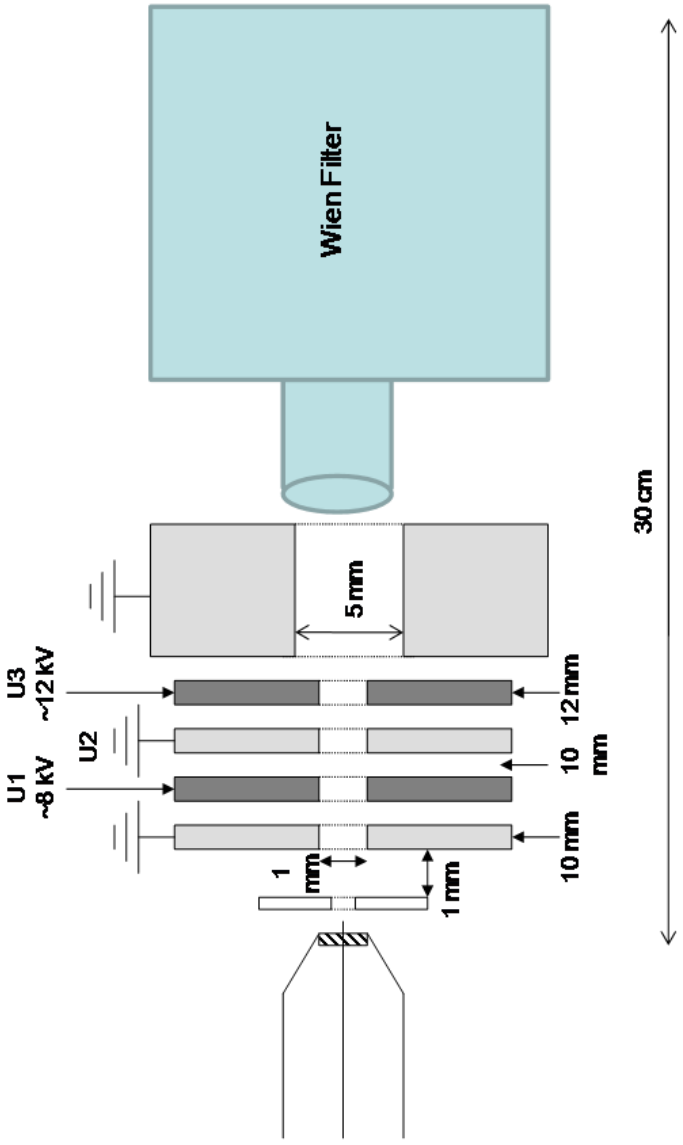

Figure 2-3. Schematic of the LIMS, lens assembly and Wien filter (not drawn to scale).

the mass of the ion (amu)[54]. Individual Au clusters may be selected via the Wien filter for Au_n^{q+} where $1 \leq n \leq 9$. For Au clusters with more than 9 constituents, the Wien filter can only select primary ions with a specific mass to charge ratio. Specifically, in the experiments detailed in chapters IV and V, when referring to the Au_{400}^{4+} projectile, we refer to a projectile that has an average of 400 constituents and 4 positive charges per projectile[26].

After mass filtering, the beam of the selected primary ions is introduced into a high voltage pulsing system. The beam is pulsed for two main reasons. First, this provides a start signal for the primary ion time of flight, which is used to verify the mass to charge of the particles impacting the surface. The primary ion flight distance, i.e. the distance between the aperture and the target, is 50.5 cm. Second, this reduces the beam flux such that particles impact the target surface in the event-by-event bombardment/detection mode (discussed in more detail below). Reduction in the beam current is achieved by pulsing the beam (from -1 kV to +1kV at a repetition rate of 10 kHz, rise time ~25 ns) over a 400 μm exit aperture. In some cases the beam current requires further reduction, which can be achieved by defocusing the beam with einzel lens potentials U1 and U3.

After pulsing, the ions that are allowed to pass through the exit aperture are steered onto the target using horizontal and vertical deflection plates. The goal of steering the primary ion impacts is to center the resulting SI distribution on the 8-anode SI detector. The primary ions are accelerated toward the target in front of the negatively biased target (-9 kV). The electrons that are emitted from the primary ion impact are

deflected with a weak magnetic field (<100 Gauss) to a dual microchannel plate (MCP) assembly (chevron configuration) and detected with a single anode. This electron signal acts as both the stop signal for the primary ion time of flight as well as the start signal for the secondary ion time of flight. Secondary ions produced from the Au-cluster impact are analyzed by their time of flight down the 88.3 cm flight tube and detected by a dual microchannel plate assembly and an 8-anode detector.

Time of Flight Mass Spectrometry

The C_{60} and Au-LMIS mass spectrometers have a similar design in the secondary ion leg. Both instruments isolate the primary ion leg from the secondary ion leg using a gate valve, which is convenient for isolating and protecting the source region during sample introduction or maintenance on the secondary ion leg. The custom-built stainless steel chambers (Kurt J. Lesker, Clairton, PA) are maintained at an ultimate pressure of ~$5x10^{-7}$ Torr by 760 L/s oil diffusion pumps (Edwards Vacuum Products, Tewksbury, MA) backed by 10.6 CFM two-stage rotary vane mechanical pumps (Alcatel Vacuum Prod., Hingham, MA).

The sample holder is a cube composed of either stainless steel or brass. The design specifications for the sample cube can be found in Appendix B. The sample cube is introduced into vacuum via a rotary linear direct motion feedthrough vacuum interlock (MDC Vacuum, Hayward, CA). This feedthrough is attached to a vacuum introduction chamber, separated from the main sample chamber by a gate valve, which can be differentially pumped to ~$1x10^{-2}$ Torr using a 1.2 CFM rotary vane mechanical pump (Welch Vacuum Technology, Niles, IL). When the introduction chamber reaches this

pressure, the gate valve is opened and the sample cube is inserted into the Teflon sample cube holder. The linear feedthrough rod is then removed and the gate valve is closed. The design specifications for the Teflon sample holder are available in Appendix B.

The sample cubes are biased to -9 kV and a grounded 90% transmission grid (Precision E-forming, Cortland, NY) is placed 0.76 cm from the surface of the cube. This forms the extraction region for the SIs and electrons emitted from primary ion impacts. At the end of the flight tube is another 90% transmission grid, which defines the field free region, as well as accounts for the ~80% transmission efficiency for the mass spectrometers described in the following chapters.

Secondary ions are characterized by time of flight, which measures the time required to travel a given distance from their creation to detection. During this path, SIs encounter three distinct regions: an acceleration region, a field free drift region, and a deceleration region. The total flight time for an ion is a summation of the ion's flight time through these three regions (figure 2-4). That is,

$$t_{tot} = t_a + t_{dr} + t_d \qquad \text{Eq. 2-3}$$

where t_{tot} is the ion's total flight time, t_a is the ion's flight time in the acceleration region, t_{dr} is the ion's flight time in the drift region, and t_d is the ion's flight time in the deceleration region.

The flight times for these individual regions can be described as follows:

$$t_a = \sqrt{\frac{2md_a^2}{qV_a}} \qquad \text{Eq. 2-4}$$

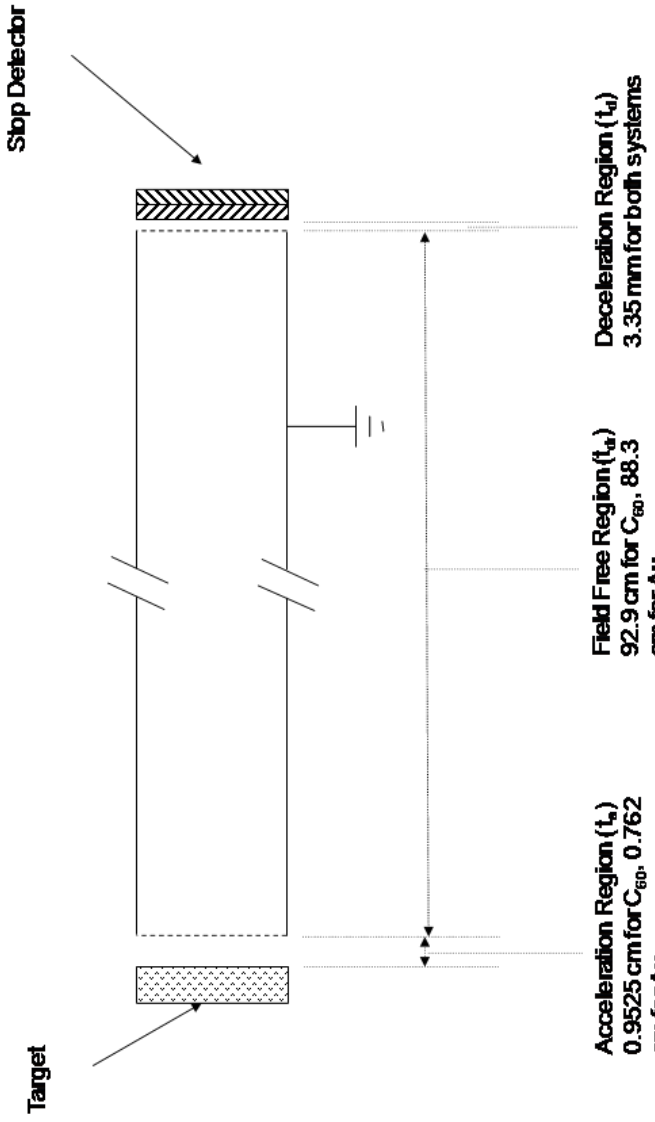

Figure 2-4. Time-of-flight schematic (not drawn to scale).

$$t_{dr} = \sqrt{\frac{md_{dr}^2}{2qV_a}} \qquad \text{Eq. 2-5}$$

$$t_d = \frac{(d_d^2\sqrt{2m})(\sqrt{V_a + V_d} \pm \sqrt{V_a})}{\sqrt{q}\cdot V_d} \qquad \text{Eq. 2-6}$$

Therefore,

$$t_{tot} = \left(\sqrt{\frac{2md_a^2}{qV_a}}\right) + \left(\sqrt{\frac{md_{dr}^2}{2qV_a}}\right) + \left(\frac{(d_d^2\sqrt{2m})(\sqrt{V_a + V_d} \pm \sqrt{V_a})}{\sqrt{q}\cdot V_d}\right) \qquad \text{Eq. 2-7}$$

where m is the mass of the secondary ion, q is the charge state of the secondary ion, V_a and V_d are the high voltage biases applied in the acceleration region and deceleration regions, respectively, d_a, d_{dr}, d_d are the lengths of the acceleration, drift, and deceleration regions, respectively. A full explanation of the derivations for these principles have been discussed elsewhere[1-4,55], but in practice, when the instrument is operational, all values are constant except for mass and charge state of secondary ions. Mass calibration is achieved for experimental results via:

$$m/z = \left(\frac{t_{tot} - C_2}{C_1}\right)^2 \qquad \text{Eq. 2-8}$$

where C_1 is a constant determined by the sample bias and flight length, and C_2 is determined by the speed of the timing electronics[56]. In practice, these constants can be determined by creating a calibration between two ions of known mass-to-charge (e.g. H^- and CH^-). The mass resolution, R, for a mass spectrometer is defined as:

$$R = \frac{m}{\Delta m} = \frac{t}{2\Delta t} \qquad \text{Eq. 2-9}$$

and for the mass spectrometers used in the studies described here, typical mass resolution ranges from ~1500 at m/z 26 (FWHM) to ~500 at m/z 149 (FWHM).

Detectors and Detection Electronics

The signals originating from secondary electrons and secondary ions are amplified by striking microchannel plate (MCP) assemblies. Microchannel plates are generally lead-doped glass electron multiplier microtubes (dynodes) set in parallel arrays. Fused together, they form a thin plate which can be used singly or stacked together. When a particle (ion, electron, neutral) strikes a wall of the microtube, an electron cascade is formed, giving a gain of $\sim 10^3$ across a single MCP. When operational, high voltage is applied across the plates (~1 kV) to facilitate a strong directional path for the electron cascade. In the detector assemblies used in the mass spectrometers here, MCP's are used in Chevron formation[57] giving a total gain of $\sim 10^6$ across the plates. Besides an increase in overall gain, the Chevron formation is also beneficial for decreasing ion feedback.

Microchannel plates used in the mass spectrometers here are non-imaging grade MCPs obtained from Photonics (Pittsfields, MA). Electron detector MCPs are 30mm in diameter (25 mm active area), whereas secondary ion detector MCPs are 50 mm in diameter (active area of 40mm). The detection efficiency for secondary ions is dependent on the velocity, i.e. for ions with the same kinetic energy, lower mass (higher velocity) SIs will have greater detection efficiency than SIs with higher mass (lower velocity). This detection efficiency has been estimated at 50-85% for electrons and 60-85% for secondary ions[57].

The electron cascade that results from a particle impact on the MCP assembly is collected at the exit of the MCP using a copper anode. In the case of the electron detector, a single copper plate is used as a "single anode" collector. In the case of the secondary ion detector, a "multi-anode" detector is used. The multi-anode detector consists of an 8-segment collector made from a copper plated circuit board and is discussed in detail elsewhere[52]. A schematic of the MCP assembly in Chevron configuration with the two types of detectors is shown in figure 2-5. Multi-anode detectors are used in the case of the SI detector due to the efficiency of the projectiles used in our experiments to impact analyte surfaces. As discussed in the previous chapter, large and massive clusters produce multiple ion emission from single impacts. As such, the capability to monitor multiple secondary ions with the same m/z is advantageous. Signals obtained from the electron cascade on the anode are monitored via the "pulse counting" regime. A proportionally larger amplitude pulse is observed whenever ions with the same time of flight strike the detector at same time. In this regime, however, only one ion is registered by the counting electronics. By dividing the anode into 8 separate and independent anodes, up to 8 ions with the same flight time can strike the detector and be registered, given that each ion strike its own anode. For this reason, it is important to center secondary ion emission on the SI detector to increase the detection capability. A full diagram of the 8-anode detector, including detailed dimension information, is available in Appendix B.

Under the current design of the SI detector, the active area is ~93% of the total surface area. Given the detection efficiency for the MCPs (~50%), and the transmission

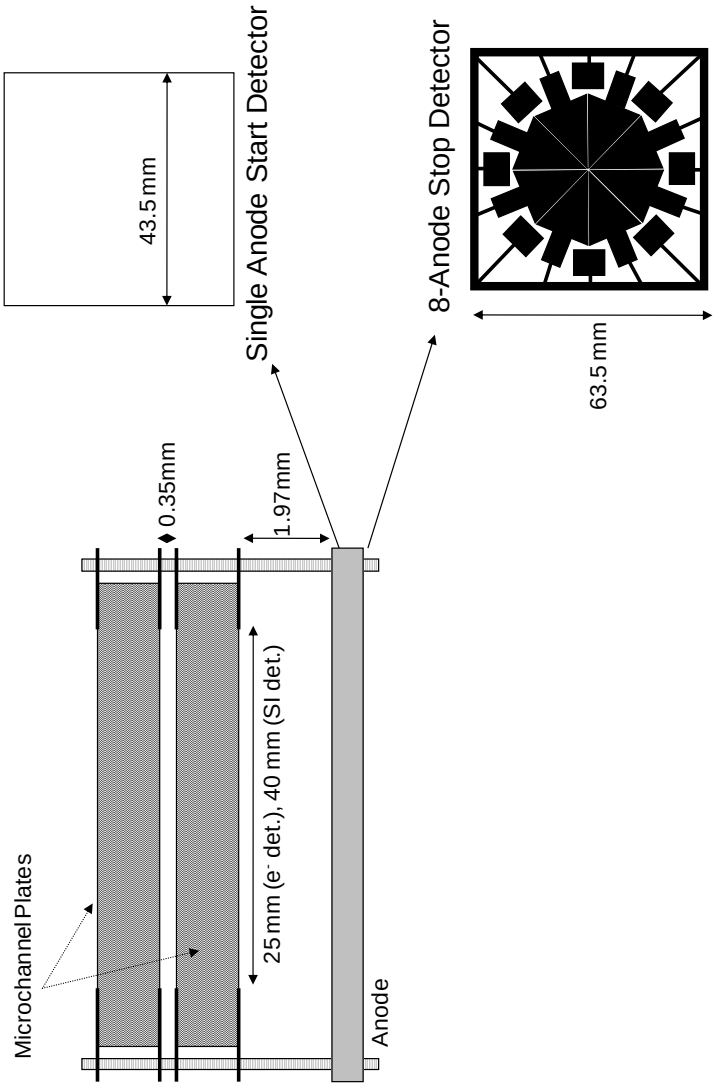

Figure 2-5. Schematic of micro-channel (Chevron formation) plate detector assembly for start and stop detectors (not drawn to scale). A detailed schematic for the 8-anode detector is presented in Appendix B.

efficiency of the ToF mass spectrometer with grids (~81%), the final detection efficiency for SIs in the mass spectrometers used here is ~38%.

The electron flux output by the MCPs is registered by the anode as a voltage spike which is then passed on to a constant fraction discriminator (CFD). The output signal from the electron detector is passed to a quad-port CFD (Canberra (Tennelec), Meriden, CT). The output signal from the SI detector is passed to an octo-port CFD (Ortec, Oak Ridge, TN). The CFD transforms the negative voltage pulse from the anode into a NIM (square wave) pulse which proceeds to the time to digital converter (TDC). The CFD allows to block signals below a specified threshold from passing to the TDC (Institut de Physique Nucleaire, Orsay, France) for processing. The TDC has a single port for the input of a "start" signal and an octo-port for the input of 8 "stop" signals. Upon receiving a start signal, the TDC opens a data acquisition window (the duration of which can be set by the user) during which it will collect stop signals. The TDC converts the NIM pulse to a digital signal which is recorded by personal computer. The digital output is processed within the "Total Matrix of Events" (TME) software, described elsewhere[53], allowing for the acquisition of a mass spectrum as well as the ability to calculate SI yields and other relationships from individual impact/emission events.

Event-by-Event Bombardment/Detection Mode

One of the key features of the mass spectrometric methodology presented in this research is the use of the event-by-event bombardment/detection mode. In this regime, single projectile ions impact the surface and the resulting secondary electrons and ions

are stored as singular impact "events." These events are resolved in time and space such that during stochastic sampling over the field of view, projectiles are statistically unlikely to sample the same regions. Since the ejecta from each impact are stored and recorded independently of one another, relationships between the secondary ions from single impacts can be examined. One relationship that will be discussed in later chapters is the secondary ion yield (Y_{SI}) which is the number of secondary ions of a particular m/z emitted per projectile impact. This relationship is experimentally defined as:

$$Y_{SI} = \frac{(I_{SI} - I_B)}{N_T} \qquad \text{Eq. 2-10}$$

where I_{SI} is the experimental relative intensity of a SI, I_B is the experimental relative intensity of the background, and N_T is the total number of primary ion impacts (as determined by secondary electron emission). The background subtraction is performed in order to reduce the influence of metastable decay as well as random noise in the peak area.

Another relationship that can be monitored with the event-by-event bombardment/detection mode is the coincidental emission of secondary ions. Coincidental emission implies that ions were co-emitted from a single impact, and therefore, originated from the same desorption volume. This is the basis for the investigation of nano-materials since the sampling volume from single impacts, for example with Au_{400}^{4+} is ~10^3 nm^3. Coincidental yields can be experimentally determined for two ions, A and B, given:

$$Y_{A,B} = \frac{I_{A,B}}{N_T} \qquad \text{Eq. 2-11}$$

where $Y_{A,B}$ is the coincidental yield for ion A when it is co-emitted with ion B, $I_{A,B}$ is the experimental relative intensity for ion A in coincidence with ion B, and N_T is the total number of primary ion impacts. These concepts will be described in more detail in the next chapters.

Development of the Methodology for Positive Mode

One limitation of the instrumental design of the event-by-event mass spectrometers described here is the necessity for electron emission to signal the arrival of a primary ion onto the target. This requirement prohibits the ability to monitor positively charged secondary ions. Many SIMS investigations, especially analysis of biological samples, require access to both the negative and positive secondary ion signals emitted from the impact. Indeed, the electron capture or ionization probability is highly correlated to the type of molecules investigated. While the analysis of negative SIs is straightforward in our instrument, due to the strong electron emission, operation in the positive mode is more complex. A start signal for the time of flight analysis is required to be able to perform ToF-SIMS in positive mode. Two methods have been developed to bridge the gap in positive ion mode operation.

The first method involves obtaining a start signal from the pulse generator of the primary ion beam. It should be noted, however, that the pulsing plates are located ~50.5 cm before the target, which means that the start is registered before the projectile strikes the target. As such, the signal is delayed by a gate delay generator (Ortec, Oak Ridge, TN) in order to match the start of the acquisition window with the calculated time of the arrival of the projectile onto the sample. In practice, the primary projectile is tuned in

the negative mode using the standard procedure at -9 kV target voltage. The output from the delay gate generator is input into the start port of the CFD, and the electron detector voltage and electromagnet are turned off. A test of this method was performed in negative mode. Figure 2-6 shows the mass spectra obtained for Glycine under Au_5^+ bombardment when started from electrons and from the pulse generator. It can be seen that the secondary ion mass spectrum obtained using the pulse generator is similar to that resulting from the start with electron. However a zoom on the area corresponding to the CN^- secondary ion clearly shows a decrease in the mass resolution (from ~560 to ~120, at m/z 26, FWHM). The mass resolution decreases further in mass spectra obtained with Au_9^+ impacts, as shown in Figure 2-7, where unit resolution is lost. The decreases in the mass resolution are directly related to the primary ion energy distribution as well as the time jitter resulting from an ion's location in the pulse. For Au_5^+, for instance, the primary ion ToF peak width is ~200 ns, while for Au_9^+ it is ~500 ns. The mass resolution decreases further with Au_{400}^{4+}, as it has a primary ion peak width of ~3 μs. Though the mass resolution is reduced for ions starting from the pulser, as opposed to electron signals, the resolution is still sufficient to identify peaks separated by one mass unit when using projectiles of size $1< n < 5$. Theoretically, shortening the distance between the pulsing region and the target should minimize peak broadening for larger projectiles, but this would require reorganization of the existing instrument.

The goal of the second method developed was to maintain the advantages of utilizing massive projectiles for bombardment. This method uses the secondary ion detector as a start signal for the acquisition. As previously described, large and massive

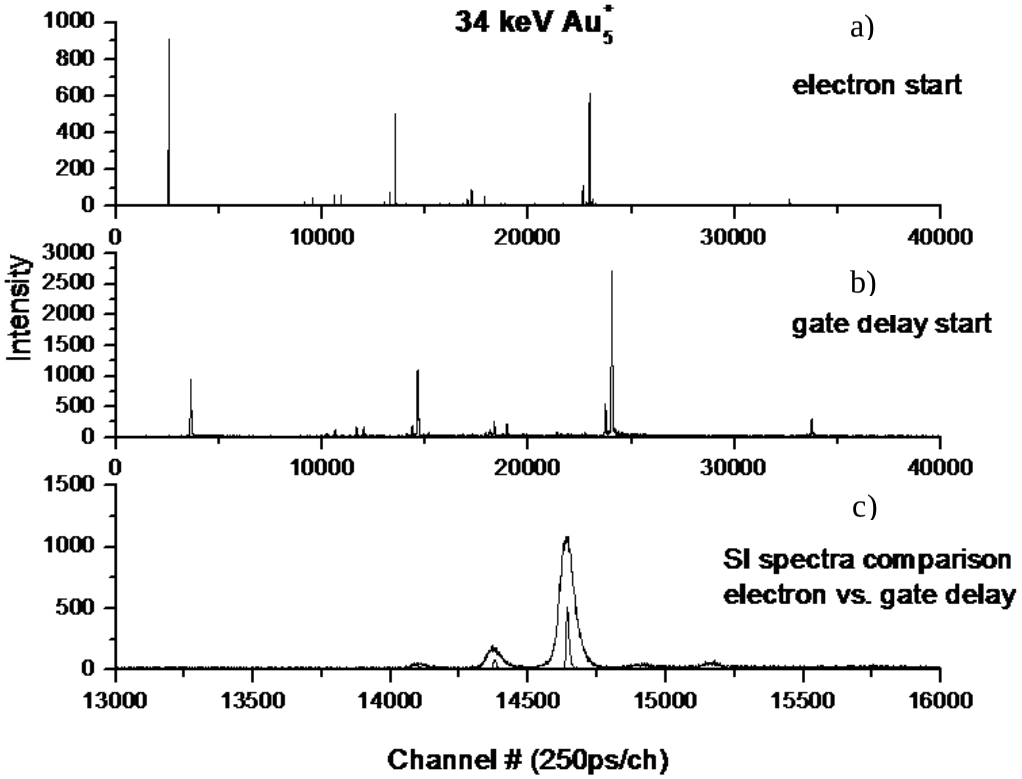

Figure 2-6. Negative secondary ion mass spectra obtained from **a)** electron start signal **b)** gate delayed pulsed start using 34 keV Au_5^+ primary ions and **c)** an overlay of part a and b for comparison.

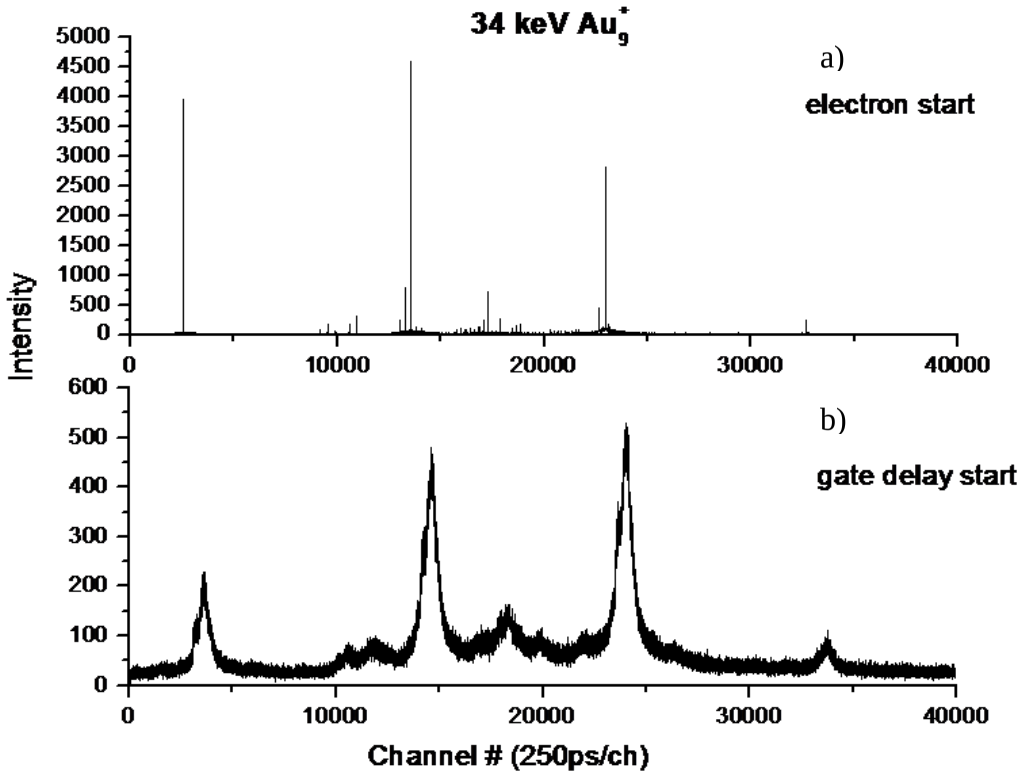

Figure 2-7. Negative secondary ion mass spectra obtained from **a)** electron start signal **b)** gate delayed pulsed start using Au_9^+ primary ions.

cluster impacts generate abundant multiple ion emission. In this method, the detection of the lightest secondary ion produced from the impact is used as a start signal for the remaining secondary ions co-emitted with it. In practice, signal outputs from the octo-port "stop" CFD are split between the octo-port TDC and a Linear Fan-In/Fan-Out Module (LeCroy Corp., Chestnut Ridge, NY) which converts the signal from the 8-anodes into an OR-circuit. It sets the condition that if any of the 8-anodes registers a SI impact, it supplies an output signal which is fed into the "start signal" of the stop TDC. Figure 2-8 shows a positive ion mass spectrum of Glycine bombarded with Au_{400}^{4+} projectiles using this second method. The mass resolution is comparable to that obtained in negative mode. Analysis of this mass spectrum however is not straightforward, since the start signal for each projectile impact originates from ions with different molecular weights. This point is illustrated in the figure 2-8, where the overall mass spectrum is an overlap of spectra obtained from various "start signal" ions (m/z 28, 30, 32, etc.).

In the interest of obtaining a singular start signal from the SI start approach, sample targets can be spiked with a low mass ion with high ionization efficiency (such as Li, Na, or K). A low mass ion is preferable because information about ions of lower mass (thus, shorter flight time) will be lost in analysis. The goal, also, is to have a concentration of this light ion such that at least one Li, Na, or K is emitted under each impact (i.e. 100% yield). In such a case, all ToF acquisition windows will be started from the same ion. NaCl was chosen over Li, due to the abundant presence of Na in biological samples, implying it may be less disruptive to a biological system. Moreover, Li and K have isotopic distributions (two isotopes for Li and three for K), whereas Na is

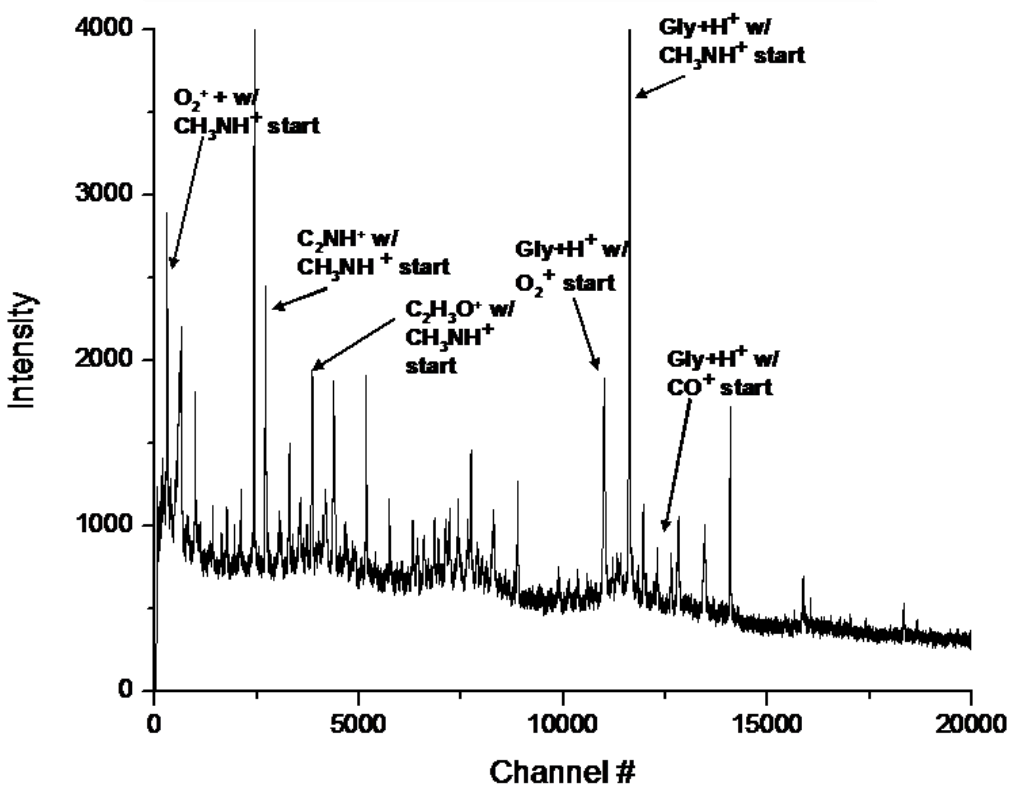

Figure 2-8. Positive secondary ion mass spectrum of Glycine bombarded with 80keV Au_{400}^{4+} with start signal from secondary ion detector.

monoisotopic. This further simplifies the possible starts resulting from Na. To test this method, a solution of Gly and NaCl was created with a concentration of 10 mg NaCl/mL (concentration optimized for maximum $[Gly-H]^-$ yield). Figure 2-9 shows the mass spectrum resulting from Glycine spiked with NaCl in the positive mode using 80 keV Au_{400}^{4+}. Here, most start signals originate from Na^+, as spectral overlap is lessened, with a few exceptions in the low mass region. This technique for obtaining a positive ion mass spectrum may not be feasible for all sample types, especially samples that cannot be prepared in solution or those that require chemical co-localization.

Another signal that may be utilized for time of flight analysis is photon emission after projectile impact. Photon emission resulting from atomic and small cluster impacts on CsI and NH_4Cl films in the event-by-event bombardment/detection mode has been previously observed[58, 59]. Recently, we have also observed photon emission from large cluster projectile bombardment (Au_{100n}^{4+}, $1 \leq n \leq 4$) on CsI and organic dye targets. The photomultiplier tube used to detect photon emission has a maximum quantum efficiency of 22% at 410 nm, with a solid angle of 7.5×10^{-3}sr (fractional area ~6×10^{-4} mm^2). The total detection efficiency, which is a factor of the fractional area and the quantum efficiency, using this design is ~1×10^{-4}. Based on this detection capability, our data suggest that there is ~1 photon emitted per electron detected from a CsI target. The detectable yield of the photon signal is too low to be practically utilized as a start signal. Higher impact energies would be needed for ToF-MS with photon starts to be practical.

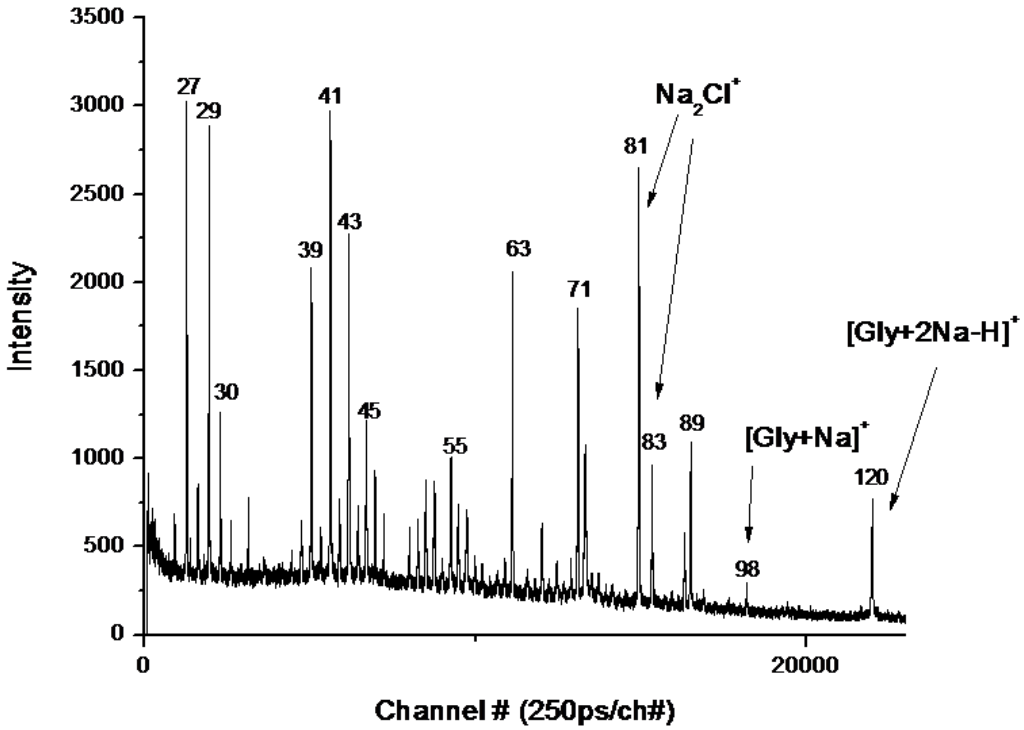

Figure 2-9. Positive secondary ion mass spectrum of Glycine/NaCl solution bombarded with 80keV Au_{400}^{4+} with start from secondary ion detector.

Sample Preparation

The sample preparation procedures used to fabricate the lipid bilayer and nano-object samples used in the studies presented here are described in detail in the next chapters.

CHAPTER III

ANALYSIS OF SOLID-SUPPORTED LIPID BILAYER ORGANIZATION AND NANO-DOMAIN FORMATION

Introduction

The cell membrane is a vital component of the biological cell, acting as a semi-permeable barrier between the cell and the environment. This structure is a bilayer which has a complex chemical make-up, consisting of proteins, cholesterol, and phospholipids. Many analytical techniques have been utilized to provide information regarding the nature of the lipid bilayer environment. Fluorescence techniques, which have been widely applied to lipid studies, have excellent detection sensitivity and localization capabilities. However, these techniques only provide information for tagged species. Furthermore, it is difficult to predict how these fluorophores may perturb the delicate and already complex lipid system[60]. Atomic force microscopy is also commonly used for lipid investigations to provide structural information. This technique, however, does not provide chemical identification of species[61-65]. Recently, studies of lipid membranes have utilized mass spectrometric techniques due to their ability to provide molecular information without the need to tag molecules for specificity. Imaging mass spectrometry (IMS), in particular, can provide both spatial and molecular information from lipid membranes[60, 64, 66, 67]. Matrix-assisted laser desorption ionization (MALDI) experiments mainly focus on imaging the distribution of lipid components in tissue samples. Research efforts by Woods, Caprioli and Sweedler

focus on the investigations of lipid distributions in tissue samples from rat brain[68-73] and rat embryos[74]. While MALDI offers the ability to ionize large intact molecules (>3000 Da), the need to apply a chemical matrix complicates investigations. Further, the area probed by a laser shot is generally dictated by the diffraction limit (micron scale). It should be noted that much work has been done to improve this resolution by laser focusing[75], desorbed ion focusing[76], and sample preparation[77]. Secondary ion mass spectrometry, while unable to ionize large molecules (>3000 Da) with high efficiency, offers improved spatial resolution. Nano-SIMS instruments have achieved the most focused beam of incident particles (~33nm with Cs^+ beam), however the focused beam causes extensive fragmentation in the interrogation region, which requires species to be isotopically labeled in order to attain chemical specificity. Kraft and Boxer modified lipids with ^{13}C and ^{15}N to study phase separation in the bilayer[64, 78]. Lechene and co-workers monitor multiple isotopes in mass spectrometry (termed MIMS[79, 80]) incorporated into biological membranes and other sub-cellular components. In order to obtain intact molecular species, larger primary projectiles, such as Bi_3^+ and C_{60}^+ are utilized[60, 81-84]. Cluster primary ion beams, however cannot be focused to the spot sizes attained with atomic projectile beams. One technique that provides molecular information from species located within an area of about 10 nm of one another is event-by-event SIMS. The use of event-by-event mass spectrometry allows for a mass spectrum to be obtained from a single impact, and as a result, correlations can be made between co-emitted secondary ions from individual desorption volumes.

The investigations into native biological membranes are complex due to the abundance and diversity of chemical species incorporated in the bilayer. One tool that researchers use to isolate specific chemical interactions between molecules in the lipid membrane for study is the solid-supported lipid bilayer[85]. Solid-supported lipid bilayers (SLBs) consist of a single bilayer structure held to a hydrophilic solid support structure by Van der Waals forces. SLBs have been shown to be two-dimensionally fluid, as is the case with cells[86]. They are also used due to the ease of adding other molecules such as membrane-bound proteins, or cholesterol and sphingomyelin to induce the formation of lipid rafts. Many mass spectrometry groups use these models for IMS standards as well as for fundamental investigations into cellular functioning and signaling[64, 78, 87-90].

When investigating SLBs, it is important that their structural integrity be maintained during sample preparation for vacuum environment, since SIMS is a vacuum technique. A serious challenge with the use of SLBs in SIMS is the fact that they are stable only in aqueous environments. Upon dehydration, the bilayer structure may reorganize/delaminate into a random configuration[91]. This is not the preferred orientation for analysis, since it is not the orientation of biological cell membranes. This sample preparation issue is handled by flash freezing in liquid ethane or propane to quickly preserve lateral organization. A concern, however, is that melting and refreezing is difficult to control, so sample damage can occur.

In order to study these effects, a sample preparation technique, developed by Albertorio and co-workers was employed whereby lipids functionalized with poly(ethylene glycol) were added to vesicles before fusion to the hydrophilic substrate

(see fig. 3-1)[92]. The thickness of the PEG layer depends on the degree of polymerization, and is estimated to be ~3 nm for PEG550 and ~12 nm PEG5000[92]. This method has been shown to protect bilayer structure at the air-water interface, while not interfering with two-dimensional mobility of the lipids in the bilayer. In order to be a viable sample preparation for SIMS analysis, the PEG must not interfere with SI emission from the underlying bilayer. The use of PEG-protection also allowed for SIMS analysis of bilayer organization in order to determine if orientation-related differences in secondary ion emission could be observed via mass spectrometry.

Experimental Section

a. Preparation of PEG-Bilayers

1-Palmitoyl-2-Oleoyl-sn-Glycero-3-Phophocholine (POCP), *1*,2-dioleoyl-*sn*-glycero-3-phosphoethanolamine-*N*-[methoxy(poly(ethylene glycol)] (PEG-DOPE) were purchased from Avanti Polar Lipids (Alabaster, AL) with PEG molecular weights of 550 and 5000. *N*-(Texas Red sulfonyl)-1,2-dihexadecanoyl-*sn*-glycero-3-phosphoethanolamine (Texas Red DHPE) was obtained from Molecular Probes (Eugene, OR). Saline solutions were prepared using 150 mM NaCl (Sigma-Aldrich). Poly(dimethylsiloxane) (PDMS) was used to fabricate wells and microfluidic devices.

Glass microscope slides were purchased from VWR International and were cleaned and annealed according to established procedures[93]. Briefly, borosilicate glass slides were boiled in 1/10 v/v diluted 7X detergent solution in purified water. Slides were then washed with purified water profusely. The cleaned slides were dried and annealed in an oven at 500°C for 5 hours. Silicon oxide wafers were purchased from

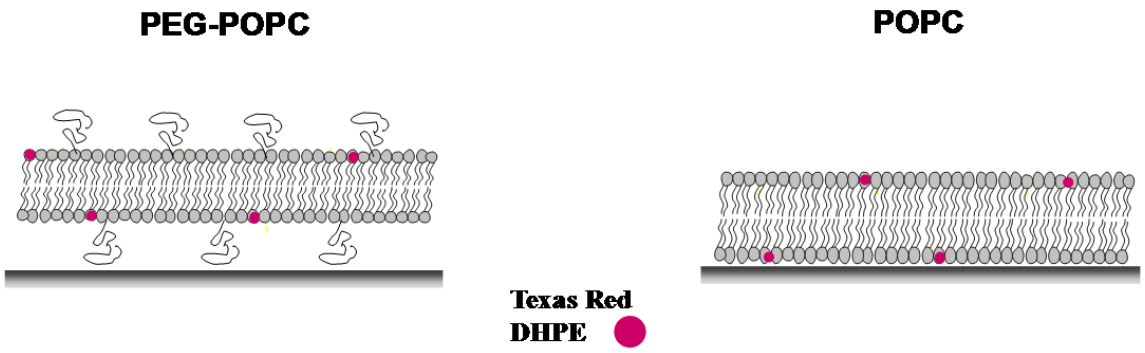

Figure 3-1. Schematics of PEG-protected and unprotected POPC bilayers .

Montco Silicon Technologies, Inc. (Spring City, PA) and were washed by the same method. Wafers were annealed at ~800°C for 5 hours.

Small unilamellar vesicles were prepared from lipopolymers, dye, and/or cholesterol using the desired mole fraction in chloroform. Solvents were evaporated under a stream of dry nitrogen followed by desiccation under vacuum overnight[94]. Vesicles were rehydrated in saline solution at pH 7.4. After 10 freeze−thaw cycles the large vesicles were extruded through a polycarbonate filter, which had an average pore size of 50 nm. Small unilamellar vesicles were 70 ± 10 nm in diameter as determined by dynamic light scattering using a 90Plus particle size analyzer from Brookhaven Instruments Corp.

Vesicles were deposited onto the surface of the glass slides or silicon oxide wafers, confined by a PDMS well. Vesicles spontaneously adsorb, rupture, fuse and organize into a bilayer in aquous solutions on hydrophilic substrates[95]. After a 5 min incubation period, the wells were thoroughly rinsed with purified water in order to remove any unfused vesicles. PEG-protected bilayers were dried at room temperature in a vacuum dessicator overnight. Bilayer quality was monitored via fluorescence microscopy while hydrated, after freeze-drying and after exposure to high vacuum. For SIMS analysis, bilayers were prepared on silicon oxide wafers which were taped directly to the sample cube with no other preparation. Samples were then introduced into the mass spectrometer.

Three supported lipid bilayer samples were prepared for SIMS analysis: one unprotected and therefore disorganized, and two protected by PEG and therefore

organized bilayer samples. Unprotected lipid samples were composed of 99.9 mol% 1-Palmitoyl-2-Oleoyl-sn-Glycero-3-Phosphocholine (POPC) and 0.1 mol% Texas-Red 1,2-dihexadecanoyl-sn-glycero-3-phosphoethanolamine (TR-DHPE). The smaller polymer chain samples were composed of 10 mol% 1,2-Dioleoyl-sn-Glycero-3-Phosphoethanolamine-N-[Methoxy(Polyethylene glycol)-550] (PEG550-PE), 0.2 mol% TR-DHPE, and 89.8 mol% POPC. The longer polymer chain used for protection of the bilayer was prepared from 0.5 mol% 1,2-Dioleoyl-sn-Glycero-3-Phosphoethanolamine-N-[Methoxy(Polyethylene glycol)-5000] (PEG5000-PE), 0.2 mol% TR-DHPE, 99.3 mol% POPC.

b. Preparation of Lipid Raft Bilayers

A lipid raft model was prepared using a mixed lipid system with cholesterol. Bilayers were composed of 24.9 mol% 1-Palmitoyl-2-Oleoyl-sn-Glycero-3-Phophocholine (POCP), 24.9 mol% 1,2-Dipalmitoyl-*sn*-Glycero-3-Phosphocholine (DPPC), 49.9 mol% 25, 26, 26, 26, 27, 27, 27-heptafluorocholesterol, and 0.3 mol% *N*-(Texas Red sulfonyl)-1,2-dihexadecanoyl-*sn*-glycero-3-phosphoethanolamine (Texas Red DHPE). POPC, DPPC, and heptafluorocholesterol were purchased from Avanti Polar Lipids (Alabaster, AL), Texas Red DHPE was purchased from Molecular Probes (Eugene, OR). Fluorinated cholesterol was selected for SIMS analysis for its specificity in the negative ion mode. The formation of lipid rafts is highly sensitive to substrate roughness and charge. As such, domains did not form on silicon oxide wafers. The substrate used in this study was borosilicate glass. Vesicles containing these four components were prepared according to the procedure described above and deposited

onto cleaned and annealed borosilicate microscope slides. Lipid solutions and glass/PDMS substrate were heated to ~70°C before deposition (above the liquid-gel transition temperature) and allowed to come to room temperature before rinsing with purified water. Samples were freeze dried in order to preserve the lateral organization of the chemical species as well as prepare a dry sample for mass spectrometry under vacuum environment. Samples were frozen under -80°C (~3 hours), then stored in a -20°C vacuum dessicator (~10^{-3} Torr) until the water ice was completely sublimated (~3 hours). For SIMS analysis, glass substrates were affixed to stainless steel sample cube with double-sided conductive carbon tape. Edges of the slide were coated with silver paint to help mediate charging effects of the glass.

c. Instrumental

Bilayer organization was monitored in the positive and negative ion modes using the LMIS instrument described in chapter II. In the negative ion mode, 136 keV Au_{400}^{4+} was utilized in the event-by-event bombardment/detection mode. In the positive ion mode, 20 keV Au_5^+ was used to bombard bilayers, where ToF cycles were triggered by the delayed pulser signal as described in chapter II. Lipid rafts were analyzed in the negative ion mode using C_{60}^+ in the event-by-event bombardment/detection mode.

Bilayer quality was monitored with fluorescence microscopy. Samples were observed on an inverted Hg arc lamp epifluorescence Nikon Eclipse TE2000-U microscope with a 10× objective. The fluorophore, Texas Red-DHPE, absorbs 560 nm light and emits 630 nm light. As such, series 31004 Texas Red/Cy3.5 filter sets were utilized (Chroma Technology Corps.). Images were obtained using a MicroMax 1024b

CCD camera (Princeton Instruments) and processed using MetaMorph software (Universal Imaging).

Results and Discussion

a. Lipid Bilayer Organization

The structural integrity of the lipid bilayers was monitored via fluorescence microscopy. Figure 3-2 presents the fluorescence microscopy images of the distribution of the Texas Red tag in a bilayer with and without PEG protection. The PEG image is obtained for a PEG550 bilayer. In both of the hydrated samples, a uniform fluorescence is observed across the surface, which is indicative of the two-dimensionally fluid bilayer. The black lines are scratches which were intentionally administered after vesicle fusion in order to provide a reference for orientation under the microscope. Upon dehydration of the bilayer samples, it is apparent that the PEG-protected bilayer maintains the uniform fluorescence as well as the reference lines, while the unprotected sample delaminates and rearranges. Damage is observed in the fluorescence image where light regions show fluorescent probe accumulation and dark regions show areas of diminished probe concentration. After introduction into a high vacuum environment (~10^{-6} Torr), the PEG-protected bilayer still maintains the even fluorescence and reference lines, implying that no significant damage is created as a result of sample preparation. The unprotected sample maintains the areas of light and dark regions where tags have accumulated, though damaged after initial dehydration, introduction into the vacuum caused no apparent shift in the damage regions.

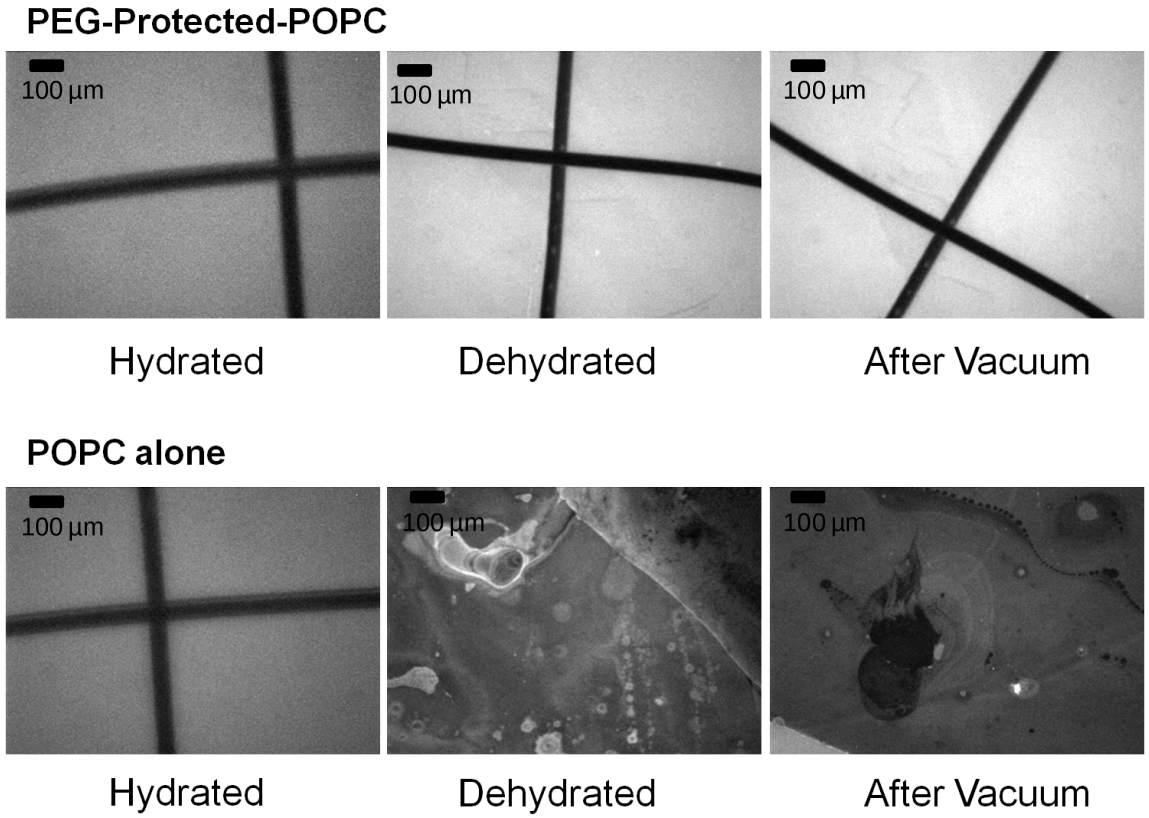

Figure 3-2. Fluorescence microscopy images of PEG-protected and unprotected POPC bilayers when hydrated, dehydrated, and exposed to high vacuum environment (~10^{-6} Torr).

The negative secondary ion mass spectra resulting from impacts of 136 keV Au_{400}^{4+} are presented in figure 3-3 for a) the unprotected lipid layer, b) the bilayer protected by PEG550 and c) PEG5000. Characteristic peaks in the low mass region (<100 Da) are evident for both the lipid as well as from the underlying substrate. C_2H^-, $C3^-$, C_4H^-, etc. emission is likely due to fragmentation of the lipid's hydrocarbon tail, whereas PO_2^- and PO_3^- originates from the phosphocholine head group. SI emission is also observed from the underlying substrate (SiO_2^-, SiO_3H^-, etc.). Recalling the depth of emission for secondary ions, the presence of secondary ion emission from the underlying substrate validates the thickness of the bilayer as < 10 nm.

Interestingly, the addition of PEG to the surface of the bilayer did not significantly alter the hydrocarbon signal compared to POPC alone. The relative abundances of carbon containing peaks remained approximately the same from POPC, PEG550 and PEG5000 samples. Indeed, it is difficult to differentiate between protected and unprotected samples in the negative ion mode. Furthermore, the thickness of the PEG layer has been approximated to be ~12 nm for PEG5000, which is larger than the reported SI depth of emission for Au projectiles, yet SI emission from the underlying bilayer appears to be unaffected by this coverage. PEG-modified bilayers have been shown to allow the binding and incorporation of very large biomolecular species into the bilayer[91, 96]. This is thought to occur due to the nature of the PEG molecules on the surface—they exist as a mesh network, which retain a thin layer of hydration to help protect bilayer organization. The observation of lipid-specific SI emission from the PEG

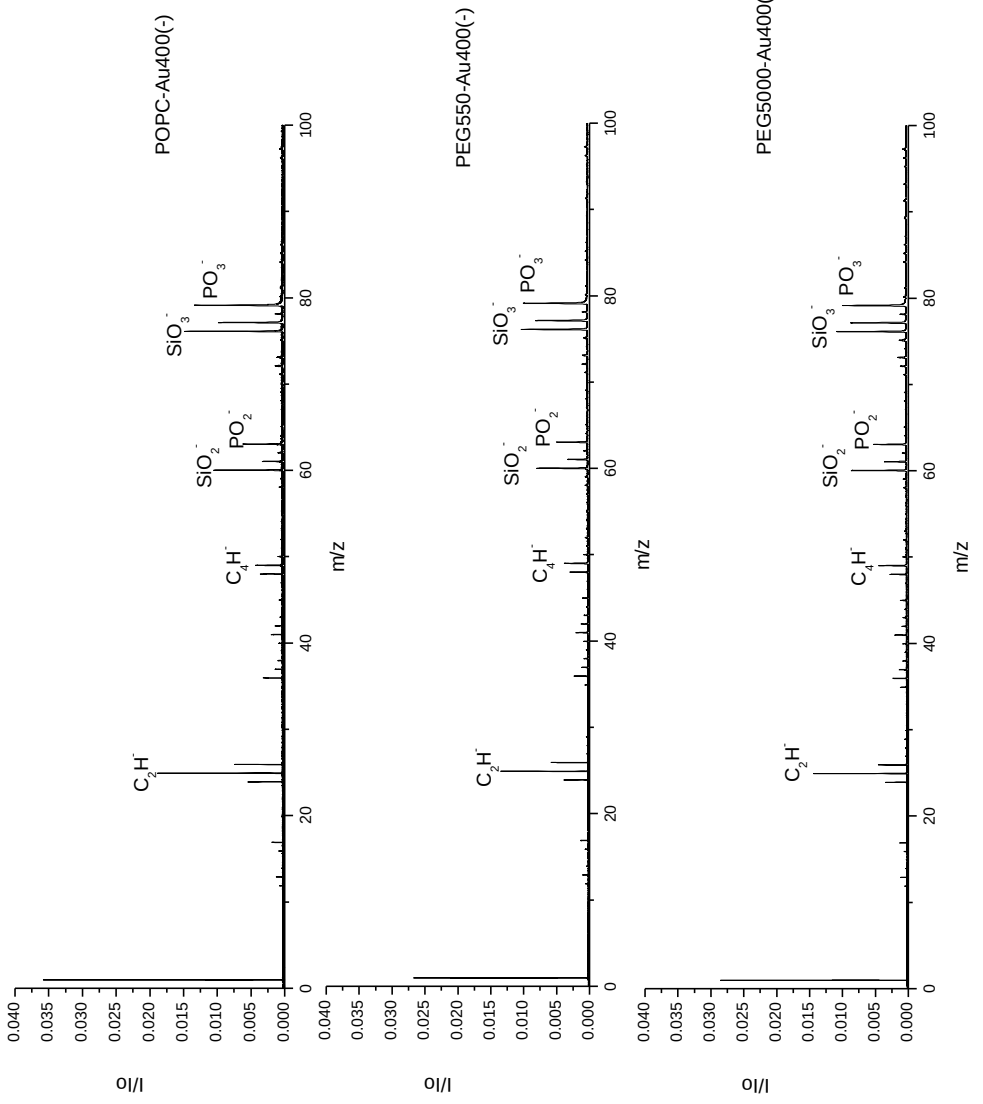

Figure 3-3. Negative secondary ion mass spectra of POPC, PEG550, and PEG5000 bilayers obtained from ~1x10^6 impacts with 136 keV Au_{400}^{4+} .

bilayers implies that the density of the polymer is low in comparison to the field of view of a primary ion impact (~10 nm in diameter).

A majority of the literature regarding mass spectrometry of lipid bilayers focuses on the positive ion mode, due to the specificity of the chemical signal obtained from lipid headgroup fragments. Positive ion mass spectra resulting from 20 keV Au_5^+ are presented in figure 3-4 for the PEG5000-protected and unprotected POPC bilayers. Peak broadening is observed in the positive ion spectra using the delayed pulser "start" methodology. The decrease in the mass resolution is related to the primary ion position and energy distribution, as described in chapter II. In the POPC bilayer alone (fig. 3-4A), fragments of the phosphocholine headgroup correspond to m/z 86 $[C_5H_{12}N]^+$, 104 $[C_5H_{13}NO]^+$, 184 $[C_5H_{15}NPO_4]^+$, and 224 $[C_8H_{19}NPO_4]^+$. Also present in the mass spectrum is contribution from the underlying silicon substrate at m/z 73 $[(CH_3)_3Si]^+$ and 147 $[(CH_3)_5SiO_2]^+$. Upon investigation of the PEG-protected bilayer spectrum (fig. 3-4B), again lipid-specific signals can be observed through the PEG protection. Qualitatively, the first observation of bilayer protection and organization can be observed by inspection of the peak areas from lipids and from the silicon oxide substrate. Indeed, substrate peaks at m/z 73 and 147 are present in the PEG-protected bilayer spectrum, but are in lower abundance compared to the disorganized sample. For a quantitative comparison of the two samples, organized versus disorganized, ratios of substrate and lipid peaks are calculated (see figure 3-5). Significant changes in the peak areas ratios are not observed for lipid peaks (e.g. m/z 86, 166, 184), but ratios between

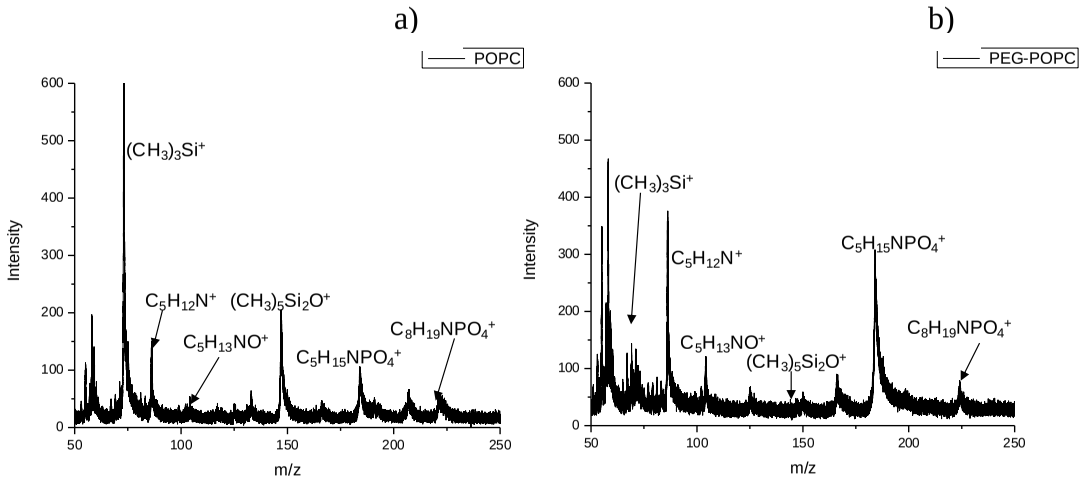

Figure 3-4. Positive secondary ion mass spectra of **a)** POPC and **b)** PEG5000 bilayers obtained from ~1x10^6 impacts with 20 keV Au_5^+.

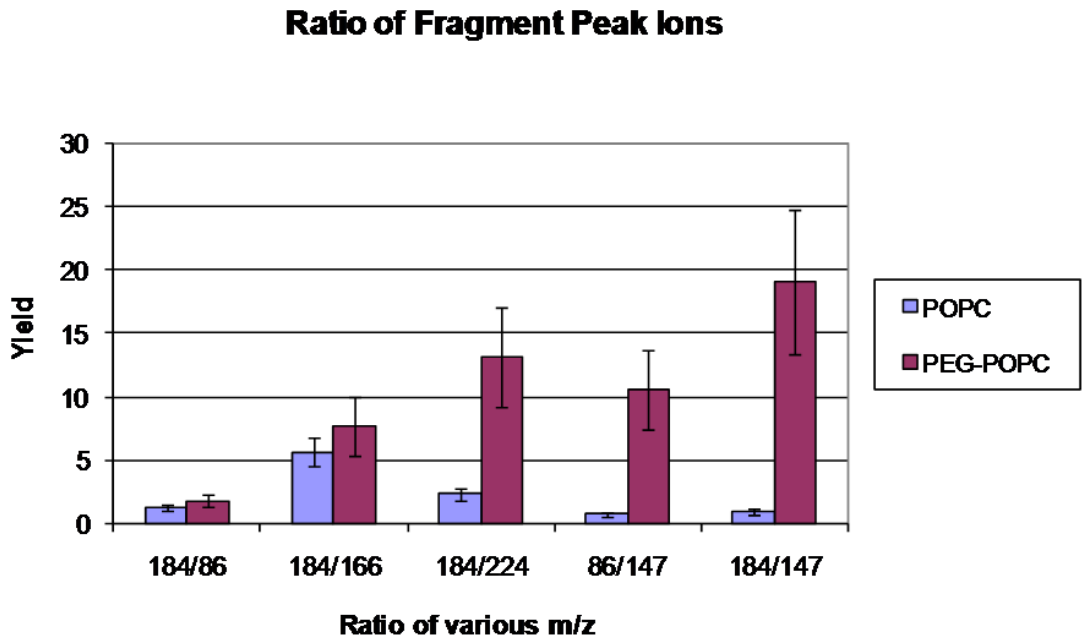

Figure 3-5. Ratio of phosphocholine fragment peaks and silicon substrate peaks for POPC and PEG5000 bilayers (obtained from mass spectra in fig. 3-4).

lipid and substrate peaks reveal a 6-19 fold increase in the ratios for the PEG-protected sample.

Another interesting feature differentiates PEG-protected, organized bilayers from unprotected, disorganized bilayers. In the high mass region (>500 Da), evidence of the protonated molecule for POPC is visible at m/z 760 (fig. 3-6B), though the relative abundance is low. The low intensity can be attributed to two factors: the low resolution (i.e. peak broadening) of the positive mode, and the efficiency of Au_5^+ to produce quasi-molecular ions. The average yield for the molecular ion peak (0.0035) is above the critical limit for the decision limit (0.002, as defined by Currie[97]). The key, however, is the fact that this signal is not observed in the unprotected bilayer (fig. 3-6A). The organizational dependence of bilayer secondary ion emission has been observed previously[89, 98]. Authors attribute the observation of the molecular ion in organized layers to the destabilization of the bilayer after several projectile impacts. This disruption may decrease the surface interactions, allowing for increased sputtering probability. Since the molecular ion is only observed in organized bilayers, this signal may be used as an indicator of membrane structure without the addition of fluorophores.

b. Lipid Raft Characterization

The supported lipid bilayer platform can be expanded to model more complex molecular interactions. One topic of interest for molecular biologists is the appearance of clusters of ordered and tightly packed lipids in lipid membranes. These clusters, termed lipid rafts, are thought to have a significant role in physiological functioning, including signaling specific protein or drug molecule binding. Models of lipid raft

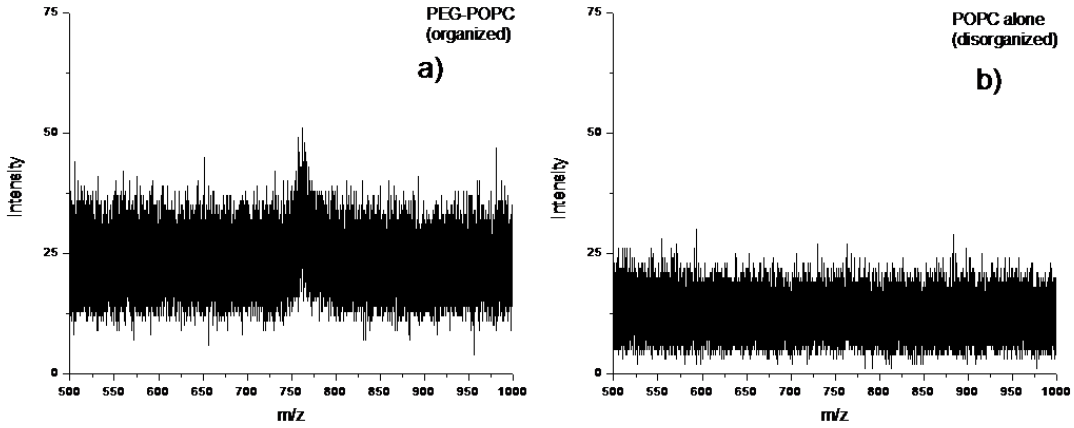

Figure 3-6. High mass region of the positive secondary ion mass spectra of **a)** POPC and **b)** PEG5000 bilayers obtained from ~1x10^{6} impacts with 20 keV Au_5^+.

systems predict enrichment in the raft of particular components such as cholesterol and sphingolipid[99]. Many mass spectrometry studies have found similar results[64, 78, 81, 83, 84]. Still, there are many unresolved questions regarding the chemical make-up of lipid rafts. Though imaging mass spectrometry has been utilized in the past to identify location-specific molecular signals in order to describe surface organization, the technique is still limited by the spatial resolution of the probe. The event-by-event bombardment/detection mode of operation is particularly suited for co-localization analysis of chemical species within ~10 nm of one another. As previously noted, by monitoring coincidental emission, it is possible to determine relationships between chemical species located within the emission volume.

Figure 3-7A shows the initial deposition of the bilayer, still in the hydrated state. A fluorescence microscopy image of a POPC bilayer (protected with PEG5000) without cholesterol is presented in fig 3-7B for comparison of the homogeneous signal from the fluorescent tag. As can be seen in part a) light and dark regions show areas of differing fluorophore concentrations. The domains have an average diameter of ~1 μm. Again, scratch marks were applied to the glass slide, and these lines are maintained even though lipids are 2-dimensionally mobile. Observation of the same sample after dehydration (fig 3-8B) and after introduction into high vacuum environment (fig 3-8C) show the preservation of the domains and reference lines, implying the sample preparation procedure does not cause significant damage.

Lipid domain samples were analyzed by C_{60}^{+} secondary ion mass spectrometry run in the event-by-event bombardment detection mode. Negative ions were identified

a)

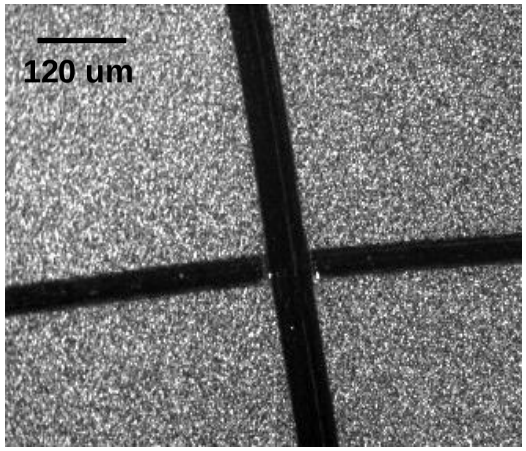

POPC/DPPC/cholesterol/TR

b)

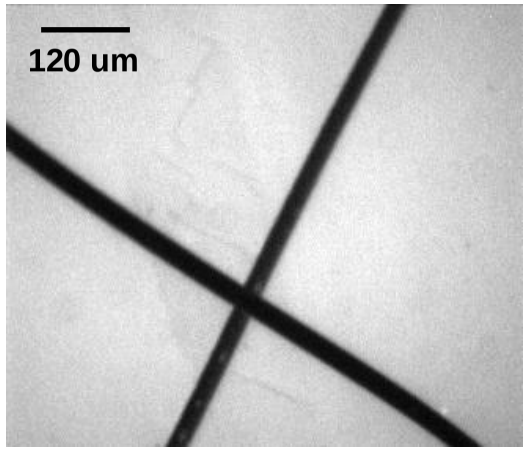

POPC/PEG-PE/TR

Figure 3-7. Fluorescence microscopy images of **a)** cholesterol induced lipid rafts and **b)** PEG5000 bilayers.

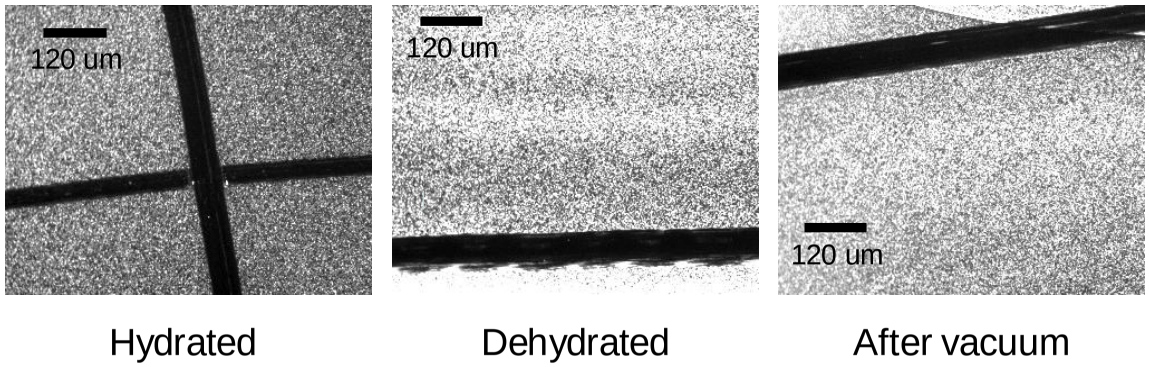

Figure 3-8. Fluorescence microscopy images of 2:1:1 F7-cholesterol: POPC: DPPC bilayers when hydrated, dehydrated, and exposed to high vacuum environment (~10^{-6} Torr).

by time-of-flight and were recorded for each 26 keV C_{60}^{+} impact. The total negative secondary ion mass spectrum is shown in figure 3-9. Secondary ion emission is observed from the lipids (hydrocarbon, cyanide, and phosphate ions) as well as from the underlying glass substrate (silicon oxide ions). Cholesterol was identified via the F^{-} peak at m/z 19. In comparing the yields of the lipid raft bilayer to those of the PEG-protected bilayer, raft samples exhibited an observable decrease in relative abundances of lipid peaks compared to substrate peaks. This difference (~6-8 times decrease in SiO_3H^{-} / PO_3^{-} ratio) can be attributed to the difference in packing order and density due to the liquid-gel transition. Further, ~50% of the lipid composition has been substituted by cholesterol.

One benefit of using the event-by-event bombardment/detection mode is the ability to obtain more insight into specific impact/emission events. In order to obtain a representative mass spectrum for a given component of the system, the co-emission from that component may be displayed in a coincidence mass spectrum. For example, in order to obtain a representative mass spectrum from the cholesterol domain, all ions co-emitted with F^{-} are monitored (fig 3-10). Projectile impacts resulting in fluoride emission also showed emission from hydrocarbon peaks and silicon oxide peaks. The most intense peak in the coincidence spectrum is m/z 77 SiO_3H^{-} (coincidence yield = $3.5x10^{-5}$), which implies that fluorine-rich areas of the bilayer are less than 10 nm in thickness. The presence of hydrocarbon peaks are not specific to lipid side chains, since impacts with C_{60}^{+} cause some re-emission of carbon from the projectile as hydrogen adducts. For a more chemically specific signal for the lipids, phosphates originating

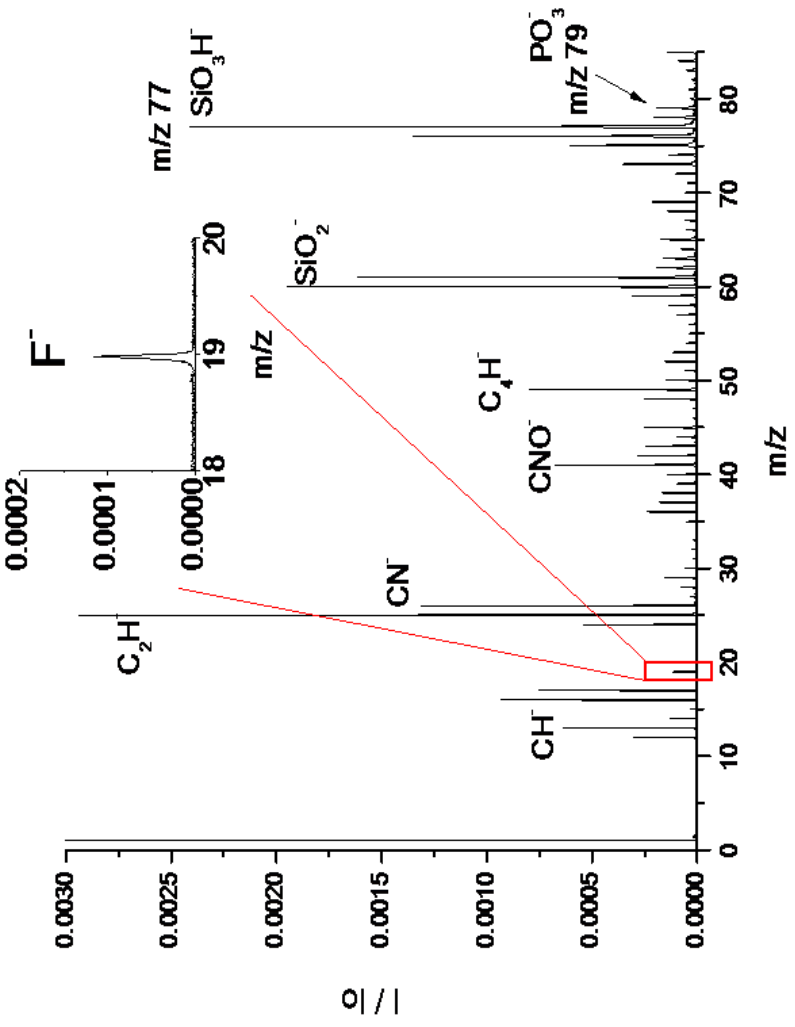

Figure 3-9. Negative secondary ion mass spectra of 2:1:1 F7-cholesterol: POPC: DPPC bilayers obtained from ~$2x10^6$ impacts with 26 keV C_{60}^+.

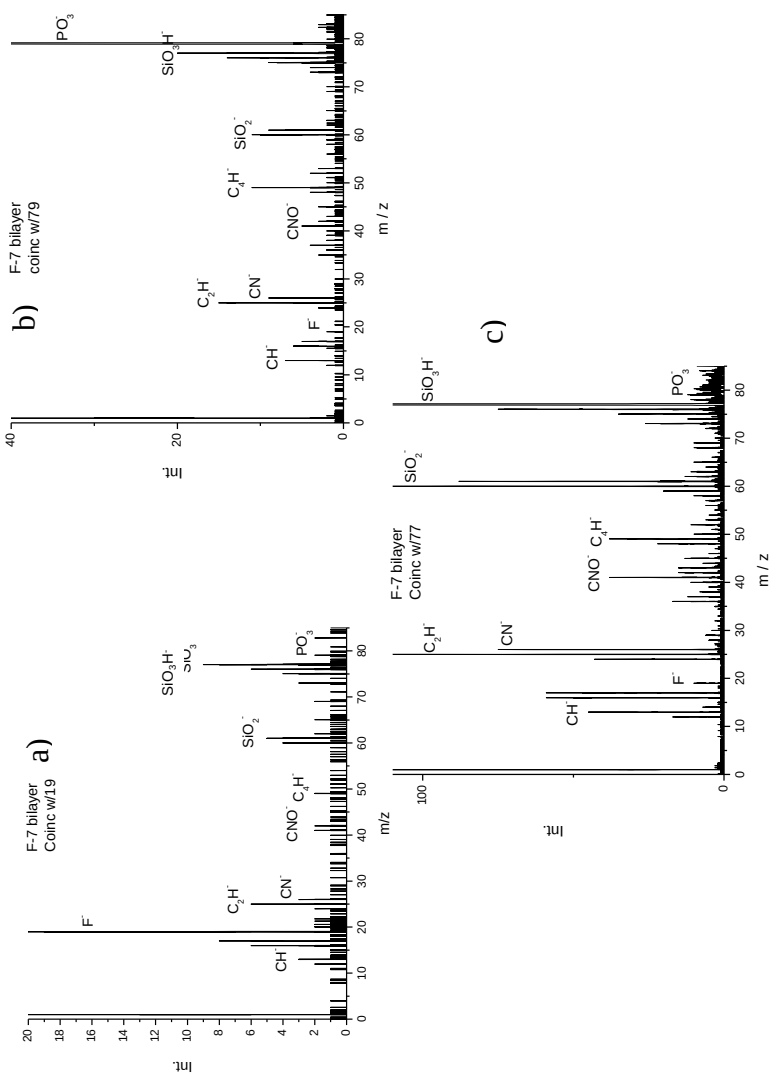

Figure 3-10. Coincidence ion mass spectra of 2:1:1 F7-cholesterol: POPC: DPPC bilayers obtained from co-emission with **a)** m/z 19 F^-, **b)** m/z 79 PO_3^-, **c)** 77 SiO_3H^-.

from the phosphocholine headgroup are monitored (m/z 63 PO_2^-, m/z 79 PO_3^-). The coincidence mass spectrum in fig 3-10A shows the absence of m/z 63 and small contribution from m/z 79 (coincidence yield = 1.8×10^{-6}). This implies that, at the level of single impacts (~10 nm in diameter), cholesterol segregates into domains. Further evidence of this phenomenon is provided by the coincidence ion mass spectrum of all ions co-emitted with PO_3^- (fig. 3-10B). Here, contribution from fluoride is approximately the same as observed in the fluoride coincidence spectrum (coincidental yield = 2.0×10^{-6}). Emission from the underlying glass substrate again predominates in SiO_2^- and SiO_3H^- emission. This spectrum also shows emission from non-specific hydrocarbon peaks. For reference, a coincidence mass spectrum for ions co-emitted with m/z 77 SiO_3H^- is presented in fig 3-10C. Here, contribution of both lipid-specific and cholesterol-specific peaks is visible.

Beyond the coincidence mass spectrum, more quantitative information may be derived from monitoring co-emission in the event-by-event bombardment/detection mode. Information about the planar surface homogeneity can be obtained using a concept called the correlation coefficient[33, 41, 100], Q, which is defined by:

$$Q_{A,B} = \frac{\sum_{x_A}\sum_{x_B} x_A x_B P(x_A x_B)}{\sum_{x_A} x_A P(x_A) \sum_{x_B} x_B P(x_B)} \cong \frac{Y_{AB}}{Y_A Y_B} \qquad \text{Eq. 3-1}$$

where $Q_{A,B}$ is the correlation coefficient between two ions A and B, x_A, x_B are the number of SIs of type A and B respectively detected simultaneously per single impact/emission event (x_A and x_B range from 0 to 8 in the experiments performed here due to the use of an 8-anode SI detector), $P\ x_A$ and $P\ x_B$ are the probability distributions

for the number of ions of A and B detected per impact/emission event, respectively. Px_Ax_B is the probability distribution for ions A and B co-emitted per single projectile impact. If the emission of ions A and B is uncorrelated, i.e., A and B are emitted independently within the single impact/emission event, then the distribution $P(x_Ax_B)$ is equal to $P(x_A)P(x_B)$, which results in $Q_{AB} = 1$. When the emission of ions A and B is correlated, implying that emission events that are favorable for the emission of ion A are also favorable for ion B, then $Q_{AB} > 1$. If the emission of ion A and B are anti-correlated, implying that events favorable for the emission of ion A are not favorable for B, then the value of the correlation coefficient, $Q_{AB} < 1$. In practice, probability distributions are approximated as the experimentally detected secondary ion yields, Y_A, Y_B, and $Y_{A,B}$, respectively.

The correlation coefficients for the cholesterol-induced lipid domain bilayer are presented in table 3-1. Representative peaks were selected for cholesterol (m/z 19 F^-), lipid (m/z 79 PO_3^-), and glass substrate (m/z 77 SiO_3H^-) for calculation of the correlation coefficients. The correlation coefficient for emission of fluoride in coincidence with silicon oxide is 1.5 implying that the emissions are correlated. This correlation provides further evidence that cholesterol rich domain regions exist as thin films with thicknesses <10 nm, which allows for the enhancement in the co-emission of both F^- and SiO_3H^- from beneath the cholesterol layer from each C_{60}^+ impact. The correlation coefficient between the silicon substrate and the lipid in the bilayer is 1.1. This value implies that the co-emission is uncorrelated, i.e. random emission. This lack of correlation likely originates from the variable thickness of the lipid bilayer depending on the packing order

Table 3-1. Correlation coefficients from lipid raft bilayers.

Co-emitted Ions	Q
F^- and SiO_3H^-	1.5
F^- and PO_3^-	0.8
PO_3^- and SiO_3H^-	1.1

and density of lipids in the liquid ordered and liquid disordered states. A variable thickness of mixed lipid phase systems has been observed in atomic force microscopy studies[64]. Of particular interest in this study is the relationship between cholesterol and lipid organization. The correlation coefficient between F^- and PO_3^- suggests that the emission of these two ions is anti-correlated (Q = 0.8). Anti-correlation implies that the emission of F^- from the cholesterol inhibits the emission of PO_3^- from the lipids. This anti-correlation can be explained in the planar inhomogeneity of the bilayer. If cholesterol segregates from lipids and forms domains larger than 10 nm, then impacts from C_{60}^+ either contact a region rich in cholesterol or lipid, but not both. The observation of F^- in the PO_3^- spectrum, and vice versa, is then likely due to the boundary where both are physically co-located.

Conclusion

Secondary ion mass spectrometry is well-suited to provide molecular information for biological systems such as the supported lipid bilayer model. The ability to monitor the structural integrity of the bilayer based on secondary ion information alone (without the use of fluorescent probes) allows the supported lipid bilayer model to more closely represent the chemical nature of the biological membrane. A caveat, however, is that biological samples must be stable in the dehydrated state, and must be introduced into a vacuum environment, which arguably decreases the value of the model system.

The use of the event-by-event bombardment detection mode provides information on individual nano-domains since each projectile samples an area ~10 nm in diameter. To validate the lipid raft study presented here, AFM information can be

utilized to monitor raft thickness. Future SIMS studies should focus on preparing lipid raft environments with different classes of lipids (i.e. different head-groups) to allow for the differentiation of lipid components. This information should provide a further indication of the degree of separation of each lipid component from the cholesterol-rich areas.

CHAPTER IV

CHARACTERIZATION OF INDIVIDUAL NANO-OBJECTS BY SECONDARY ION MASS SPECTROMETRY*

Introduction

Secondary ion mass spectrometry (SIMS) is a method of choice for the characterization of nanometric size features in solids by virtue of its detection sensitivity and spatial resolution[3, 79, 101-105]. The characterization of nano-domains embedded in or supported on solids is well documented[105-108]. We examine here a case which has received scant attention, the application of SIMS for the analysis of individual free-standing nano-objects. Prior to addressing this topic, it is useful to briefly recall some performance features of the microprobe and microscope techniques which employ beams of atomic to massive projectiles (e.g. Cs^+, C_{60}^+) at keV impact energies[64, 79, 109]. Isotopic signals may be detected from sample volumes as small as a few tens of nm^3, i.e. volumes containing a few thousand atoms[79]. When molecular information is sought, the volumetric limit scales with the size of the chemical species. For low mass analytes (molecular weights of a few hundred Da), a minimum size of $\sim 10^3$ nm^3 appears necessary to obtain detectable emission of fragment and molecular ions[110, 111]. The dimensions noted account for the depth of secondary ion (SI) emission (5-10 nm) [3], further they assume full energy deposition of the bombarding projectile in the solid.

---

*Parts of this chapter are reprinted with permission from *Analytical Chemistry*, Volume 80, Veronica T. Pinnick, Sidhartharaja Rajagopalachary, Stanislav V. Verkhoturov, Leonid Kaledin, and Emile A. Schweikert, Characterization of Individual Nano-Objects by Secondary Ion Mass Spectrometry, pages 9052-9057, 2008.

The present study is concerned with SIMS applied on free-standing nano-objects with a dimension smaller than the depth of SI emission and, *a fortiori*, smaller than the range of the bombarding primary projectiles (where the term "range" refers to the depth of projectile penetration in bulk solids). One can consider these objects to be of "sub-critical assay dimensions." The specimens examined here are individual boehmite nanowhiskers of ~2 nm diameter and ~200 nm length. The fibers are grafted in random orientation on silicon oxide rods. Examination by transmission electron microscopy shows the nanowhiskers in the stand-up position in a brush-like arrangement (figure 4-1). In our experiments, individual whiskers were bombarded with a suite of projectiles (Au^+, Au_3^+, Au_9^+, Au_{400}^{4+}) with keV energies. The impacts could occur at any position along a 200 nm length at varying angles. The parameter of interest for SI emission is the object's diameter ($\leq$ 2 nm) versus the depth of SI emission ($\leq$10 nm) and the projectile range (from ~36 nm with Au_1^+ to $\geq$10 nm with Au_{400}^{4+})[112, 113]. The latter represents a case of impact physics described as a collision of finite-size objects. The topic has been studied experimentally and theoretically with keV projectiles only at the extreme level of cluster-cluster and atom-cluster interactions[114-116]. Those studies typically involved the C_{60} molecule as a gas phase target and concluded that such collision regimes lead to extensive fragmentation[114]. The question then arises: can the SI signal from individual

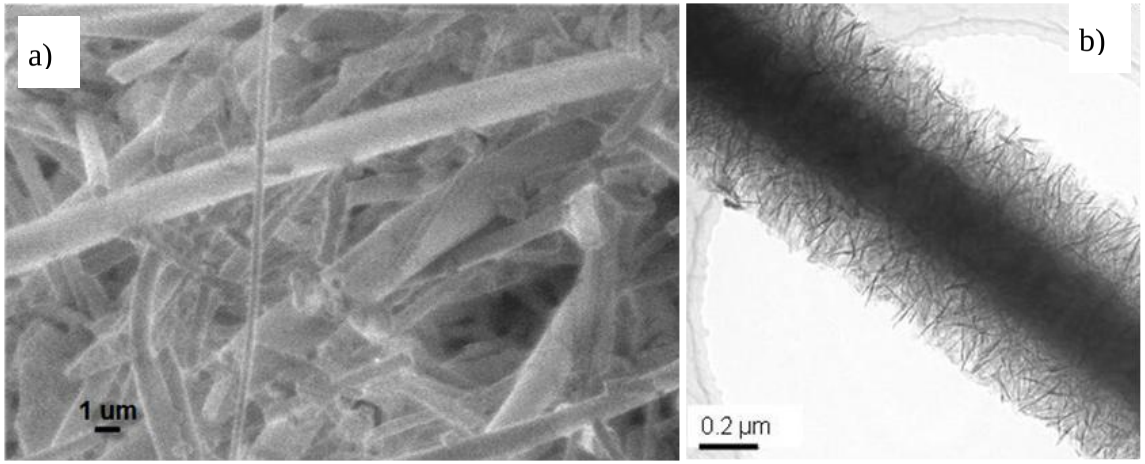

Figure 4-1. a.) SEM image of silicon oxide rods, which act as the supports for the nanowhiskers, in random orientations (Image acquired by Tom Stephens, MIC, Texas A&M). **b.)** TEM image of boehmite alumina nanowhiskers in the "stand up" position along a silicon oxide rod (TEM image provided by L. Kaledin, Argonide Corp).

nano-objects be compared for chemical analysis with those from an "infinite" size reference material?

The experiments were carried out as a sequence of single projectile impacts with individual collection of the corresponding SI emissions. Thus, in the shot-by-shot mode, objects of "sub-critical assay dimensions" are examined one-by-one. We present below observations from the boehmite nanowhiskers and compare them for validation and for an estimate of sample-size effects with data from "bulk" samples of varying sizes, and that replicate similar chemical compositions.

Experimental Section

a. Materials. The nanowhiskers (Argonide Corporation[117], Sanford, FL) consist of boehmite (AlOOH) fibers (~2 nm diameter, 200 nm length). The nano-alumina is bonded to a microglass fiber (Lauscha B06 glass with average diameter ~0.6 μm and with composition of 58% SiO_2, 12% Na_2O, 10% B_2O_3,) that serves as a scaffold. In order to compare the results of impacts on confined nano-volumes to impacts on much larger objects, aluminum-based "bulk" samples of varying physical structure were also examined: spherical aluminum nanoparticles with an average diameter of 50 nm (Argonide Corporation), boehmite powder (μm mesh size) (Wako Pure Chemical Co., Richmond, VA), and wafer samples prepared by sputter coating aluminum onto silicon wafers (~200 nm Al layer).

Whisker samples were obtained as thick disks, which were affixed to stainless steel supports using carbon tape. Nanoparticles were prepared for SIMS using a procedure described elsewhere[105], where samples were prepared and stored in argon

atmosphere and 25 μL of a 25 mg/mL solution was deposited on a stainless steel substrate. The thickness of the nanoparticle layer is estimated to be on the order of a few microns. The nanoparticles were briefly exposed to air (~10 min) during deposition on the substrate and insertion into the mass spectrometer. Boehmite powder was pressed onto double-sided carbon tape which was affixed to a stainless steel support. Each target was examined in our experiment with the suite of projectiles, i.e. data were obtained under the same experimental conditions for ready comparison.

b. Electron Microscopy Measurements. SEM images were obtained by Tom Stephens at the microscopy and imaging center (MIC) at Texas A&M University using an FEI Quanta 600 FE-SEM. Images are secondary electron images obtained at working distance 3 mm and accelerating voltages 0.5 kV. Samples to be analyzed were halved, one half for SEM analysis, one half for SIMS analysis. Whisker samples were sputter-coated (Cressington 208HR) with ~2nm of Pt/Pd for increased conductivity for SEM analysis only. The TEM image shown in figure 4-1b was provided by the whisker manufacturer (Dr. Leonid Kaledin, Argonide Corporation).

Results and Discussion

a. Mass Spectra. The mass distributions of the negative SIs from Au_{400}^{4+} impacts on the nanowhiskers and bulk samples are shown in figure 4-2A and 4-2B, respectively. The secondary ion spectrum from the nanowhiskers (figure 4-2A) differs quantitatively and qualitatively from that presented in figure 4-2B, which is representative of the bulk samples examined, including targets as small as 50 nm nanoparticles. The sum of the yields of all Al-containing SIs collected from the whisker

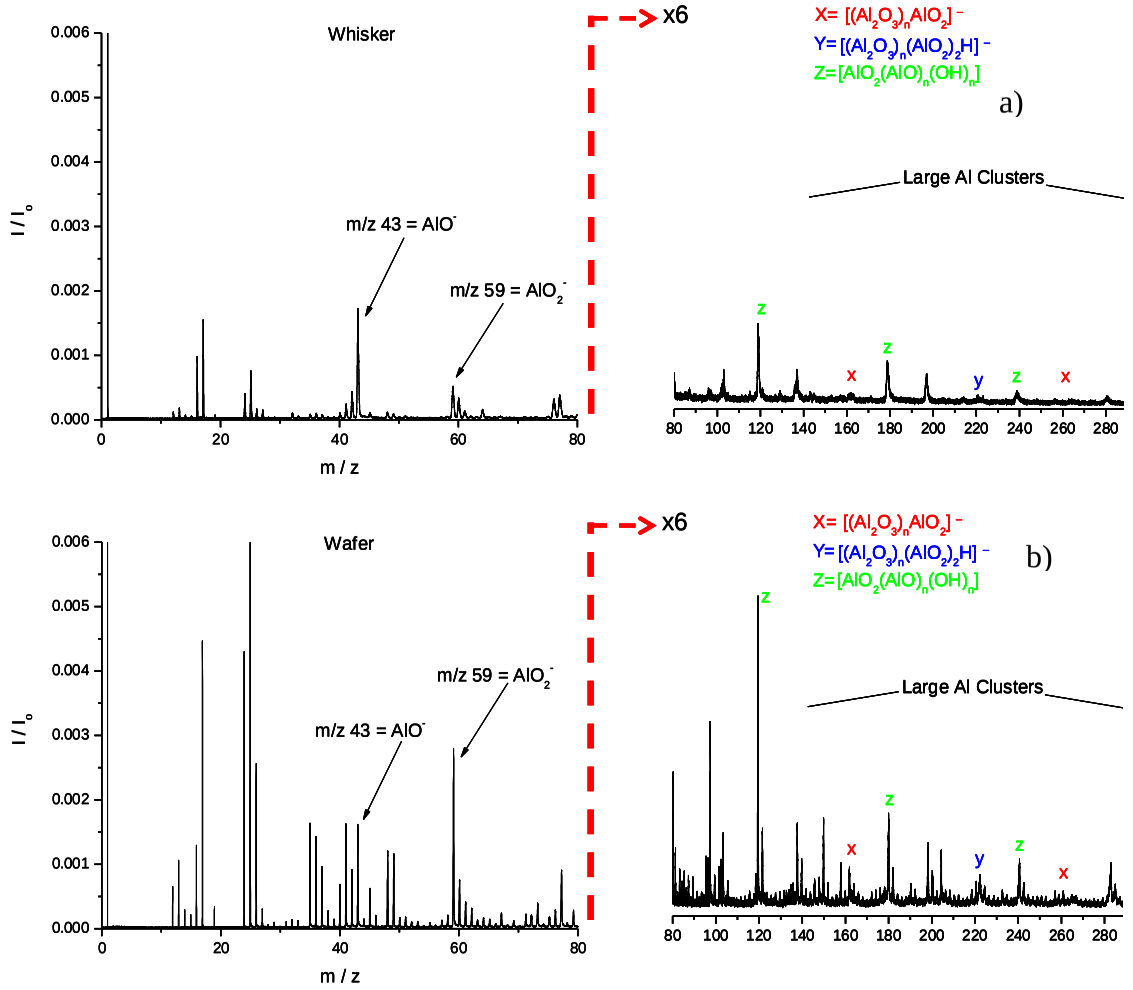

Figure 4-2. Negative secondary ion mass spectra resulting from impacts of 136 keV Au_{400}^{4+} on **a.)** free-standing Al nanowhiskers and **b.)** a bulk aluminum sample: Al-coated Si wafer. The intensities are normalized to the number of impacting projectiles (~2 million).

was ~40% of that obtained from bulk specimens. The lower SI yields are attributed to the nature of the whisker sample. Given the brush-like arrangement, electrons are more likely than SIs to escape from impacts at convoluted positions. Thus, electrons are detected, i.e. starts are recorded, without the detection of the corresponding SIs from the impact. The random loss of SI signal makes it impossible to determine quantitative differences between the samples without the use of the method described in the next section. However, even with this caveat, there is a difference in the relative abundances of AlO^- (m/z 43) versus AlO_2^- (m/z 59) from the whiskers and from the bulk sample (figures 4-2A,B). The ratio of the respective emissions of AlO^- and AlO_2^- is ~3 in the case of the whiskers and ~0.6 for the bulk samples (see table 4-1). For "infinite volume" targets of Al oxide, including boehmite, we observe a dominant occurrence of AlO_2^-. The "AlO^- exception" in the case of the whiskers is notable because its electron affinity[118] is lower than that of AlO_2^-. We hypothesize that the preeminence of AlO^- results from the fragmentation of energetic "chunks"[119] ejected from the whiskers. Even when utilizing projectiles smaller than Au_{400}^{4+}, remarkably, the diatomic ion emission dominates—regardless of the mode of projectile-solid interaction (linear collision cascades, collective effects[120], and hydrodynamic penetration[121]) and concomitant differences in projectile range and energy density (see table 4-2). All of the projectiles used in the bombardment of the whiskers have ranges greater than the diameter of the whisker, thus there is incomplete energy deposition in the confined volume (2 nm dia. whisker). Indeed, even in the case of Au_{400}^{4+}, whose penetration depth is the smallest of the projectiles employed in this study, the range in boehmite is estimated at $\geq$10 nm

Table 4-1. Ratio of negative secondary ion yields of AlO^- and AlO_2^- for confined-volume sample (whisker) and bulk samples (nanoparticles, powder, wafer).

	Whiskers Yields	Nanoparticle Yields	Powder Yields	Wafer Yields
AlO^- / AlO_2^-	2.8	0.5	0.6	0.6

Table 4-2. The percentage of the total detected secondary ion emission due to emission of the small mass SI AlO^- for various projectiles.

	E/at (keV/Au)	Atoms/Å^2	(Y AlO^- / Tot Y) = % Whisker	Nano-particles	Powder
Au_{400}^{4+}	0.34	0.47	37.0	12.9	17.6
Au_9^+	3.77	0.12	38.6	12.3	16.8
Au_3^+	11.3	0.075	54.4	9.7	15.4
Au_1^+	34	0.028	37.7	16.8	38.2

based on range measurements in carbon foils[113]. The remainder of the energy not deposited into the whisker is partially retained by the projectile as kinetic energy, partially transferred to the emitted secondary species as kinetic energy and also converted into internal energy of the emitted matter. The excitation of the sputtered products causes their fragmentation and thus increases the yield of the fragmentation species AlO^-. The emission of AlO^- is highest (~50% of the total SI yield) for Au_3^+ impacts. Thus, among the projectiles employed, the impact at 11.3 keV/Au and at 0.075 atoms/Å [121] caused the emission of the highest energy density ejecta from the truncated volume. The hypothesis that higher energy density ejecta lead to increased fragmentation products (including AlO^-) is supported by the shift in the secondary ion mass distribution described in the following section.

b. Secondary Ion Yields. The high mass region in figure 4-2 shows SIs due to three groups of aluminum oxide clusters with the following repeating units: $[(Al_2O_3)_nAlO_2]^-$, $[(Al_2O_3)_nOH]^-$, and $[AlO_2(AlO)_n(OH)_n]^-$. Our observations are in line with earlier studies[105, 122-126] which showed a monotonic decrease in the abundance of the clusters for n≥3. An illustration of one of the cluster series is shown in figure 4-3. The SI mass distribution for $[(Al_2O_3)_nAlO_2]^-$ is presented as the yield (*Y*), which is defined by:

$$Y = \sum_x \frac{x \cdot N_x(x)}{N_T} = \sum_x xP(x) \qquad \text{Eq. 4-1}$$

where x is the number of secondary ions detected simultaneously for a given species ($0 \leq x \leq 8$) from a single impact; N_x is the number of events (impacts) where ions x were

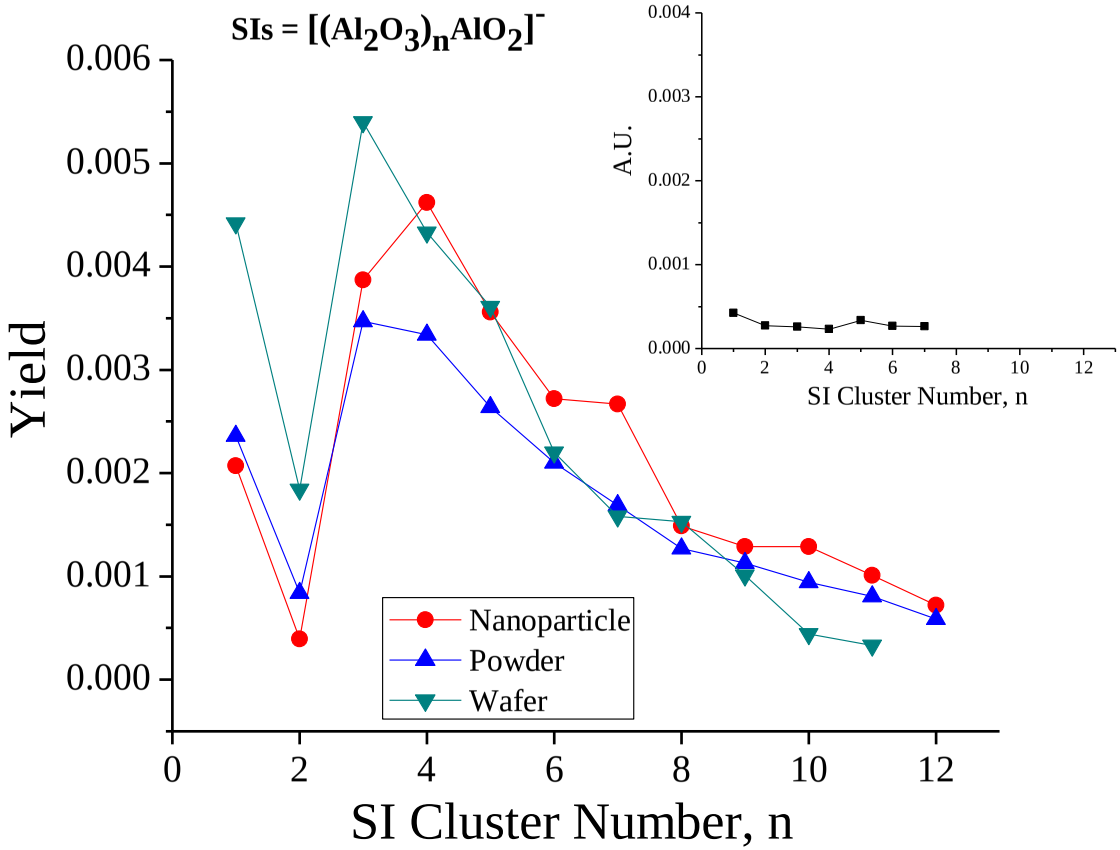

Figure 4-3. Trends in the secondary ion yield as a function of the integer n for a typical SI cluster series emitted from boehmite: $[(Al_2O_3)_nAlO_2]^-$. Yields for the whiskers are shown in the inset.

detected simultaneously; N_T is the number of incident projectile ion impacts; and *P(x)* is the probability distribution of the number of SIs detected per single impact event[3]. The SI yields for the bulk samples, including for the 50 nm nanoparticle are plotted in figure 4-3. The corresponding data from the whiskers are presented in the insert with an arbitrary y-scale. While the latter are much lower than those from the bulk samples, a quantitative comparison cannot be made for reasons outlined earlier (the brush-like structure of the whiskers). However, the difference in the relative abundances of the successive clusters from the bulk and the whiskers is revealing. In the latter, there is little variation in the relative yields from n=3 to n=7. In contrast, the yield for the same species produced from bulk samples show a monotonic decrease. The relative abundances of these large secondary ions are similar for all of the bulk samples. The comparatively low abundance of the n=2 cluster has been observed in other experiments with aluminum surfaces[122]. Similar trends are observed with Au_9^+ impacts, though the yields of all ions are significantly reduced. Au_3^+ and Au^+ projectiles are not efficient for the production of high-mass secondary ions.

c. Effective Yields. For a quantitative comparison between the bulk and confined-volume samples, the SI yield has to be defined for emission under comparable conditions. Comparisons can be made between flat and brush-like samples via the "effective" yield, Y_{eff}, which measures the yield of a given SI emitted in events where another selected SI is also emitted. This approach[3, 33, 45] side-steps the issue of computing a yield based on detecting projectile impacts from electron emission as follows. When a single impact event causes the emission of two types of ions, A and B,

the probability of observing these two types of ions in coincidence, assuming the ions are emitted independently of one another, is

$$\sum_{x_A}\sum_{x_B} x_A x_B P(x_A x_B) = \sum_{x_A} x_A P(x_A) \sum_{x_B} x_B P(x_B) \qquad \text{Eq. 4-2}$$

where x_A and x_B are the number of secondary ions detected simultaneously for species A and B, respectively, $P(x_A x_B)$ is the probability distribution of the number of ions A and B detected simultaneously and $P(x_A)$ and $P(x_B)$ are the probability distributions of detecting ions A and B individually. Given that

$$\sum_{x_A}\sum_{x_B} x_A x_B P(x_A x_B) = Y_{A,B} \qquad \text{Eq. 4-3}$$

where $Y_{A,B}$ is the experimentally detected coincidental SI yield, and

$$\sum_{x_A} x_A P(x_A) = Y_A \qquad \text{Eq. 4-4}$$

where Y_A is the SI yield for ion A, then it follows that the coincidental yield of ions A and B is

$$Y_{A,B} = Y_A \cdot Y_B \qquad \text{Eq. 4-5}$$

and thus, the effective yield for an ion A ($Y_{eff,A}$) can be expressed as

$$Y_{eff,A} = \frac{Y_{A,B}}{Y_B} \qquad \text{Eq. 4-6}$$

Recalling the brush-like arrangement of the whiskers, Y_{eff} is, in practice, a measure of the SI yield from a free-standing nano-object. The effective yields for AlO^- and AlO_2^- are presented in table 4-3, based on the co-emission with various SIs from Au_{400}^{4+} impacts. The effective yields for both species are approximately similar in all bulk samples, within the uncertainty of the experimental measurements (± 10%).

Table 4-3. Effective yields for a) AlO^- and b) AlO_2^- calculated in coincidence with various secondary ions. The precision of the values reported is ± 10%. The conventional secondary ion yield from the Al wafer sample is presented at the right for reference.

a)

Effective Yields for AlO^-					
Whiskers	**Nanoparticle**	**Powder**	**Wafer**	**Ion**	Wafer SI Yield
0.19	0.03	0.06	0.04	H^-	0.193
0.23	0.05	0.08	0.05	OH^-	0.040
0.23	0.04	0.06	0.04	C_2H^-	0.129
0.24	0.05	0.04	0.04	$C_2H_2^-$	0.031
0.24	0.05	0.06	0.05	Al^-	0.003
0.25	0.04	0.07	0.05	AlO_2^-	0.057
0.30	0.04	0.06	0.05	$AlO_3H_2^-$	0.021
0.32	0.04	0.06	0.04	$Al_2O_3H^-$	0.006
0.26	0.04	0.07	0.05	$Al_3O_7H_4^-$	0.007
0.25	0.04	0.05	0.04	$Al_5O_9H_2^-$	0.009
0.95	0.05	0.01	0.03	$Al_6O_{11}H_3^-$	0.002
0.15	0.15	0.03	0.04	$Al_7O_{12}H_2^-$	0.003

b)

Effective Yields for AlO_2^-					
Whiskers	**Nanoparticle**	**Powder**	**Wafer**	**Ion**	Wafer SI Yield
0.09	0.07	0.08	0.07	H^-	0.193
0.11	0.09	0.11	0.08	OH^-	0.040
0.10	0.08	0.08	0.07	C_2H^-	0.129
0.10	0.08	0.06	0.07	$C_2H_2^-$	0.031
0.11	0.10	0.09	0.09	Al^-	0.003
0.10	0.09	0.11	0.08	AlO_2^-	0.057
0.07	0.08	0.09	0.07	$AlO_3H_2^-$	0.021
0.11	0.08	0.08	0.06	$Al_2O_3H^-$	0.006
0.08	0.08	0.10	0.07	$Al_3O_7H_4^-$	0.007

Remarkably, the effective yields are roughly the same regardless of the coincidentally emitted SI used for the computation. Thus, while AlO^- or AlO_2^- and other SIs are co-emitted from a single impact, the emission of one does not affect the emission of the other, i.e. their emissions are not correlated. However, when comparing the bulk samples to the confined-volume sample, the yields differ. First, the effective yield for AlO^- is significantly higher for the whisker sample, regardless of the species selected as a co-emitted ion. This is not the case with the effective yields for AlO_2^-, where the whisker and bulk samples have similar effective yields. In the case of Au_9^+ impacts, the effective yields (data not shown) are approximately one order of magnitude lower, indicating that Au_{400}^{4+} is a more efficient projectile, even in a restricted-volume sample like the whiskers. Again, the higher AlO^- yield for the whiskers impacted by Au_{400}^{4+} is remarkable considering the electron affinities for AlO^- and AlO_2^-. As noted, the effective yields for AlO^- are approximately constant, which again implies the absence of correlation between the emission of AlO^- and the other Al-containing SIs. One exception is the surprisingly high effective yield for AlO^- when co-emitted with m/z 341. This result suggests a chemical correlation between these two coincidentally emitted SIs, perhaps indicating a preferred fragmentation pathway of large energetic "chunks" of matter.

By rearranging equation 4-6, the effective SI yield for the ion, A, co-emitted with AlO^- can be determined, as follows:

$$Y_{eff,A} = \frac{Y_{A,AlO^-}}{Y_{AlO^-}} \qquad \text{Eq. 4-7}$$

The pertinent data are presented in table 4-4. The effective yields from the whiskers are, for some coincidentally emitted SIs, comparable to those from bulk samples, yet for other cases of co-emission, they are very different. While the effective yields of AlO_2^- remain constant (within the uncertainty of the experimental measurements) from sample to sample, the emission of Al^- is much higher in the whiskers compared to the bulk samples. The preeminence of Al^- and AlO^- from the confined-volume sample again suggests the ejection of energetic "chunks" of matter which undergo extensive fragmentation, to the point of preferentially emitting atomic and diatomic SIs.

Conclusion

The nanowhiskers represent a first example of sample-size effects in SIMS. The effective SI yields show that a massive projectile like Au_{400}^{4+} is best for generating a signal from vanishingly small amounts of analyte. The scope of the information is affected by the shift in the SI distribution. The latter is a consequence of incomplete projectile energy deposition, regardless of the type of projectile used.

In the case of boehmite, the sample size limit where the SI mass distribution shifts toward the low-mass region is between 2 and 50 nm. In the 50 nm nanoparticles, we observe bulk-like SI emission, i.e. in a case where the size of the object sampled is ~250 times larger than the estimated ~10^3 nm^3 emission volume for 136 keV Au_{400}^{4+} impact[3]. Further experiments are needed to determine the boundaries of an object's volume and chemical composition for obtaining "bulk-like" SI emission.

SIMS with massive projectiles run in the shot-by-shot mode offers a distinct combination of features for the characterization of nanometric-size objects. SI yields are

Table 4-4. Effective yields for secondary ions (x) selected in coincidence with a) AlO^- and b) AlO_2^-. The precision of the values reported is ± 10%. The conventional secondary ion yield from the Al wafer sample is presented at the right for reference.

a)

Effective Yields for Ion (x) co-emitted with AlO^-

Whiskers	Nanoparticle	Powder	Wafer	Ion (x)	Wafer SI Yield
0.174	0.214	0.309	0.242	H^-	0.193
0.119	0.080	0.154	0.058	OH^-	0.040
0.082	0.083	0.157	0.165	C_2H^-	0.129
0.018	0.018	0.024	0.042	$C_2H_2^-$	0.031
0.015	0.003	0.004	0.006	Al^-	0.003
0.088	0.093	0.117	0.079	AlO_2^-	0.057
0.084	0.020	0.020	0.030	$AlO_3H_2^-$	0.021
0.021	0.007	0.010	0.008	$Al_20_3H^-$	0.006
0.026	0.011	0.019	0.010	$Al_3O_7H_4^-$	0.007
0.009	0.012	0.006	0.010	$Al_5O_9H_2^-$	0.009
0.004	0.005		0.002	$Al_6O_{11}H_3^-$	0.002
0.003	0.006	0.001	0.003	$Al_7O_{12}H_2^-$	0.003

b)

Effective Yields for Ion (x) co-emitted with AlO_2^-

Whiskers	Nanoparticle	Powder	Wafer	Ion (x)	Wafer SI Yield
0.216	0.194	0.269	0.235	H^-	0.193
0.161	0.071	0.138	0.054	OH^-	0.040
0.095	0.075	0.135	0.154	C_2H^-	0.129
0.022	0.015	0.019	0.038	$C_2H_2^-$	0.031
0.019	0.003	0.004	0.005	Al^-	0.003
0.274	0.044	0.069	0.043	AlO^-	0.057
0.053	0.020	0.020	0.027	$AlO_3H_2^-$	0.021
0.019	0.006	0.009	0.007	$Al_20_3H^-$	0.006
0.023	0.010	0.017	0.008	$Al_3O_7H_4^-$	0.007

high, thus assays can be based on co-emitted SIs. In this approach, one measures the effective SI yields which reflect the comparative amounts of matter in individual nano-objects. Finally, since the nano-objects are examined one-by-one, variation in composition may be revealed, i.e. their classification based on individual tests appears feasible. This idea will be discussed in more detail in the next chapter.

CHAPTER V

LOCATION-SPECIFIC MOLECULAR IDENTIFICATION OF INDIVIDUAL NANO-OBJECTS*

Introduction

The characterization of single nano-objects beyond their size and shape is limited by the capabilities of current analytical techniques[48, 127]. Chemical information has been obtained via laser-based methods on atmospheric particles[128] and aerosols[49] and in some cases has been shown to interrogate spots well below the optical diffraction limit[129]. A limitation of these characterization techniques, however, is that they provide only elemental chemical information. Recently, we reported a sample-size effect when secondary ion mass spectrometry (SIMS) is applied on nano-objects too small for full projectile energy deposition[130]. We present here a SIMS methodology capable of extracting molecular information from individual nano-size objects in a binary mixture. In this technique, the nano-objects are bombarded with a sequence of individual projectiles resolved in time and space, in the present case Au_{400}^{4+} of 136 keV impact energy. The secondary ions ejected from each impact are identified with time-of-flight mass spectrometry and recorded individually. This mode of operation allows for the identification of single nano-objects because they are sampled one-at-a-time. We present below the first evidence of quantitative molecular information originating from a

*Parts of this chapter are reprinted with permission from *Analytical Chemistry*, Veronica T. Pinnick, Stanislav V. Verkhoturov, Leonid Kaledin, Yordanos Bisrat and Emile A. Schweikert, Location Specific Molecular Identification of Individual Nano-Objects, *ASAP Article*. Copyright [2009] American Chemical Society.

mixture of nano-whiskers and nano-spheres.

The nano-whiskers examined in this study have been described elsewhere[131]. The TEM image (fig. 5-1a) shows the nano-alumina whiskers bonded to an underlying 600 nm glass fiber. X-ray diffraction patterns identified the nano-alumina as predominantly a crystalline aluminum oxyhydroxide[132] with the mineralogical name of boehmite[3]. The second type of nano-objects examined are polystyrene nanospheres, 30 nm in diameter suspended in water solution. SEM of a thick layer of polymer spheres (fig. 5-1b) confirms the particle diameter. A dilute suspension of the spheres was drop-cast onto the surface of the whisker sample, and the corresponding SEM image (fig. 5-1c) verifies that a relatively even layer of spheres forms, with some areas of particle accumulation. This preparation provided a test case for the characterization of mixture of nano-objects: whiskers and spheres.

Experimental Section

a. Preparation of Whiskers. The preparation of the commercially available NanoCeram filters (Argonide Corp.) has been previously documented[131]. Briefly, 6 g of microglass fibers (Lauscha Fiber International) were dispersed in permeate from a reverse osmosis water generator, using a kitchen style blender. Quantity of 1.8 g of aluminum powder (Atlantic Equipment Engineers) was added to microglass. Ammonium hydroxide was added to initiate the reaction of aluminum with water to form the AlO(OH) and hydrogen. The mixture is heated to boiling and kept at boiling until the mixture is milky white, and then cooled and neutralized to approximately pH 7. The

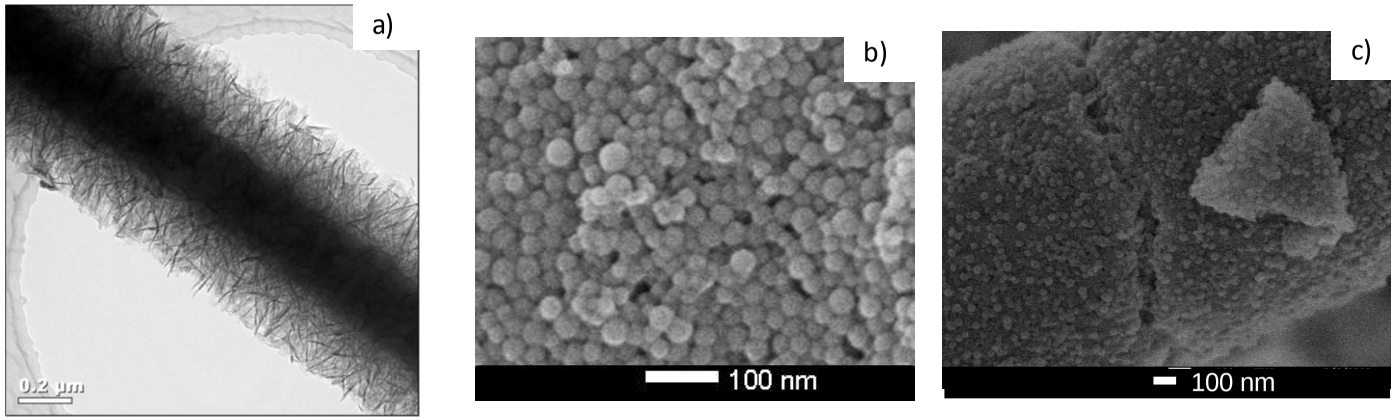

Figure 5-1. a) TEM image of nano-alumina whiskers bonded to a silicon oxide microfiber (image obtained from L. Kaledin, Argonide Corp.), **b)** SEM image of bulk deposition of ~30nm polystyrene spheres, **c)** SEM image of polystyrene spheres on the surface of the alumina whiskers (images in b and c obtained from Y. Bisrat, MCF, Texas A&M).

result is nano alumina formed onto the coarser fiber with a composition of 40 w/w% Nanoalumina whisker/60 w/w% microglass. A non-woven media is formed by conventional wet-laid paper making technology. Sheets (30 cm x 30 cm, 0.8 mm thick) were prepared, and then 6 mm diameter discs were cut out of the sheet.

b. Preparation of Droplets. Whisker samples containing intact polystyrene nanospheres were prepared by sonicating then depositing 10 μL of a suspension of 30 nm particles, 1% (w/w) in water (Duke Scientific, Palo Alto, CA) onto 6 mm diameter, 0.8 mm thick discs. Samples were affixed to stainless steel supports with conductive carbon tape for ToF-SIMS and SEM measurements.

c. Preparation of Flakes. Polymer flakes on alumina whiskers were also obtained already prepared by the Argonide Corp. Their preparation was reported by the manufacturer as follows. 0.4 mL of 30 nm undeluted latex microsphere suspension was mixed with 40% nanowhisker / 60% microglass mulch (~ 0.5 g in 1 L of water at pH 7). The samples were mixed by hand, with a dwell time of 10 minutes. Discs were formed with a diameter of 4 cm. Smaller discs were punched out of this sample as needed for sample holders. In all the preparations of nano-objects, replicate samples were prepared and affixed to stainless steel supports for both ToF-SIMS and SEM measurements.

d. Electron Microscopy Measurements. Scanning electron microscope (SEM; Jeol – 7500F Cold Field Emission) was used to study the morphology of the surface of the whiskers before and after polymer spheres were deposited. All SEM images were obtained by Dr. Yordanos Bisrat at the materials characterization facility (MCF) at Texas A&M University. Images are all secondary electron images obtained at working

distances 4.5-14 mm and accelerating voltages 1.5-5 kV, depending on the sample. Samples to be analyzed were halved, one half for SEM analysis, one half for SIMS analysis. Because the polymer spheres are insulators, whisker samples with polymer spheres and bulk polymer samples were sputter-coated (Cressington 208HR) with ~2nm of Pt/Pd for increased conductivity for SEM analysis only. The TEM image shown in figure 5-1a was provided by the whisker manufacturer (Dr. Leonid Kaledin, Argonide Corporation).

Results and Discussion

a. Spheres on Whiskers. Samples were analyzed using secondary ion mass spectrometry run in the event-by-event bombardment/detection mode. Negative ions were monitored and recorded from each single 136 keV Au_{400}^{4+} impact. Figure 5-2 shows the negative secondary ion (SI) mass spectra for a) the nanoalumina whiskers alone, b) a thick layer of the polystyrene nanoparticles alone, and c) a sample of the nano-whiskers with a small volume (~5 μL) of nanoparticles drop cast onto the surface. The whisker negative ion mass spectrum (fig. 5-2a) illustrates the emission of aluminum oxide-based secondary ions. As previously observed with the whisker samples[130], there is a shift in the mass distribution of SIs toward lower masses (AlO^-, AlO_2^-) compared to emission from bulk aluminum surfaces. The unusual predominance of AlO^- has previously been reported as sample-size effect, where the confined volume of the nano-object is too small for full projectile energy deposition. Some emission of carbon-based clusters is due to surface contamination; these fragments are most abundant in the small mass range (≤40 Da). A thick sample of polymer spheres (fig. 5-2b) shows emission of

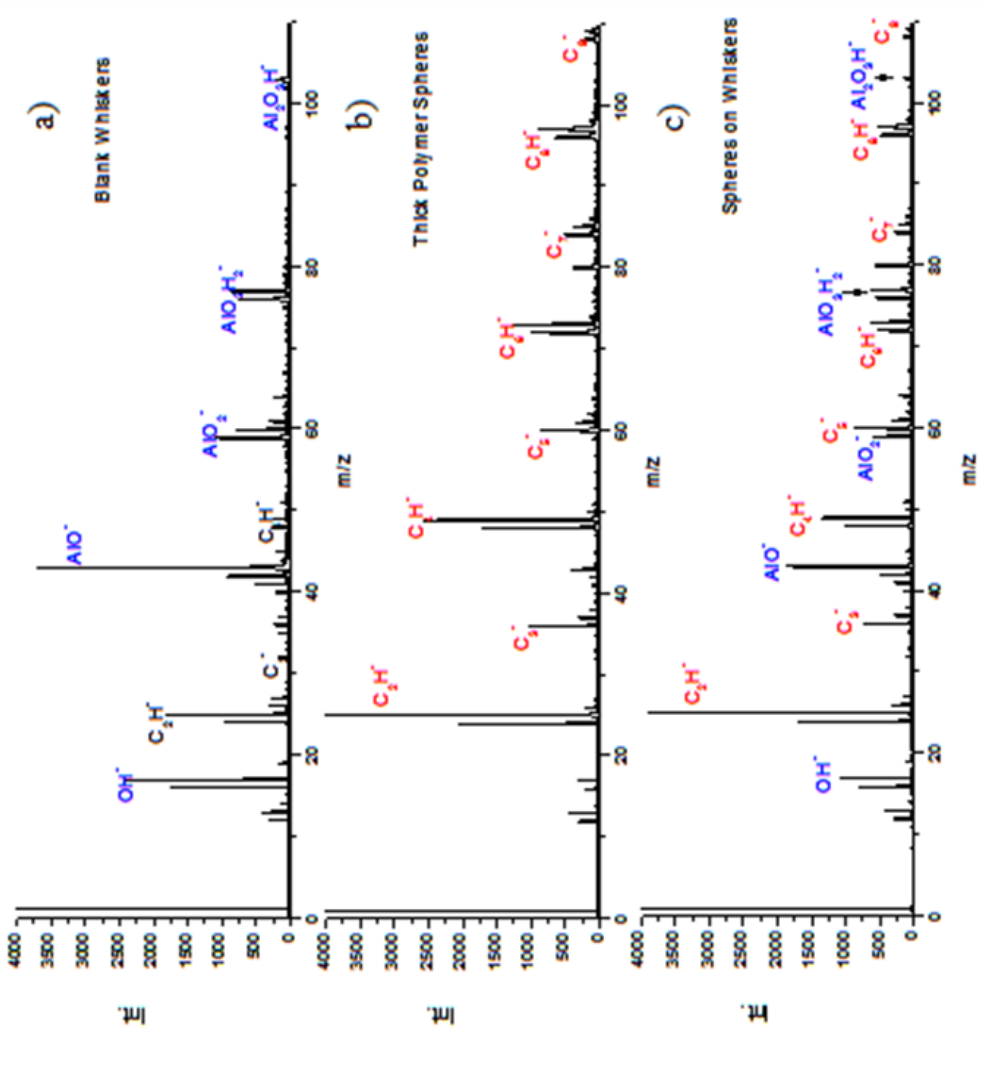

Figure 5-2. Total negative secondary ion mass spectrum of **a)** bare boehmite alumina whiskers, **b)** thick layer of polystyrene nano-spheres (~30 nm diameter), **c)** polystyrene nano-spheres deposited on the surface of the boehmite whiskers (less than a monolayer).

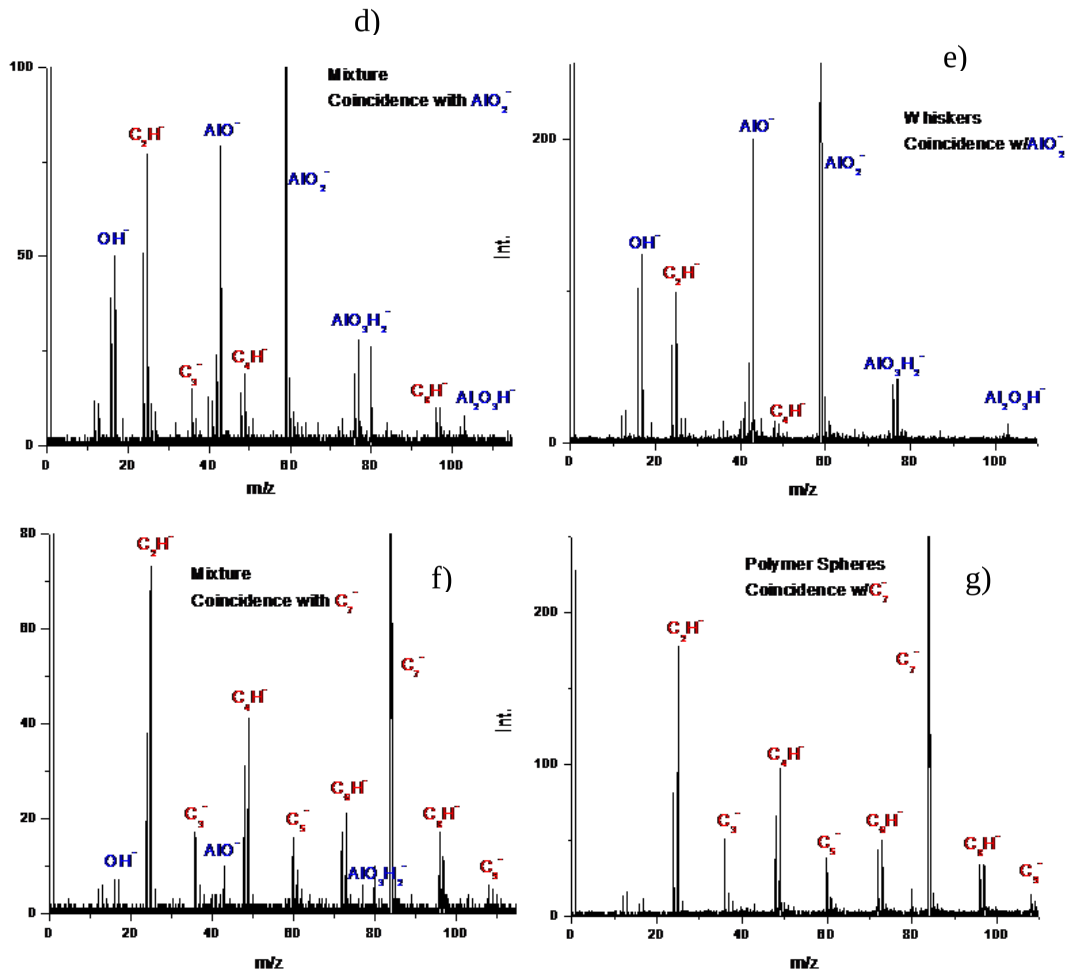

Figure 5-2. (Continued) **d)** AlO_2^- coincidence mass spectrum (obtained from part c) for nano-object mixture. **e)** AlO_2^- coincidence mass spectrum (obtained from part a) for bulk whiskers. **f)** C_7^- coincidence mass spectrum (obtained from part c) for nano-object mixture. **g)** C_7^- coincidence mass spectrum (obtained from part b) for bulk spheres.

carbon based SI clusters C_n^- and C_nH^- where $1 \leq n \leq 22$. Generally, for even values of n, clusters of C_nH^- predominate over the C_n^- type. The trend is reversed for odd n carbon clusters. The SI spectrum for the mixed nano-object system (fig. 5-2c) represents emission from both nano-objects—as both polystyrene and aluminum based secondary ion emission is detected. Inspection of the peak areas of AlO^- and AlO_2^- (fig. 5-2c) reveals that they are in the same ratio (~2.7) as when nanowhiskers are sole free-standing objects (fig. 5-2a). Thus, the summation of individual impacts (fig. 5-2c) includes emissions from nanowhiskers unaffected by the presence of polystyrene.

b. Coincidence Mass Spectra. More insight into the impact/emission events on specific nano-objects can be gained when examining the data obtained from the event-by-event bombardment/detection mode. In this approach, we can identify the SIs that are co-emitted from a single impact (the resulting crater is hemispherical with diameter of ~10 nm[3, 111, 133, 134]. Coincidental emission implies co-localization within this nanovolume. Let's consider the data from the mixed nanoparticle-nanowhisker sample in fig. 5-2c. The subset of impacts pertaining to emission of AlO_2^- is shown in fig. 5-2d. This coincidence ion mass spectrum compares well with that of SIs co-emitted with AlO_2^- from the blank whiskers (fig. 5-2e). There is little evidence in fig. 5-2d of SIs that may have originated from polystyrene spheres surrounding the whiskers. Conversely, when extracting from the mix of whiskers and spheres the mass spectrum of the Sis co-emitted with C_7^- (fig. 5-2f), one obtains a replica of the corresponding coincidence mass spectrum from a thick layer of polystyrene spheres (fig. 5-2g).

An SEM image of the sample with polystyrene spheres on the whisker-coated fibers (fig. 5-3) shows that the spheres are dispersed. The spectrum in fig. 5-2f is thus from individual spheres. Recalling its similarity with C_7^- co-emission mass spectrum from a thick layer of polystyrene spheres (fig. 5-2g), we infer that a solid 30 nm polymer sphere is large enough for full projectile energy deposition. Further, the virtual absence of SIs due to the alumina whiskers indicates that the emission recorded in fig. 5-2f are from spheres that are located at the top of the whiskers. The top location may be due to an electrostatic effect at the whisker tips. An electrostatic whisker-particle interaction has been previously observed with silicon nanoparticles[131]. We have noted earlier that the SI emission from the whiskers is affected by their small diameter. The SIs co-emitted with AlO_2^- (fig. 5-2d) are a replicate of those observed from blank whiskers (fig. 5-2e) which have been described as emissions from individual free-standing whiskers[130]. The notable observation is that SI emission from nano-objects can reflect their physical orientation/location in addition to effects due to confined dimensions.

c. Nano-Object Size and Composition. Given the sensitivity to nanoparticle dimensions, the event-by-event bombardment/detection mode of mass spectrometry can give insight into the structural integrity and composition of an object without the use of visualization by techniques such as microscopy. To demonstrate this point, a sample was prepared with the same components as used previously: alumina whiskers and polystyrene spheres. The sample preparation was varied such that the polymer spheres reacted with the whiskers to produce a nano-composite material. Bohemite alumina whiskers have been shown in the past to be extremely reactive, due to their electrostatic

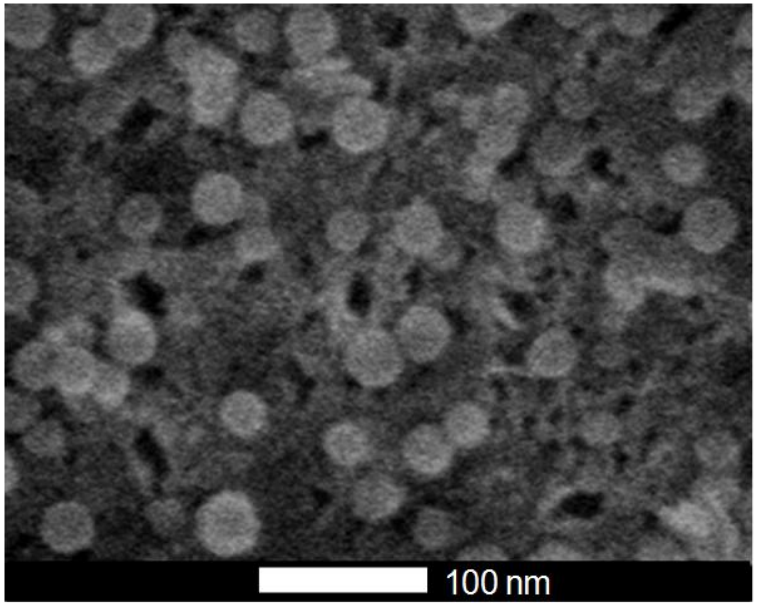

Figure 5-3. SEM image of polymer nano-spheres deposited on whisker surface (less than a single layer deposited) (image obtained from Y. Bisrat, MCF, Texas A&M).

nature[135]. Figure 5-4a shows the SEM image of the polymer "flakes" on the whisker surface.

The SI mass spectrum for the polymer flakes on whiskers is presented in figure 5-4b. Again, hydrocarbon peaks related to the flakes and aluminum oxide peaks relating to the whiskers are detected. There are qualitative differences between the spectrum representing polymer flakes (fig. 5-4b) and the spectrum representing the spheres (fig. 5-2c). The ratio of AlO^- and AlO_2^-, which is one indicator used to monitor sample-size dependent SI emission, shows a shift from ~2.8 observed with the sphere on whisker sample to ~0.8 observed with the flakes. Further, the overall secondary ion emission from hydrocarbon species is on average 2-3 times lower for the flakes than from the polymer spheres. The coincidence spectra also suggest that the individual alumina and polymer spectra cannot be extracted as was the case for the spheres. Fig. 5-4 c shows the coincidence spectrum for all ions co-emitted with AlO_2^-. Here, while the majority of the high-intensity peaks originate from alumina, there is still notable contribution from the polymer. Likewise, the coincidence spectrum for all ions co-emitted with C_6H^- shows contribution from the whiskers. The inability to separate the individual mass spectra for each component implies that these components are not segregated on the scale of a single impact.

For a better understanding of the morphology of the spheres and the flakes, quantitative information can be obtained from the event-by-event bombardment/detection mode of operation. To determine the correlation between coincidentally emitted ions, a correlation coefficient can be calculated from the

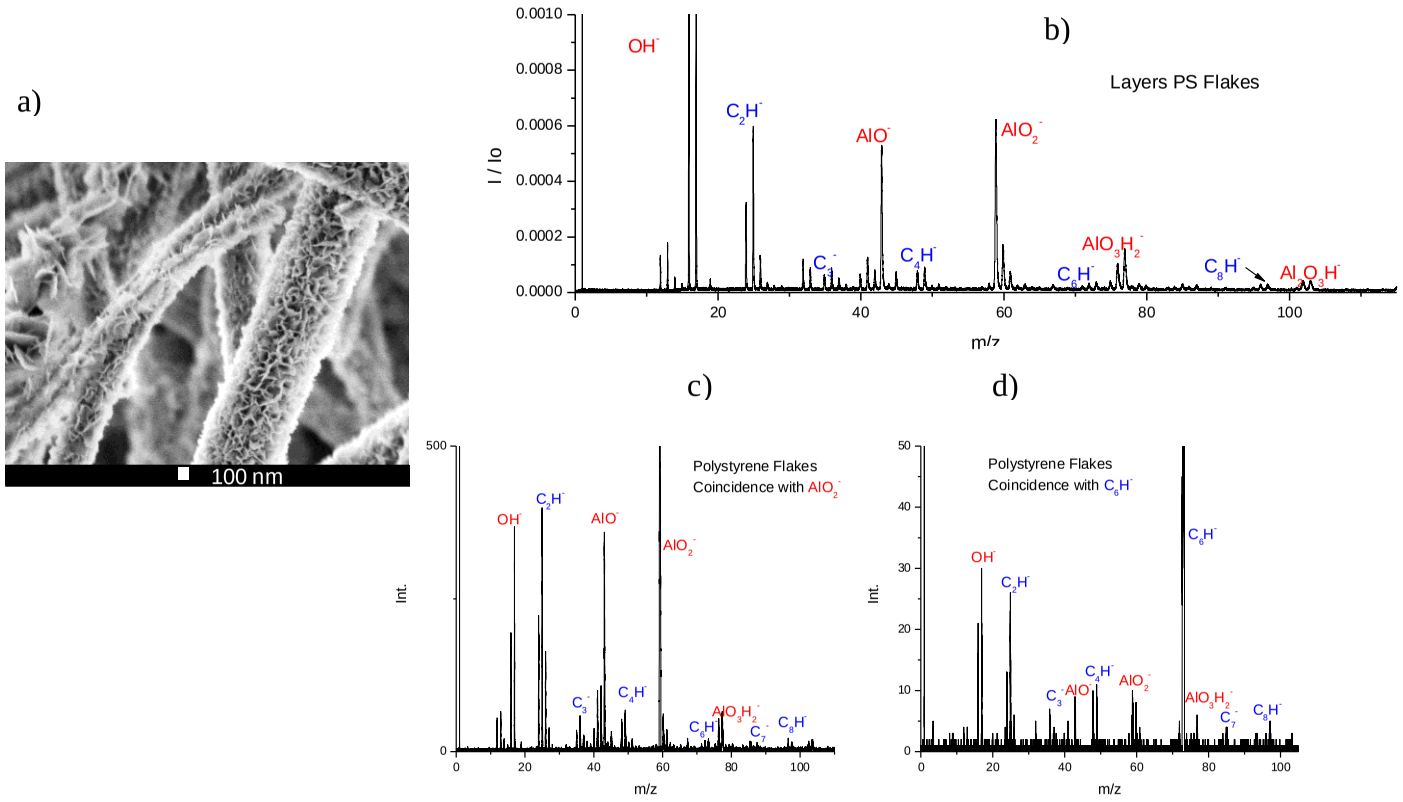

Figure 5-4. **a)** SEM of flake structure on whiskers (image obtained by Y. Bisrat, MCF, Texas A&M), **b)** total negative ion mass spectrum of flakes, **c)** spectrum of ions in coincidence with AlO_2 d) spectrum of ions in coincidence with C_7.

experimental data. When a single impact event causes the emission of two types of ions, A and B, the probability of observing these two types of ions in coincidence, assuming the ions are emitted independently of one another, is

$$\sum_{x_A}\sum_{x_B} x_A x_B P(x_A x_B) = \sum_{x_A} x_A P(x_A) \sum_{x_B} x_B P(x_B) \qquad \text{Eq. 5-1}$$

where x_A and x_B are the number of secondary ions detected simultaneously for species A and B, respectively, $P(x_A x_B)$ is the probability distribution of the number of ions A and B detected simultaneously and $P(x_A)$ and $P(x_B)$ are the probability distributions of detecting ions A and B individually.

Given that

$$\sum_{x_A}\sum_{x_B} x_A x_B P(x_A x_B) = Y_{A,B} \qquad \text{Eq. 5-2}$$

where $Y_{A,B}$ is the experimentally detected coincidental SI yield, and

$$\sum_{x_A} x_A P(x_A) = Y_A \qquad \text{Eq. 5-3}$$

The correlation coefficient, Q, is defined by:

$$Q_{A,B} = \frac{\sum_{x_A}\sum_{x_B} x_A x_B P(x_A x_B)}{\sum_{x_A} x_A P(x_A) \sum_{x_B} x_B P(x_B)} = \frac{Y_{AB}}{Y_A Y_B} \qquad \text{Eq. 5-4}$$

If the emission of ions A and B is uncorrelated, i.e., A and B are emitted independently within the single impact/emission event, then the distribution $P(x_A x_B)$ is equal to $P(x_A)P(x_B)$, which results in $Q_{AB} = 1$. When the emission of ions A and B is correlated, implying that emission events that are favorable for the emission of ion A are also favorable for ion B, then $Q_{AB} > 1$. If the emission of ion A and B are anti-correlated,

implying that events favorable for the emission of ion A are not favorable for B, then the value of the correlation coefficient, $Q_{AB} < 1$.

Table 5-1 shows the correlation coefficients for the polymer spheres on whisker substrate. The coincidence yields are calculated for species co-emitted with either AlO_2^- or C_7^-, likewise the correlation coefficients measure the correlation between species co-emitted with each of these ions respectively. Correlation coefficients calculated for two ions originating from the substrate (alumina) show correlation (i.e. Q > 1). The same is true for carbon-based SIs co-emitted from the polymer nanoparticle. The correlation coefficient between C_7^- and any of the aluminum-based peaks, however, is consistently less than unity. The same trend can be seen when calculating the correlation coefficient for carbon-based ions co-emitted with AlO_2^-, where Q < 1. This relationship suggests anti-correlation between the SIs emitted from the substrate and the nanoparticle. The physical significance of this result is that the quantitative information gathered by this methodology allows one to understand the relative dimensions of the individual nano-objects by monitoring the degree of separation of co-emitted species. In this case, impacts on polymer spheres result almost entirely in emission of carbon-based SIs, implying that the structure of the polymer sphere is large enough to encompass the total interaction volume between the projectile and the nanoparticle. Correlation coefficients for the polymer flakes on the whiskers are presented in table 5-2. The lack of segregation, as noted in the coincidence spectra, is again observed in the correlation coefficient data. All secondary ions, whether emitted from the polymer or from the

Table 5-1. Correlation coefficients (Q) for alumina-based and polymer-based secondary ions from intact polymer spheres on whiskers. Q>1 implies correlation, Q<1 implies anticorrelation.

	$Q\ (AlO_2^-)$	$Q\ (C_7^-)$
AlO^-	3.7	0.5
AlO_2^-	x	0.7
$AlO_3H_2^-$	2.8	0.5
C_6H^-	0.5	3.6
C_7^-	0.7	x
C_9^-	0.9	3.8

Table 5-2. Correlation coefficients (Q) for alumina-based and polymer-based secondary ions from polymer flakes on whiskers. Q>1 implies correlation, Q<1 implies anticorrelation.

	$Q\ (AlO_2^-)$	$Q\ (C_7^-)$
AlO^-	1.7	1.4
AlO_2^-	x	1.7
$AlO_3H_2^-$	1.6	1.5
C_6H^-	1.4	4.1
C_7^-	1.9	x
C_{10}^-	1.8	3.4

whisker, have correlated emission, (Q>1). This lack of segregation could be the result in the formation of a nano-composite material after the reaction of boehmite with polystyrene, or may simply be an indication that the flakes are not sufficiently large to encompass the entire emission volume from Au_{400}^{4+} impacts. It is evident that objects must be chemically and physically resolved in order to obtain separation of their mass spectral information.

d. Number of Effective Impacts. The ability to extract mass spectra from either the nano-whiskers or the polymer spheres allows further to estimate the relative abundance of a nano-object in the field of view. The effective number of incident projectile impacts (N_{eff}) on one component of a mixed system can be calculated as previously described[136]. Briefly, the SI mass distribution for a secondary ion, e.g. C_7^-, is presented as the yield (Y), which is defined by

$$Y_{C_7^-} = \frac{I_{C_7^-}}{N_T} \qquad \text{Eq. 5-5}$$

where $I_{C_7^-}$ is the number of C_7^- ions detected and N_T is the total number of primary ion impacts. When a single impact event causes the emission of two types of ions, e.g. C_7^- and C_9^-, the probability of observing these two types of ions in coincidence, assuming the ions are emitted independently of one another, is

$$P_{C_7,C_9} = P_{C_7} P_{C_9} \qquad \text{Eq. 5-6}$$

where $P(C_7,C_9)$ is the probability distribution of the number of ions C_7^- and C_9^- detected simultaneously and $P(C_7)$ and $P(C_9)$ are the probability distributions of detecting ions C_7

and C_9 individually. Given that, probabilities are extended to our experimentally detected SI yield

$$Y_{C_7,C_9} = Y_{C_7} Y_{C_9} \qquad \text{Eq. 5-7}$$

where $Y(C_7,C_9)$ is the experimentally detected coincidental SI yield. In the case of the emission from a two-component system, N_T must be modified to account for the number of projectiles that impact each component. As such, the number of effective impacts, N_{eff}, is used such that

$$\frac{I_{C_7,C_9}}{N_{eff}} = \left(\frac{I_{C_7}}{N_{eff}}\right)\left(\frac{I_{C_9}}{N_{eff}}\right) \qquad \text{Eq. 5-8}$$

where $I_{C7,C9}$ is the number of coincidentally emitted C_7^- and C_9^- ions. Thus, in order to calculate the number of effective impacts from a single component, two ions from the single component are selected to be monitored in coincidence. By rearranging equation 4, the number of impacts on a component can be determined

$$N_{eff} = \frac{I_{C_7} I_{C_9}}{I_{C_7,C_9}} \qquad \text{Eq. 5-9}$$

Here, we report the effective number of impacts as coverage coefficient[137, 138], *C.C.*, which is used as a measure of partial coverage of nano-objects. Experimentally, we define this term as a percentage of the total number of detected incident projectile impacts, N_T, i.e.

$$C.C. = \frac{N_{eff}}{N_T} \cdot 100\% \qquad \text{Eq. 5-10}$$

Using this concept, one can calculate the fraction of the whisker surface covered by the polymer nanospheres. The coverage coefficient for the polymer sphere, as determined by C_7^- and C_9^- co-emission, is 29%. C_7^- and C_9^- were selected to be monitored due to their specificity (i.e. their absence in the alumina whisker spectrum). The physical meaning of this *C.C.* calculation correlates directly to the actual coverage—the reported *C.C.* for the spheres implies that ~29% of the 2-dimensional whisker surface is covered by particles. This value is in agreement with the coverage calculated from a cursory examination of SEM images of this sample. For example, the SEM image in fig 5-3 shows sphere coverage of ~3.04×10^4 nm^2 and a total substrate area of ~1.10×10^5 nm^2, yielding a sphere coverage of ~28%.

Conclusion

The results described here are not unique to the highly efficient Au_{400}^{4+} incident projectile—in principle, any projectile (e.g. Bi_3^+, C_{60}^+, high charge state atomic ions) can be used to impact surfaces. The key requirements are that the individual projectile induces detectable multi-ion emission and that the ejecta are recorded from each individual impact. This mode of mass spectrometry probes one nano-domain at a time. When applied to nano-objects where the emission volume is confined, the nature and abundance of the ionized ejecta may differ from "bulk-like" SI emission. This technique is sensitive to nano-object dimensions as well as chemical composition. A key requirement in obtaining unique chemical information from a component is that the objects must be chemically and physically resolved. The ability to determine the relative abundance and extent of coverage of individual components in a mixture can only be

accomplished by sampling individual components. The single impact approach can be extended to more complex mixtures and may also be applied to monitor the changing chemical nature of nanoparticles (e.g. surfactant conversion) in order to monitor the relative abundance of these particles versus their unmodified neighbors.

CHAPTER VI

CONCLUSIONS

This study was devoted to massive cluster-SIMS on nano-object and nano-domains. The projectiles used (C_{60}, Au_{400}) offer notable advantages over bombardment with atomic ions or small clusters: enhanced emission of molecular ions, low damage cross-section, and reduced molecular fragmentation[2, 139]. Limitations arise with C_{60} and Au_{400} when examining μm and sub-μm size surface areas since these beams cannot be focused as well as keV ions. This limitation was side-stepped with a nano-volume technique where ionized ejecta are examined from single projectile impacts. Under these conditions, SI emission occurs from a volume of ~10^3 nm^3.

Biological Nano-Domains

As a first test case, we examined biologically-relevant nano-domains. One of the challenges of investigating biological systems with SIMS is exposing the system to the vacuum environment. To address this concern, we investigated mimetic cell membranes (solid-supported lipid bilayers) using polyethylene glycol (PEG) to protect the bilayer from disorganization at the air-water interface. PEG was demonstrated to protect bilayer organization both in the hydrated and dehydrated states. Though PEG resides on the bilayer surface, lipid SI emission is still observed, without significant hydrocarbon contribution in the spectrum.

Another challenge in SIMS bio-analysis is the limitation of our current instrumental design to investigate only negative ion emission. To this end, two methodologies were developed to run the instrument in the positive ion mode. Though

these methodologies are not optimal in terms of performance (e.g. mass resolution, etc.), they provided a cursory examination of biological systems. POPC bilayers were examined with and without PEG protection in the positive ion mode, and SIMS showed organization-dependent emission from the bilayer. Secondary ion yield ratios of phosphocholine head group ions and silicon substrate ions, as well as observation of the deprotonated molecule of POPC (m/z 760) provide insight into bilayer organization without the use of fluorophores.

One biological nano-domain system that of great interest in molecular biology is that of lipid rafts. To study this system, lipid rafts, formed in the presence of DPPC, POPC, and heptafluoro-cholesterol, were examined in solid supported lipid bilayers. By monitoring co-emission from C_{60}^{+} impacts, coincidence mass spectra were obtained for species co-emitted with cholesterol (F^{-}), lipid (PO_3^{-}) and the glass substrate (SiO_3H^{-}). Coincidence spectra showed some degree of separation of lipid and cholesterol components, which was verified by the correlation coefficient for each species. Calculation of the correlation coefficient showed anti-correlation between lipid and cholesterol peaks, implying that these two species segregate on the scale of the emission volume of a single C_{60}^{+} impact (~100 nm^3) [3]. While tagging molecules with extrinsic species (i.e. F) is not preferred, the proof-of-concept experiment showed that co-localization analysis using molecular information can be carried out with these systems.

The biological domains had, in our case, dimensions of ~1-2 um. A question which has been first addressed in this study is the response of massive cluster SIMS on nano-object and nano-domains of “sub-critical assay dimensions.” The fundamental

issue is to understand the interactions between the projectile and matter in a confined volume.

Free-Standing Nano-Objects

For the characterization of free-standing nano-objects using SIMS, it is important to understand the relationship between nano-object SI emission and that from bulk samples. Investigations of free-standing nano-objects with the event-by-event mode showed that finite volume samples exhibit sample-size dependent secondary ion emission. Nano-alumina whiskers with a diameter of ~2 nm were impacted with ~2 nm nanoparticles (Au_{400}^{4+}) and their secondary ion emission was compared to bulk alumina samples (wafer, foil, 50 nm nanoparticles) bombarded under the same conditions. Results showed that the mass distribution of secondary ions emitted from nano-whiskers shifted toward low mass species such as Al^- and AlO^-. The ratio of AlO^-/AlO_2^- shifted from ~0.8 in bulks to ~2.6 in whiskers. Large aluminum oxide cluster emission was significantly depressed from whisker samples compared to distributions observed from bulk species.

These results demonstrate the idea that nano-objects interrogated by SIMS cannot be directly compared to reference bulk samples. One method that can be used to compare these objects under the same conditions is by comparing the effective yields. Effective yields are calculated based on co-emission from a single impact. Using this concept, the shift in the mass distribution for whiskers toward lower mass species such as AlO^- was clearly demonstrated.

When free-standing nano-objects exist in a mixture, conventional secondary ion mass spectrometry (i.e. using a beam of incident projectiles) produces an "average" of the sample surface. The ability to extract an individual mass spectrum from nano-object mixtures was demonstrated using polystyrene particles (~30 nm) on the surface of nano-alumina whiskers and verified using coincidence spectra from blanks of the same materials. This technique, however, is sensitive to nanoparticle dimensions and relative locations. It has been observed that objects smaller than 5 nm shatter and recombine with substrate atoms. Likewise, polymer nano-flakes show a different morphology, and therefore a different coincidence spectrum. Also, since SIMS probes surface structures, nano-object buried within another object or beneath the surface cannot be effectively probed. Another feature which can be determined by monitoring co-emission is the number of effective impacts on a surface. Using this concept, the fractional coverage of was calculated. The SIMS calculation was in line with the coverage calculated from SEM measurements.

Future Work

Little is known regarding the investigation of individual nano-objects using mass spectrometry, especially investigations with free-standing nano-objects. Further experiments should first focus on fundamental questions regarding emissions from nano-objects compared to chemically identical bulk specimens. It has been observed that nanoparticles smaller than 5 nm shatter and recombine with substrate atoms. Nanoparticles larger than 30 nm allow for a complete separation of coincidental signal, and objects larger than 50 nm yield a mass distribution similar to bulk species. A study

should be conducted to identify the nano-object size requirement to exhibit full projectile energy dissipation. In other words, what are the "critical assay dimensions"?

Another question that remains to be answered is that of electron emission from nano-objects. Since many of the observations made in this work rely on the electron emission to signal the arrival of the projectile onto the sample surface, and further to act as a start signal for time of flight analysis of the secondary ions, it is critical to understand if the electron yields and kinetic energies emitted from bulk surfaces are comparable to those emitted from nano-objects. An instrument capable of monitoring electron emission from single impacts and mapping electron distributions is available in our laboratory. Since secondary ion emission is affected by the dimensions of the objects studied, future experiments should investigate sample size effects on the electron emission. Nano-objects should be free standing, and range in sizes from ~100 nm to ~5 nm to complement what is currently known regarding SI emission from samples of this size.

Other fundamental studies of free-standing nano-objects could focus on photon emission from nano-objects. Photon emission has been observed from various samples using monatomic and small cluster beams in the event-by-event mode. Recently, photon emission has also been observed in our lab from organic dyes and inorganic salts bombarded by Au_{400}^{4+}. Though the yield of photon emission is low from impacts with Au_{400}^{4+}, studies should focus on sample size effects that may result from incomplete projectile energy deposition into an object.

Furthermore, the use of photon emission from analyte surfaces could be utilized as a start signal for time of flight analysis, allowing for a new methodology for investigations in the positive ion mode. At present, the yield of detected photons from Au_{400}^{4+} impacts is too low for this scheme to be effective. At present, a high voltage system (100 kV platform) is being developed to deliver highly energetic Au-projectiles onto surfaces. These higher energy projectiles may produce enough photon emission for spectroscopic investigations of the emitted light to be conducted. Photon emission from all of the large and massive Au clusters (and from C_{60}^{+}) should be investigated.

Future work with solid-supported lipid bilayers could focus on the investigation of lipid rafts and other complex lipid phase segregation using imaging mass spectrometry. A localization system using the event-by-event bombardment/detection mode coupled to an electron emission microscope is under development in our lab. At present it is capable of producing ion-specific maps from μm-sized objects obtained via event-by-event bombardment/detection mode. Ideally, this instrument could provide a detailed chemical mapping of the cholesterol in lipid rafts at the nanometer scale. Localization mass spectrometry of the lipid rafts may provide validation of information obtained via correlation coefficients, while also offering the capability to visualize the distribution of the chemical species.

REFERENCES

(1) Benninghoven, A. *Angew. Chem. Intl. Ed.* **1994**, *33*, 1023-1043.

(2) Winograd, N. *Anal. Chem.* **2005**, *77*, 142a-149a.

(3) Li, Z.; Verkhoturov, S. V.; Schweikert, E. A. *Anal. Chem.* **2006**, *78*, 7410-7416.

(4) Rol, P. K.; Fluit, J. M.; Kistemaker, J. *Physica* **1960**, *26*, 1000-1008.

(5) Gronlund, F.; Moore, W. J. *J. Chem. Phys.* **1960**, *32*, 1540-1545.

(6) Andersen, H. H.; Bay, H. L. *J. of Appl. Phys.* **1974**, *45*, 953-954.

(7) Thompson, D. A.; Johar, S. S. *Appl.Phys. Lett.***1979**, *34*, 342-345.

(8) Johar, S. S.; Thompson, D. A. *Surf. Sci.* **1979**, *90*, 319-330.

(9) Wucher, A. *Appl. Surf. Sci.ence* **2006**, *252*, 6482-6489.

(10) Appelhans, A. D.; Delmore, J. E. *Anal. Chem.* **1989**, *61*, 1087-1093.

(11) Blain, M. G.; Dellanegra, S.; Joret, H.; Lebeyec, Y.; Schweikert, E. A. *Phys. Rev. Lett.ers* **1989**, *63*, 1625-1628.

(12) Benguerba, M.; Brunelle, A.; Dellanegra, S.; Depauw, J.; Joret, H.; Lebeyec, Y.; Blain, M. G.; Schweikert, E. A.; Benassayag, G.; Sudraud, P. *Nucl. Inst. Meth. Phys. Res. B* **1991**, *62*, 8-22.

(13) Baudin, K.; Brunelle, A.; Della-Negra, S.; Jacquet, D.; Håkansson, P.; Le Beyec, Y.; Pautrat, M.; Pinho, R. R.; Schoppmann, C. *Nucl. Inst. Meth. Phys. Res. B* **1996**, *112*, 59-63.

(14) Van Stipdonk, M. J.; Harris, R. D.; Schweikert, E. A. *Rapid Comm. in Mass Spectrom.* **1997**, *11*, 1794-1798.

(15) Van Stipdonk, M. J.; English, R. D.; Schweikert, E. A. *Anal. Chem.* **2000**, *72*, 2618-2626.

(16) Szymczak, W.; Wittmaack, K. *Nucl. Inst. Meth. Phys. Res. B* **1994**, *88*, 149-153.

(17) Wong, S. C. C.; Hill, R.; Blenkinsopp, P.; Lockyer, N. P.; Weibel, D. E.; Vickerman, J. C. *Appl. Surf. Sci.* **2003**, *203*, 219-222.

(18) Weibel, D.; Wong, S.; Lockyer, N.; Blenkinsopp, P.; Hill, R.; Vickerman, J. C. *Anal. Chem.* **2003**, *75*, 1754-1764.

(19) Zheng, L. L.; Wucher, A.; Winograd, N. *Anal. Chem.* **2008**, *80*, 7363-7371.

(20) Wucher, A.; Cheng, J.; Winograd, N. *Appl. Surf. Sci.* **2008**, *255*, 959-961.

(21) Wucher, A.; Sun, S.; Szakal, C.; Winograd, N. *Appl. Surf. Sci.***2004**, *231-2*, 68-71.

(22) Szakal, C.; Sun, S.; Wucher, A.; Winograd, N. *Appl. Surf. Sci.* **2004**, *231-2*, 183-185.

(23) Sun, S.; Szakal, C.; Roll, T.; Mazarov, P.; Wucher, A.; Winograd, N. *Surf. Int. Anal.* **2004**, *36*, 1367-1372.

(24) Sostarecz, A. G.; Sun, S.; Szakal, C.; Wucher, A.; Winograd, N. *Appl. Surf. Sci.* **2004**, *231-2*, 179-182.

(25) Tempez, A.; Schultz, J. A.; Della-Negra, S.; Depauw, J.; Jacquet, D.; Novikov, A.; Lebeyec, Y.; Pautrat, M.; Caroff, M.; Ugarov, M.; Bensaoula, H.; Gonin, M.; Fuhrer, K.; Woods, A. *Rapid Comm. in Mass Spectrom.* **2004**, *18*, 371-376.

(26) Bouneau, S.; Della-Negra, S.; Depauw, J.; Jacquet, D.; Le Beyec, Y.; Mouffron, J. P.; Novikov, A.; Pautrat, M. *Nucl. Inst. Meth. Phys. Res. B* **2004**, *225*, 579-589.

(27) Guillermier, C.; Negra, S. D.; Rickman, R. D.; Pinnick, V.; Schweikert, E. A. *Appl. Surf. Sci.* **2006**, *252*, 6529-6532.

(28) Mahoney, J. F.; Parilis, E. S.; Lee, T. D. *Nucl. Inst. Meth. Phys. Res. B* **1994**, *88*, 154-159.

(29) Mahoney, J. F.; Perel, J.; Lee, T. D.; Martino, P. A.; Williams, P. *J. Amer. Soc. Mass Spectrom.* **1992**, *3*, 311-317.

(30) Toyoda, N.; Matsuo, J.; Aoki, T.; Yamada, I.; Fenner, D. B. *Nucl. Inst. Meth. Phys. Res. B* **2002**, *190*, 860-864.

(31) Matsuo, J.; Okubo, C.; Seki, T.; Aoki, T.; Toyoda, N.; Yamada, I. *Nucl. Inst. Meth. Phys. Res. B* **2004**, *219-20*, 463-467.

(32) Knoll, G. F. *Radiation Detection and Measurement*, 2nd ed.; Wiley: New York, 1989.

(33) Park, M. A.; Gibson, K. A.; Quinones, K.; Schweikert, E. A. *Science* **1990**, *248*, 988-990.

(34) Schenkel, T.; Kraemer, A.; Leung, K.-N.; Hamza, A. V.; McDonald, J. W.; Schneider, D. H.; Kraemer, A. *Proc. of SPIE-The Intl. Soc. Optical Eng.* **2001**, *4468*, 35-46.

(35) Schenkel, T.; Wu, K. J. *Intl. J.Mass Spectrom.* **2003**, *229*, 47-53.

(36) Della-Negra, S.; Beyec, Y. L. *Anal. Chem.* **1985**, *57*, 2035-2040.

(37) Li, Z.; Verkhoturov, S. V.; Schweikert, E. A. *Anal. Chem.* **2006**.

(38) Van Stipdonk, M. J.; Schweikert, E. A.; Park, M. A. *J. Mass Spectrom.* **1997**, *32*, 1151-1161.

(39) Diehnelt, C. W.; English, R. D.; Van Stipdonk, M. J.; Schweikert, E. A. *Nucl. Inst. Meth. Phys. Res. B* **2002**, *193*, 883-890.

(40) Benguerba, M.; Brunelle, A.; Della-Negra, S.; Depauw, J.; Joret, H.; Le Beyec, Y.; Blain, M. G.; Schweikert, E. A.; Assayag, G. B.; Sudraud, P. *Nucl. Inst. Meth. Phys. Res. B* **1991**, *62*, 8-22.

(41) Verkhoturov, S. V.; Schweikert, E. A.; Rizkalla, N. M. *Langmuir* **2002**, *18*, 8836-8840.

(42) Zubarev, R. A.; Bitensky, I. S.; Demirev, P. A.; Sundqvist, B. U. R. *Nucl. Inst. Meth. Phys. Res. B* **1994**, *88*, 143-148.

(43) da Silveira, E. F.; Duarte, S. B.; Schweikert, E. A. *Surf. Sci.* **1998**, *408*, 28-42.

(44) Rickman, R. D.; Verkhoturov, S. V.; Parilis, E. S.; Schweikert, E. A. *Phys. Rev. Lett.* **2004**, *92*, 047601-1-4.

(45) Rickman, R. D.; Verkhoturov, S. V.; Hager, G. J.; Schweikert, E. A. *Intl. J. Mass Spectrom.* **2005**, *245*, 48-52.

(46) Ravanel, X.; Trouiller, C.; Juhel, M.; Wyon, C.; Kwakman, L. F. T.; Leonard, D. *Appl. Surf. Sci.* **2008**, *255*, 1415-1418.

(47) Zhu, Z. J.; Ghosh, P. S.; Miranda, O. R.; Vachet, R. W.; Rotello, V. M. *J. Am. Chem. Soc.* **2008**, *130*, 14139-14143.

(48) Zenobi, R. *Anal. Bioanal. Chem.* **2008**, *390*, 215-221.

(49) Nash, D. G.; Baer, T.; Johnston, M. V. *International Journal of Mass Spectrometry* **2006**, *258*, 2-12.

(50) Li, Z. Ph.D. Dissertation, Texas A&M University, College Station, Texas, 2007.

(51) Locklear, J. E. Ph.D. Dissertation, Texas A&M University, College Station, Texas, 2006.

(52) Hager, G. J. Ph.D. Dissertation, Texas A&M University, College Station, Texas, 2007.

(53) Rickman, R. D. Ph.D. Dissertation, Texas A&M University, College Station, Texas, 2004.

(54) Moore, J. H.; Davis, C. C.; Copan, M. A. *Building Scientific Apparatus: A Practical Guide to Design and Construction*, 2nd ed.; Perseus Books: Cambridge, MA, 1991.

(55) Cotter, R. J. *Time of Flight Mass Spectrometry, Instrumentation and Applications in Biological Research*; American Chemical Society: Washington D.C., 1997.

(56) Cox, B. D.; Park, M. A.; Kaercher, R. G.; Schweikert, E. A. *Anal. Chem.* **1992**, *64*, 843-847.

(57) Wiza, J. L. *Nucl. Inst. Meth. Phys. Res. B* **1979**, *162*, 587-601.

(58) Kaercher, R. G.; Dasilveira, E. F.; Blankenship, J. F.; Schweikert, E. A. *Nucl. Inst. Meth. Phys. Res. B* **1995**, *100*, 383-388.

(59) Kaercher, R. G.; Dasilveira, E. F.; Leite, C. V. B.; Schweikert, E. A. *Nucl. Inst. Meth. Phys. Res. B* **1994**, *94*, 207-217.

(60) Brunelle, A.; Laprevote, O. *Anal.Bioanal. Chem.* **2009**, *393*, 31-35.

(61) Goksu, E. I.; Vanegas, J. M.; Blanchette, C. D.; Lin, W. C.; Longo, M. L. *Biochim. Biophys. Acta-Biomembranes* **2009**, *1788*, 254-266.

(62) Jena, B. P. *Meth. in Nano Cell Biol.* **2008**, *90*, 157-182.

(63) Cho, W. J.; Jena, B. P.; Jeremic, A. M. *Meth. in Nano Cell Biol.* **2008**, *90*, 267-286.

(64) Kraft, M. L.; Weber, P. K.; Longo, M. L.; Hutcheon, I. D.; Boxer, S. G. *Science* **2006**, *313*, 1948-1951.

(65) Mingeot-Leclercq, M. P.; Deleu, M.; Brasseur, R.; Dufrene, Y. F. *Nature Prot.* **2008**, *3*, 1654-1659.

(66) Jones, E. A.; Lockyer, N. P.; Vickerman, J. C. *Intl. J. Mass Spectrom.* **2007**, *260*, 146-157.

(67) Ostrowski, S. G.; Van Bell, C. T.; Winograd, N.; Ewing, A. G. *Science* **2004**, *305*, 71-73.

(68) Wang, H. Y. J.; Post, S. N. J. J.; Woods, A. S. *Intl. J. Mass Spectrom.* **2008**, *278*, 143-149.

(69) Jackson, S. N.; Ugarov, M.; Egan, T.; Post, J. D.; Langlais, D.; Schultz, J. A.; Woods, A. S. *J.Mass Spectrom.* **2007**, *42*, 1093-1098.

(70) Jackson, S. N.; Wang, H. Y. J.; Woods, A. S. *Anal. Chem.***2005**, *77*, 4523-4527.

(71) McLean, J. A.; Ridenour, W. B.; Caprioli, R. M. *J. Mass Spectrom.* **2007**, *42*, 1099-1105.

(72) Puolitaival, S. M.; Burnum, K. E.; Cornett, D. S.; Caprioli, R. M. *J. Am. Soc. Mass Spectrom.* **2008**, *19*, 882-886.

(73) Monroe, E. B.; Jurchen, J. C.; Lee, J.; Rubakhin, S. S.; Sweedler, J. V. *J. Am. Chem. Soc.* **2005**, *127*, 12152-12153.

(74) Burnum, K. E.; Cornett, D. S.; Puolitaival, S. M.; Milne, S. B.; Myers, D. S.; Tranguch, S.; Brown, H. A.; Dey, S. K.; Caprioli, R. M. *J. Lipid Res.* **2009**, in press.

(75) Spengler, B.; Hubert, M. *J. Am. Soc. Mass Spectrom.* **2002**, *13*, 735-748.

(76) Luxembourg, S. L.; Mize, T. H.; McDonnell, L. A.; Heeren, R. M. *Anal. Chem.* **2004**, *76*, 5339-5344.

(77) Monroe, E. B.; Jurchen, J. C.; Koszczuk, B. A.; Losh, J. L.; Rubakhin, S. S.; Sweedler, J. V. *Anal. Chem.* **2006**, *78*, 6826-6832.

(78) Kraft, M. L.; Marxer, C. G.; Weber, P. K.; Hutcheon, I. D.; Boxer, S. G. *Biophys. J.* **2005**, *88*, 530a-530a.

(79) Lechene, C.; Hillion, F.; McMahon, G.; Benson, D.; Kleinfeld, A. M.; Kampf, J. P.; Distel, D.; Luyten, Y.; Bonventre, J.; Hentschel, D.; Park, K. M.; Ito, S.; Schwartz, M.; Benichou, G.; Slodzian, G. *J. Biol.* **2006**, *5*, 20.

(80) Lechene, C. P.; Luyten, Y.; McMahon, G.; Distel, D. L. *Science* **2007**, *317*, 1563-1566.

(81) Zheng, L.; McQuaw, C. M.; Ewing, A. G.; Winograd, N. *J. Am. Chem. Soc.* **2007**, *129*, 15730-15731.

(82) Touboul, D.; Kollmer, F.; Niehuis, E.; Brunelle, A.; Laprevote, O. *J. Am. Soc. Mass Spectrom.* **2005**, *16*, 1608-1618.

(83) Piehowski, P. D.; Carado, A. J.; Kurczy, M. E.; Ostrowski, S. G.; Heien, M. L.; Winograd, N.; Ewing, A. G. *Anal. Chem.* **2008**, *80*, 8662-8667.

(84) Baker, M. J.; Zheng, L.; Winograd, N.; Lockyer, N. P.; Vickerman, J. C. *Langmuir* **2008**, *24*, 11803-11810.

(85) Chan, Y. H. M.; Boxer, S. G. *Curr. Opin. Chem. Biol.* **2007**, *11*, 581-587.

(86) Groves, J. T.; Ulman, N.; Boxer, S. G. *Science* **1997**, *275*, 651-653.

(87) Kunze, A.; Sjovall, P.; Kasemo, B.; Svedhem, S. *J. Am. Chem. Soc.* **2009**, *131*, 2450-2451.

(88) Michel, R.; Subramaniam, V.; McArthur, S. L.; Bondurant, B.; D'Ambruoso, G. D.; Hall, H. K.; Brown, M. F.; Ross, E. E.; Saavedra, S. S.; Castner, D. G. *Langmuir* **2008**, *24*, 4901-4906.

(89) Prinz, C.; Hook, F.; Malm, J.; Sjovall, P. *Langmuir* **2007**, *23*, 8035-8041.

(90) Sherrod, S. D.; Diaz, A. J.; Russell, W. K.; Cremer, P. S.; Russell, D. H. *Anal. Chem.* **2008**, *80*, 6796-6799.

(91) Daniel, S.; Albertorio, F.; Cremer, P. S. *MRS Bull.* **2006**, *31*, 536-540.

(92) Albertorio, F.; Diaz, A. J.; Yang, T. L.; Chapa, V. A.; Kataoka, S.; Castellana, E. T.; Cremer, P. S. *Langmuir* **2005**, *21*, 7476-7482.

(93) Yang, T. L.; Jung, S. Y.; Mao, H. B.; Cremer, P. S. *Anal. Chem.* **2001**, *73*, 165-169.

(94) Barenholz, Y.; Gibbes, D.; Litman, B. J.; Goll, J.; Thompson, T. E.; Carlson, F. D. *Biochem.***1977**, *16*, 2806-2810.

(95) Boxer, S. G. *Curr. Opin. Chem.Biol.* **2000**, *4*, 704-709.

(96) Diaz, A. J.; Albertorio, F.; Daniel, S.; Cremer, P. S. *Langmuir* **2008**, *24*, 6820-6826.

(97) Currie, L. A. *Anal. Chem.* **1968**, *40*, 586-593.

(98) Pacholski, M. L.; Cannon, D. M.; Ewing, A. G.; Winograd, N. *J. Am. Chem. Soc.* **1999**, *121*, 4716-4717.

(99) Pike, L. J. *J. Lipid Res.* **2009**, *50*, S323-S328.

(100) VanStipdonk, M. J.; Schweikert, E. A.; Park, M. A. *J. Mass Spectrom.* **1997**, *32*, 1151-1161.

(101) McDonnell, L. A.; Heeren, R. M. *Mass Spectrom. Rev.* **2007**, *26*, 606-643.

(102) Mahoney, C. M.; Fahey, A. J.; Belu, A. M. *Anal. Chem.* **2008**, *80*, 624-632.

(103) Gillen, G.; Fahey, A.; Wagner, M.; Mahoney, C. *Appl.Surf. Sci.* **2006**, *252*, 6537-6541.

(104) Hoppe, P. *Appl. Surf. Sci.* **2006**, *252*, 7102-7106.

(105) Rajagopalachary, S.; Verkhoturov, S. V.; Schweikert, E. A. *Nano. Lett.* **2008**, *8*, 1076-1080.

(106) Kim, Y. P.; Oh, E.; Hong, M. Y.; Lee, D.; Han, M. K.; Shon, H. K.; Moon, D. W.; Kim, H. S.; Lee, T. G. *Anal. Chem.* **2006**, *78*, 1913-1920.

(107) Konarski, P.; Iwanejko, I.; Mierzejewska, A. *Appl. Surf. Sci.* **2003**, *203*, 757-761.

(108) Marcus, A.; Winograd, N. *Anal. Chem.* **2006**, *78*, 141-148.

(109) Fletcher, J. S.; Henderson, A.; Jarvis, R. M.; Lockyer, N. P.; Vickerman, J. C.; Goodacre, R. *Appl. Surf. Sci.* **2006**, *252*(19), 6869-6874.

(110) Delcorte, A.; Garrison, B. J. *J. Phys. Chem. C* **2007**, *111*, 15312-15324.

(111) Li, Z.; Verkhoturov, S. V.; Locklear, J. E.; Schweikert, E. A. *Intl. J. Mass Spectrom.* **2008**, *269*, 112-117.

(112) Ziegler, J. In *Stopping and Range of Ions in Matter (SRIM)*, 2008.

(113) Della-Negra, S.; Pinnick, V., Ed.; *Institut de Physique Nucleaire*: Orsay, France, 2008.

(114) Farizon, B.; Farizon, M.; Gaillard, M. J.; Genre, R.; Louc, S.; Martin, J.; Buchet, J. P.; Carre, M.; Senn, G.; Scheier, P.; Mark, T. D. *Intl. J. Mass Spectrom.* **1997**, *164*, 225-230.

(115) Rohmund, F.; Campbell, E. E.; Knospe, O.; Seifert, G.; Schmidt, R. *Phys. Rev. Lett.* **1996**, *76*, 3289-3292.

(116) Reinkoster, A.; Siegmann, B.; Werner, U.; Huber, B. A.; Lutz, H. O. *J. Phys. B.* **2002**, *35*, 4989-4997.

(117) Tepper, F.; Kaledin, L. *BioProcess Intl.* **2006**, *4*, 64-68.

(118) Desai, S. R.; Wu, H. B.; Wang, L. S. *Intl. J.Mass Spectrom.* **1996**, *159*, 75-80.

(119) Guinan, M. *J. Nucl. Mat.* **1974**, *53*, 171-178.

(120) Shulga, V. V.; Vicanek, M.; Sigmund, P. *Phys Rev A* **1989**, *39*, 3360-3372.

(121) Guillermier, C.; Della-Negra, S.; Schweikert, E. A.; Dunlop, A.; Rizza, G. *Intl. J. Mass Spectrom.* **2008**, *275*, 86-90.

(122) Verdier, S.; Metson, J. B.; Dunlop, H. M. *J. Mass Spectrom.* **2007**, *42*, 11-19.

(123) Gianotto, A. K.; Rawlinson, J. W.; Cossel, K. C.; Olson, J. E.; Appelhans, A. D.; Groenewold, G. S. *J. Am. Chem. Soc.* **2004**, *126*, 8275-8283.

(124) Groenewold, G. S.; Kessinger, G. F.; Scott, J. R.; Gianotto, A. K.; Appelhans, A. D.; Delmore, J. E. *Anal. Chem.* **2001**, *73*, 226-232.

(125) Plog, C.; Wiedmann, L.; Benninghoven, A. *Surf. Sci.* **1977**, *67*, 565-580.

(126) Liu, Z. Y.; Wang, C. R.; Huang, R. B.; Zheng, L. S. *Intl. J. Mass Spectrom.* **1995**, *141*, 201-208.

(127) Veryovkin, I. V.; Calaway, W. F.; Tripa, C. E.; Pellin, M. J. *Nucl. Inst. Meth. Phys. Res. B* **2007**, *261*, 508-511.

(128) Hinz, K. P.; Spengler, B. *J. Mass Spectrom.* **2007**, *42*, 843-860.

(129) Samek, O.; Kurowski, A.; Kittel, S.; Kukhlevsky, S.; Hergenroder, R. *Spectrochim. Acta B* **2005**, *60*, 1225-1229.

(130) Pinnick, V.; Rajagopalachary, S.; Verkhoturov, S. V.; Kaledin, L.; Schweikert, E.A. *Anal. Chem.* **2008**, *80*, 9052-9057.

(131) Tepper, F.; Kaledin, L.; Kaledin, T. *J. Liq. Chrom.* **2009**, *32*, 607-627.

(132) Gitzen, W. H. *Alumina as a Ceramic Material*; The American Ceramic Society: Westerville, OH, 1970.

(133) Anders, C.; Kirihata, H.; Yamaguchi, Y.; Urbassek, H. M. *Nucl. Inst. Meth. Phys. Res. B* **2007**, *255*, 247-252.

(134) Garrison, B. J.; Postawa, Z. *Mass Spectrom. Rev.* **2008**, *27*, 289-315.

(135) Zadgoankar, U.; Patent, I., Ed. A Catalyst Composition for Catalytic Cracking of Waste Plastic, 2005; Vol. 094990A1.

(136) Raiagopalachary, S.; Verkhoturov, S. V.; Schweikert, E. A. *Anal. Chem.***2009**, *81*, 1089-1094.

(137) Jeng, E. S.; Moll, A. E.; Roy, A. C.; Gastala, J. B.; Strano, M. S. *Nano. Lett.* **2006**, *6*, 371-375.

(138) Mirmomtaz, E.; Castronovo, M.; Grunwald, C.; Bano, F.; Scaini, D.; Ensafi, A. A.; Scoles, G.; Casalis, L. *Nano. Lett.* **2008**, *8*, 4134-4139.

(139) Novikov, A.; Caroff, M.; Della-Negra, S.; Depauw, J.; Fallavier, M.; Le Beyec, Y.; Pautrat, M.; Schultz, J. A.; Tempez, A.; Woods, A. S. *Rapid Comm. Mass Spectrom.* **2005**, *19*, 1851-1857.

APPENDIX A

LIQUID METAL ION SOURCE FABRICATION

A Procedure Modified from R. Rickman's Dissertation

Read through this entire procedure before attempting to fabricate this source.

Etching Solution Preparation:

1. Clean all glassware to be used in preparation thoroughly. If the glassware is not clean, the etching solution will be yellow in color (the solution will be less efficient for etching).
2. Prepare an aqueous solution of 35% w/w NaOH in a plastic bottle. Write the date prepared on the container (NaOH should be made fresh every 3 months).
3. Mix in a clean and dry beaker:

   -10mL of 35% NaOH solution

   -50mL of Glycerol

   -50mL of distilled water

   Stir thoroughly. Prepare the etching solution fresh on the same day as the source preparation. Etching solution rapidly loses etching efficiency as it ages.

Needle Preparation:

1. Cut a section of tungsten wire (0.200 mm dia.) 5-10 cm long. Clean with automotive grade sandpaper (600-grit). This mechanical removal of the

oxide layer needs to be done the same day as assembling and dipping the source, so do not prepare needles in bulk and store.

2. Place wire in pin vise (see Fig. A1a) and center. Pull the wire with your fingers from the base of the pin vise all the way to the end of the wire in continuous smooth motions (Fig. A1b). Repeat until the wire is straight.
3. Cut the wire to a length of 3 cm.
4. Etch the needle using the following procedures:
    a. Place the needle pin vise into the Teflon needle brace (Fig. A2a), and place the needle brace into the Teflon block (Fig A2b).
    b. Be sure the level of the etching solution is parallel to the base of the platform and perfectly normal to the needle. Use the course adjustment on the platform to bring the solution to the needle. Use the fine adjustment (x-y positioner) on the stand to make the final positional adjustments.
    c. The end of the wire can be split or ragged as a result of cutting. This portion must be removed before etching the needle. Attach the electrical connections as shown in Figure A3. Insert about 1mm of the needle into the etching solution and turn on the AC voltage to a high setting (~40 V). Remove the needle from the solution every ~2min to check the progress of the etching. Continue until the needle is flat on the bottom. At times, this step can result in a needle being formed—if this happens, skip step 4d.

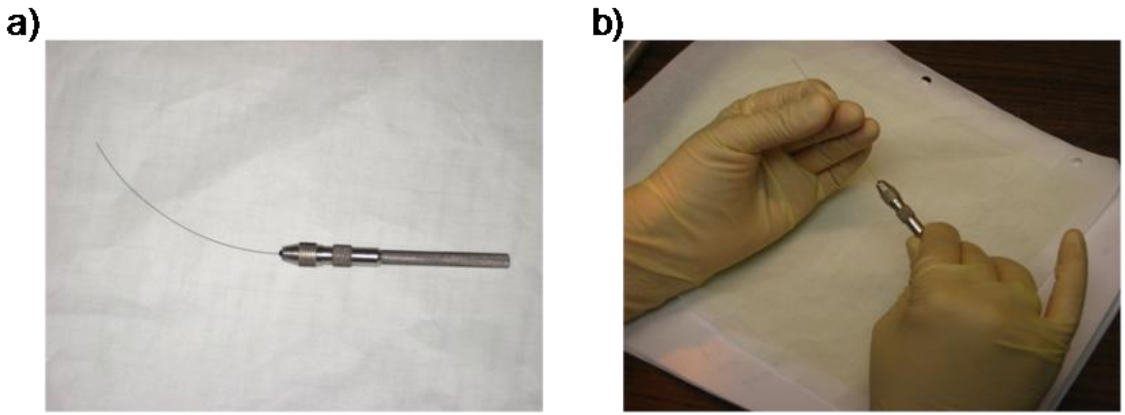

Figure A1. Needle preparation.

a)

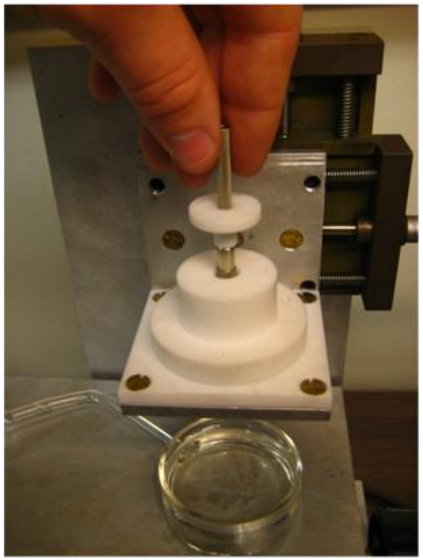

b)

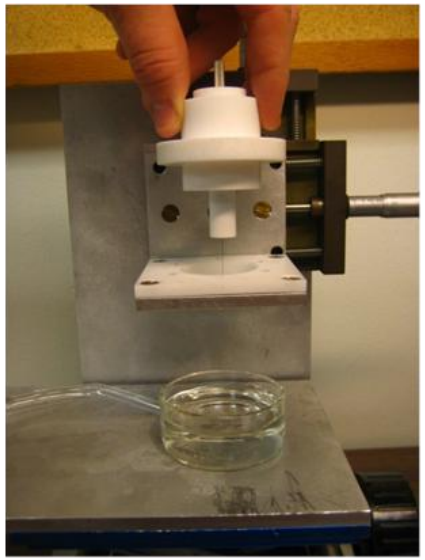

Figure A2. Inserting the needle into the etching assembly.

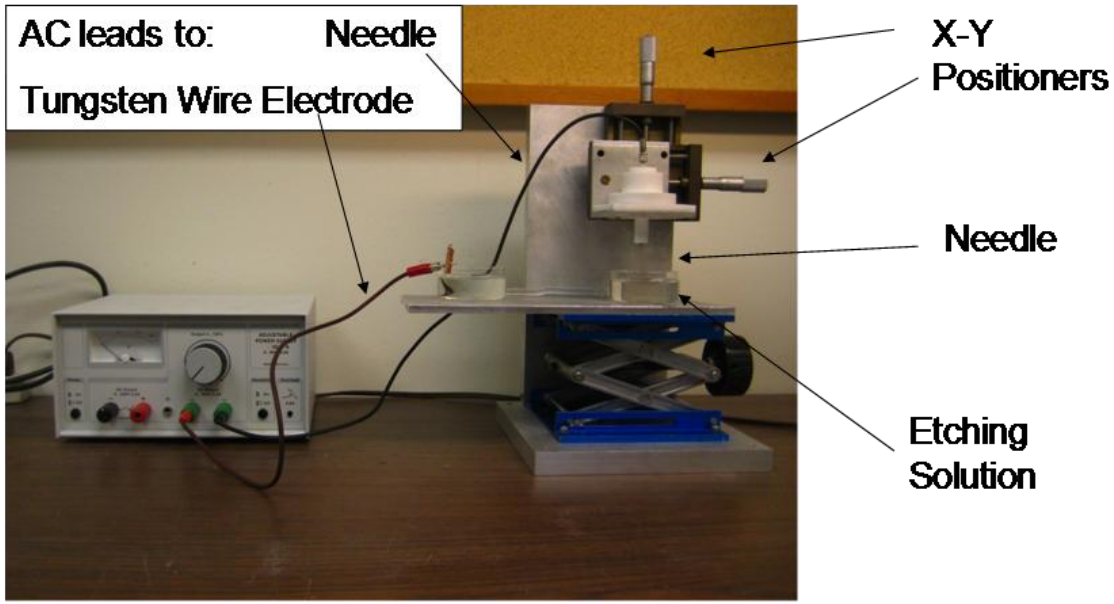

Figure A3. Attaching the electrical connections to the needle.

d. With the voltage off, immerse the needle tip into the etching solution and use the fine adjustment to pull the needle out just enough to maintain the meniscus (Fig A4a). Use the fine adjustment on the positioner to ensure that the length of the needle tip submerged is enough to form the proper half-angle. This should be done while looking through the microscope for better accuracy. Apply a low voltage (~5-10 V) to form the cone at the tip of the needle. Remove the needle from the solution every ~5min to check the progress of the etching. Continue until the needle cone has a half angle of ~ 49.5°. The tolerance for cone angle is between 90-100° (Fig A4b-c).
e. After the cone has formed, turn AC voltage off and immerse the needle 15mm into the solution. Increase the voltage until very fine bubbles form on the surface of the needle and rise to the surface of the etching solution ~5-10 V (Serge says like a good champagne!). Remove the oxide layer by etching for ~ 6 min.
f. Rinse the needle with distilled water to remove excess etching solution. Use the needle on the same day as preparation—do not store.

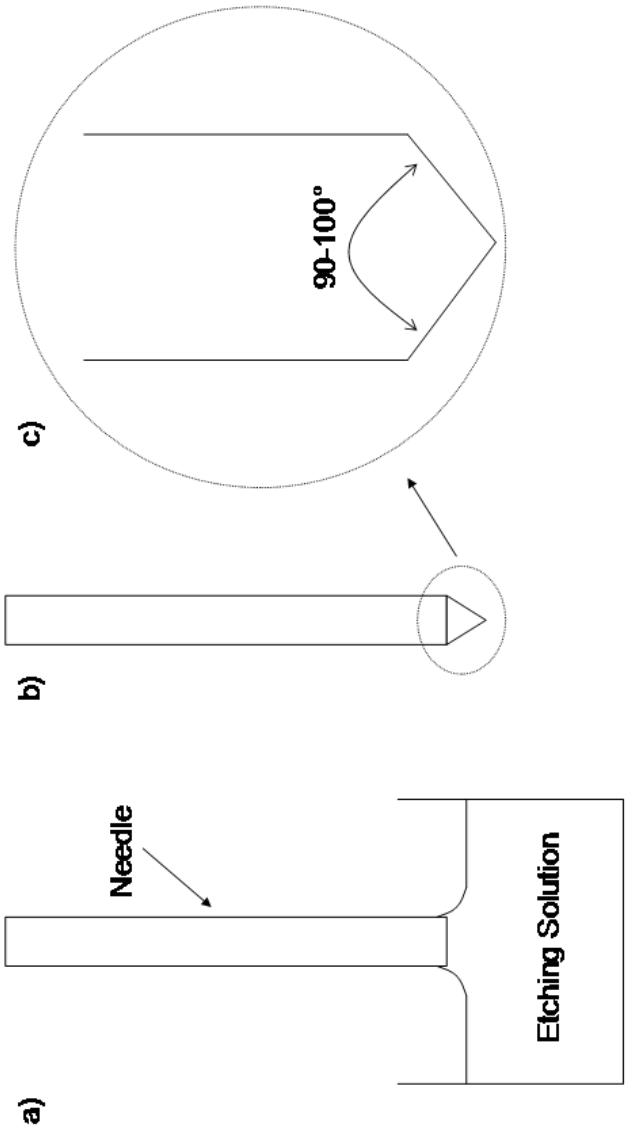

Figure A4. Etching the needle.

Spring Reservoir Preparation:

1. Cut a ~20 cm piece of tungsten wire (0.200 mm dia.). Clean with automotive grade sandpaper. Bend wire in various directions with your hand while cleaning to 'break' the memory of the wire. Reservoirs should be made on the day of source production so the mechanical removal of oxide layers using sandpaper is not lost.
2. Clean wire form with ethanol to ensure no contamination of the wire. Place center of wire on form (Fig A5) and begin to wrap around the form with jerky motions toward previous turn. Be sure to use equal force at top and bottoms of turns.
3. Make 9-10 tight turns to form the spring reservoir (no less than 9). There should be little to no space between the individual turns. If equal force was used in production, a good reservoir should be a barrel, parallel with the base.
4. Cut spring ends to the proper length using the spring jig as a measuring tool (see Fig A6). Do not bend or crease the legs, they should be straight or just gently curved. Insert the spring legs into the source assembly and tighten screws gently. Do not over-tighten as that can cause undue stress on the spring—use tweezers to hold the spring legs to keep them from twisting. If the spring is not parallel to the base (i.e. not horizontal) use the spring form to bring it into position.
5. Remove Teflon block from etching stand (Fig A7a) and attach the trident to split the electrical connections for etching the reservoir (see Fig A7b). Turn spring assembly 90° so that it is perpendicular to the outlet of the tube connecting the

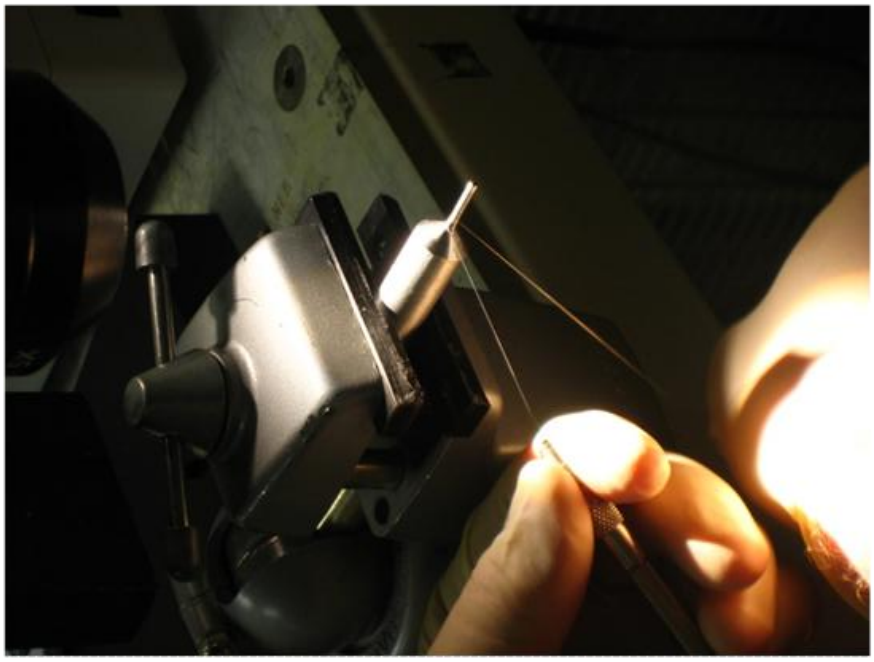

Figure A5. Creating the reservoir.

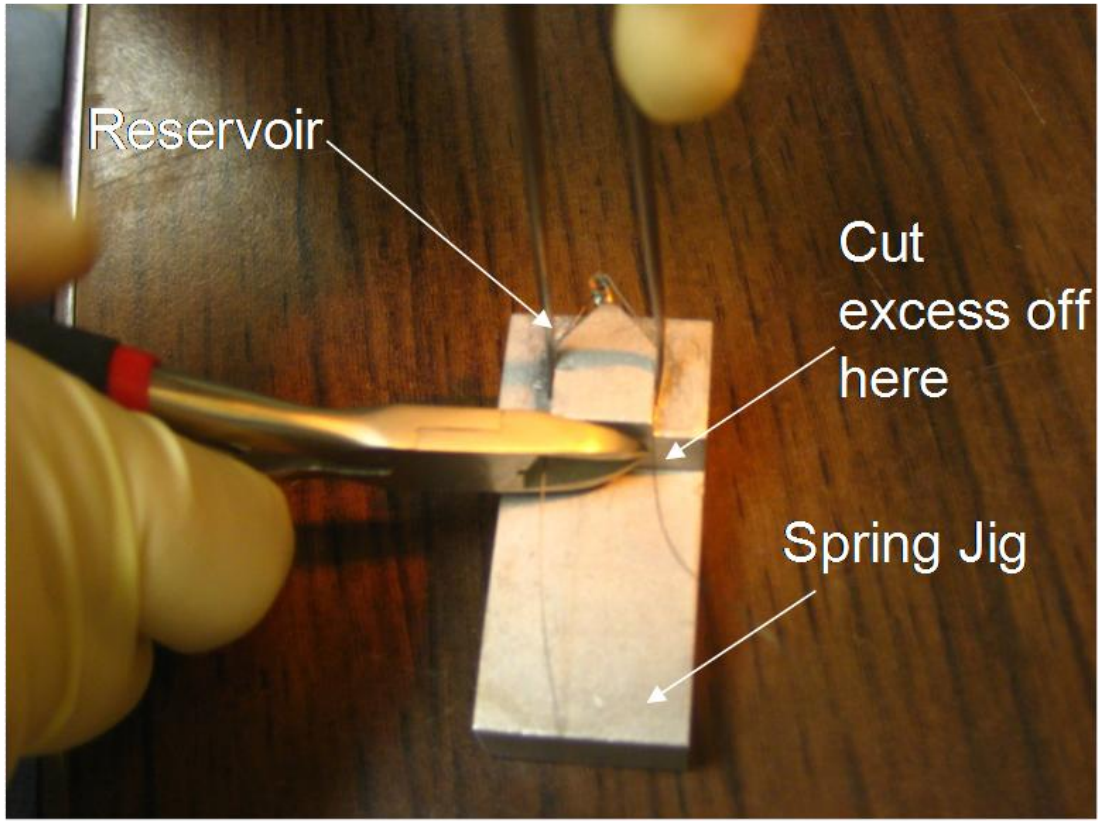

Figure A6. Measuring and cutting the legs of the reservoir.

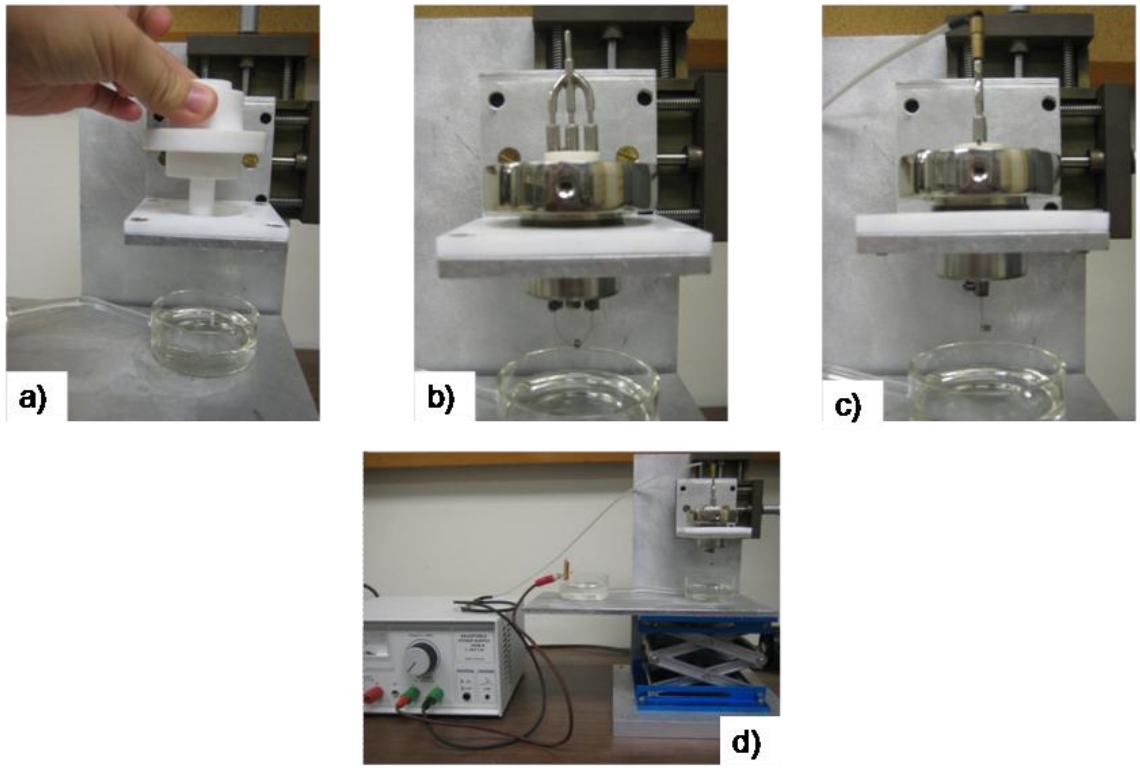

Figure A7. Inserting the reservoir into the etching assembly.

two glass chambers (and thus the electrical field (see Fig A7c)). Immerse spring into the etching solution and be sure to remove any air bubble caught in center of spring. Attach the electrical connections as shown in Fig A7d. Apply the same low voltage (~5-10 V) to achieve small, rising bubbles and etch for 5 min. Remove any air bubbles that form in the center of spring during etching. Rinse spring with distilled water to remove excess etching solution.

Inserting Needle into Spring Assembly:

1. Accurately measure 20 mm from the tip of the needle and cut off excess.
2. Insert needle into the source assembly and using tweezers position into the middle of the spring reservoir (between spring turn 4 and 5).
3. The reservoir should be centered in the side view of the spring, and must be in a vertical position above the spring at a right angle to the top of the spring. Use millimeter paper to adjust the height of the needle to 1.3 mm above the top of the spring (see Fig A8). In the case that sparking occurs with sources, adjust the needle height above the reservoir to ~1.7 mm (do not exceed 2 mm or source will not emit). 1.3-1.5 mm is ideal for large Au cluster emission.
4. Tighten the screw of the needle holder gently. Do not cause tension that forces the needle to one side or the other. If this occurs, the needle can move during heating.
5. Dip the entire assembly into etching solution, attach the trident and apply the same low voltage (~5-10V) to achieve small, rising bubbles and etch for 5

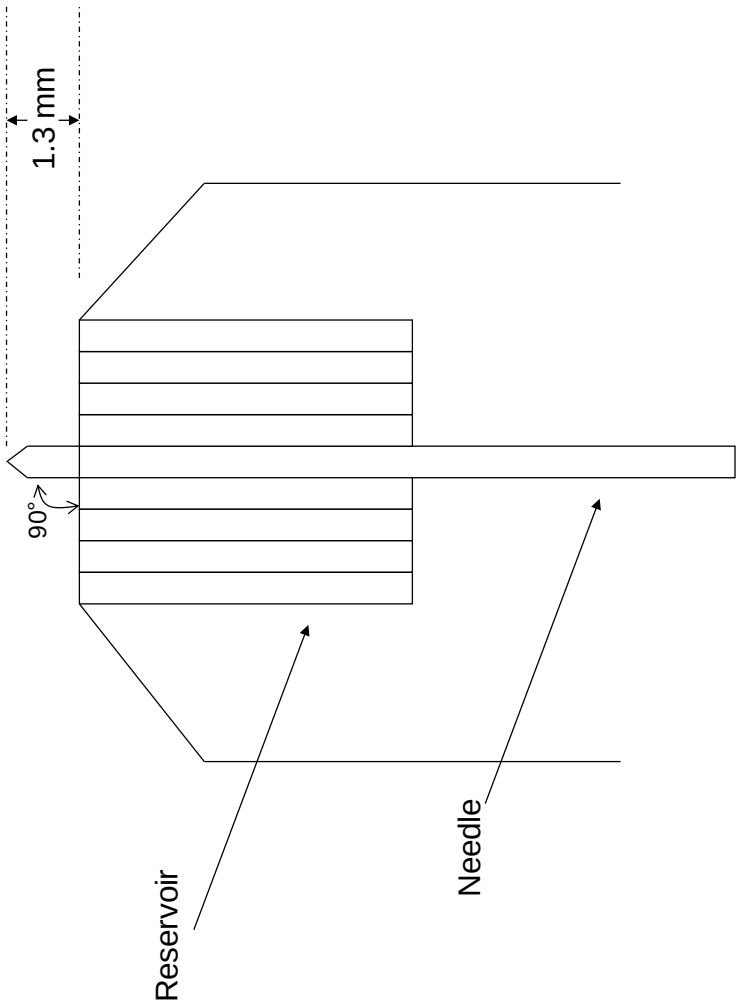

Figure A8. Inserting the needle into the reservoir.

minutes. Be sure to remove any air bubbles that form in the center of the reservoir. The time of etching is not critical, the color and finish is what is important. When all of the oxide layer has been removed, the color of the tungsten after rinsing with water should be dark grey and matte (not shiny) in finish.

Inserting Source Assembly into Vacuum:

1. Attach the source assembly to the vertical translator and attach wires to feed-through (see Fig A9). Cover the insulator with a thin Teflon cover to protect it from tungsten evaporation. Be sure to check connectivity before pumping.
2. Obtain a pellet of the Au/Si eutectic (97% Au / 3% Si, Academy Precision Metals). Clean it by using a file to remove surface contaminants, use 600-grit followed by 1000-grit automotive sandpaper to smooth surface, finally use green abrasive pad to polish. Sonicate in ethanol for 5 min then dry with nitrogen. Place the pellet in the tantalum boat in the vacuum chamber. Fresh pellet dimensions are a cylinder of 3/8" height, ~17g. When the mass of the pellet is ≤ 11g, another piece of gold should be added.
3. Clean the chamber and boat with ethanol and place source assembly lid onto vacuum chamber. Evacuate to at least $3x10^{-6}$ Torr.
4. Heat the eutectic by ramping the temperature of the tantalum boat (monitored with the thermocouple) at a rate of 10°C/min. For the varian power supply, this generally equates to 1 increment/min. The eutectic will melt at a

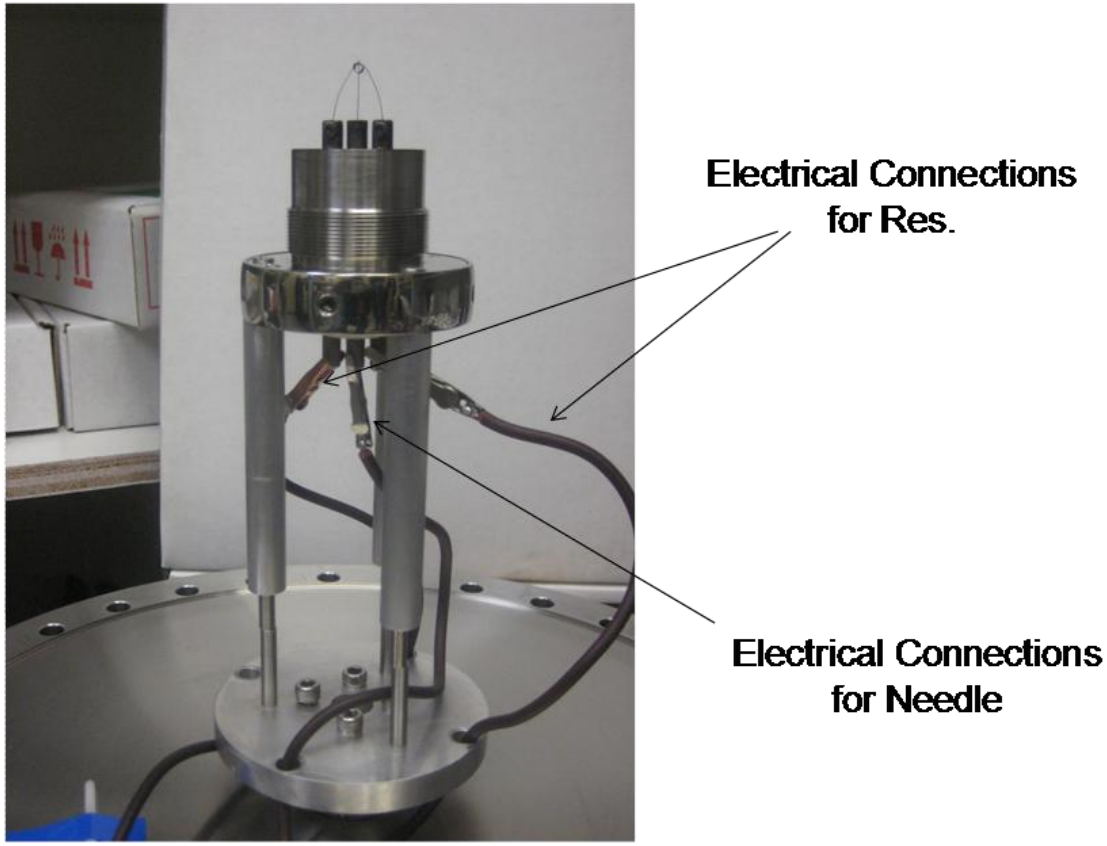

Figure A9. Inserting the source into the dipping assembly.

temperature of ~363°C. This constitutes ~395 mV across the tantalum boat. The color of the eutectic will change from yellow to grey just before melting. Check by gently nudging the chamber—you will see ripples in the eutectic if it has melted; maintain the minimum temperature for complete liquidity.

5. The needle and spring must be free of any contaminants before immersing into the eutectic. To do this:
    a. Apply ~7-8 W between the needle and one leg of the spring for ~ 2min (Fig A10a). 7-8 W should produce a red-orange color on the filament, avoid yellow or white—this means the filament is too hot. Check the location of the needle before, during, and after heating to assure the needle does not move when the reservoir springs expand (~10%).
    b. Apply the same power to the needle and the other leg of the spring for ~2 min (Fig A10b).
    c. Apply ~5 W of power between the two spring legs (not the needle) (Fig A10c). The spring will glow a light red color. Lower the needle and spring assembly slowly into the eutectic until the top of the spring is immersed completely. Turn off the power and begin to raise slowly but at a constant rate (do not use jerky motions).
    d. At times the reservoir will not fill the first time, but it should now be "wetted" enough to fill the subsequent times. If the spring is not filled on the first attempt, repeat steps 5a-c, dipping the reservoir

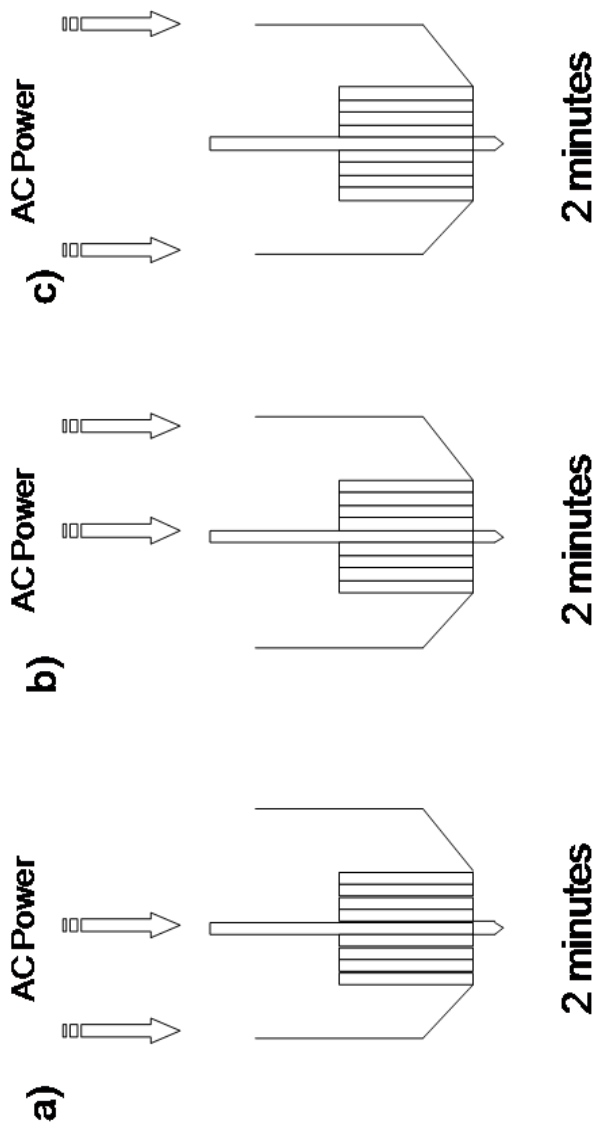

Figure A10. Heating assembly to remove contamination.

completely after each step. This makes a total of 4 dippings. Continue dipping until reservoir is filled.

6. Before breaking vacuum, examine the needle and reservoir with the microscope. A meniscus should be present between the needle and top of the reservoir (Fig A11). The reservoir should be filled with eutectic.
7. Cool the eutectic in the tantalum boat by directly turning the voltage on the boat to zero directly. Wait until the eutectic reaches room temperature before breaking vacuum and removing the source assembly.
8. It is helpful to take a picture of each source and write down its dimensions, and any other parameters of interest into the source notebook, in order to track any abnormalities in emission and lifetime.

Inserting Gold Source Assembly into System 7:

1. Attach the first extractor and center the needle in the center of the hole using the 4 set screws located at the base. Rotate the extractor and bring the tip of the needle in the plane of the bottom of the extractor cap (see fig. A12), using the microscope to view. Tighten in place with the locking washer.
2. Attach brass collar and brass lockring (see Fig A13). Attach the second extractor shield and use the microscope to make the final adjustments to the x-y position of the needle. The needle should be centered within the two diaphragms. Tighten the set screws of the extractor.
3. Install the source onto the assembly flange and connect the high voltage cables to the filament (x2) and the floating voltage cable to the base of the

source. Check for proper connectivity before attaching set-up to the instrument.

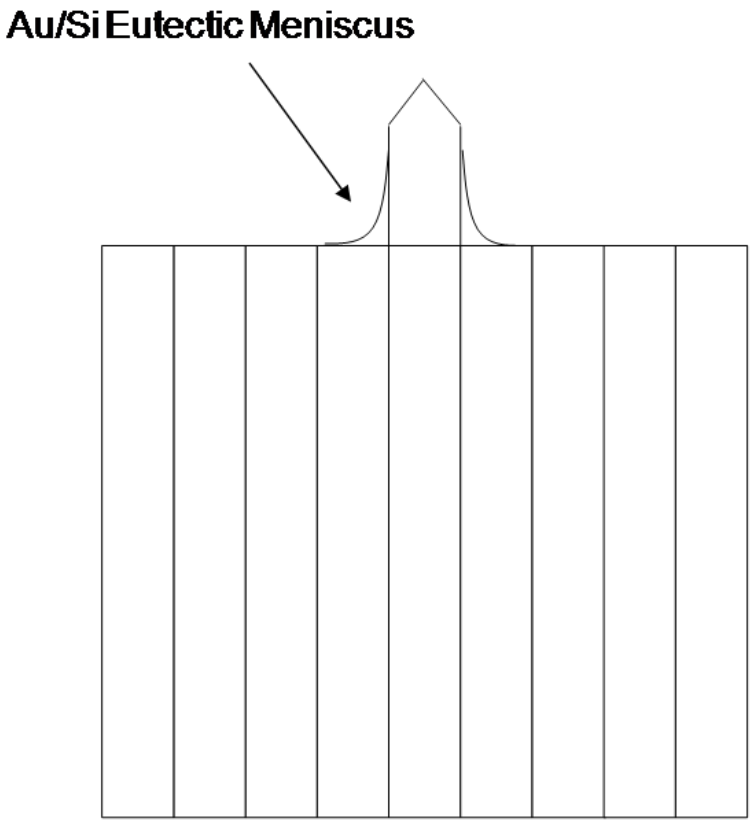

Figure A11. Meniscus formed on a good source after dipping.

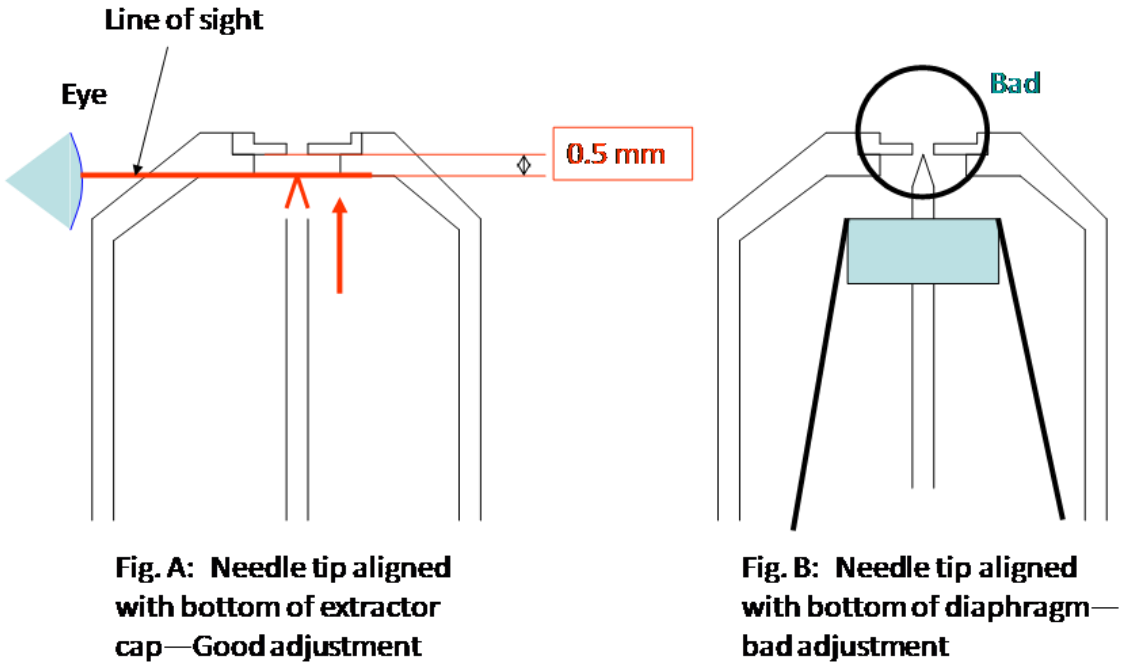

Figure A12. Needle height adjustment in extractor cap.

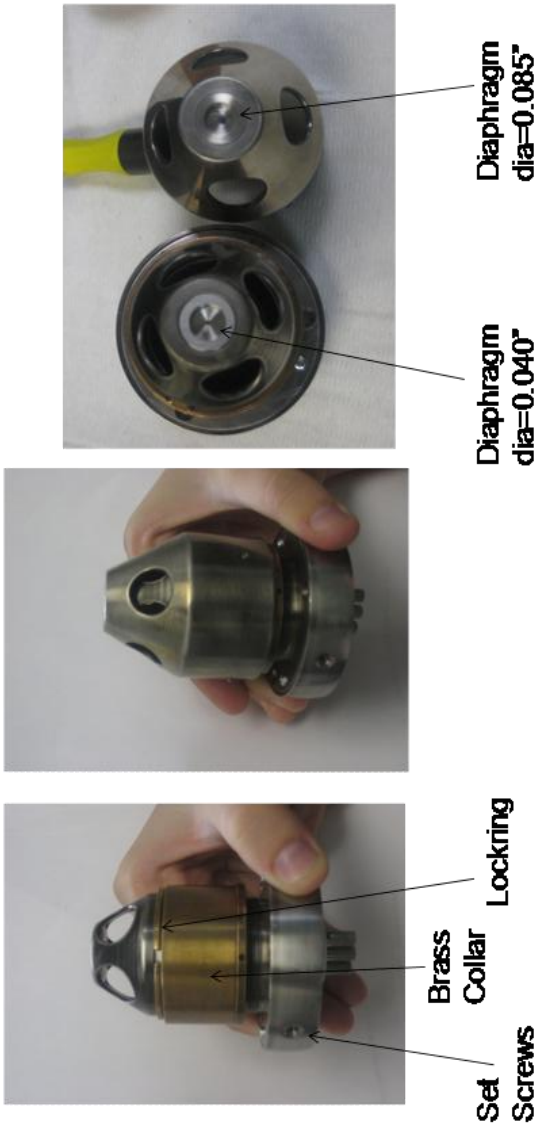

Figure A13. Completing the source assembly with final adjustments of extractor cap.

APPENDIX B

SYSTEM V AND VII DRAWINGS

1. Sample Cube without Wafer
2. Sample Cube for Wafers
3. Sample Introduction Rod
4. System 7 Extraction Grid
5. Au-LMIS First Extractor Cap Diaphragm
6. 8-Anode Detector (Machined Part)
7. 8-Anode Detector (Total Part)

note This anode was designed by J. DeBord in April 2009, and is the new design for all 8-anode systems. This design, however, was not used in the data obtained for this dissertation. At the time, the designs of J.E. Locklear (C_{60} instrument) and G.J. Hager (Au instrument) were in place. See their dissertations for active area, dead space, and dimensional calculations.

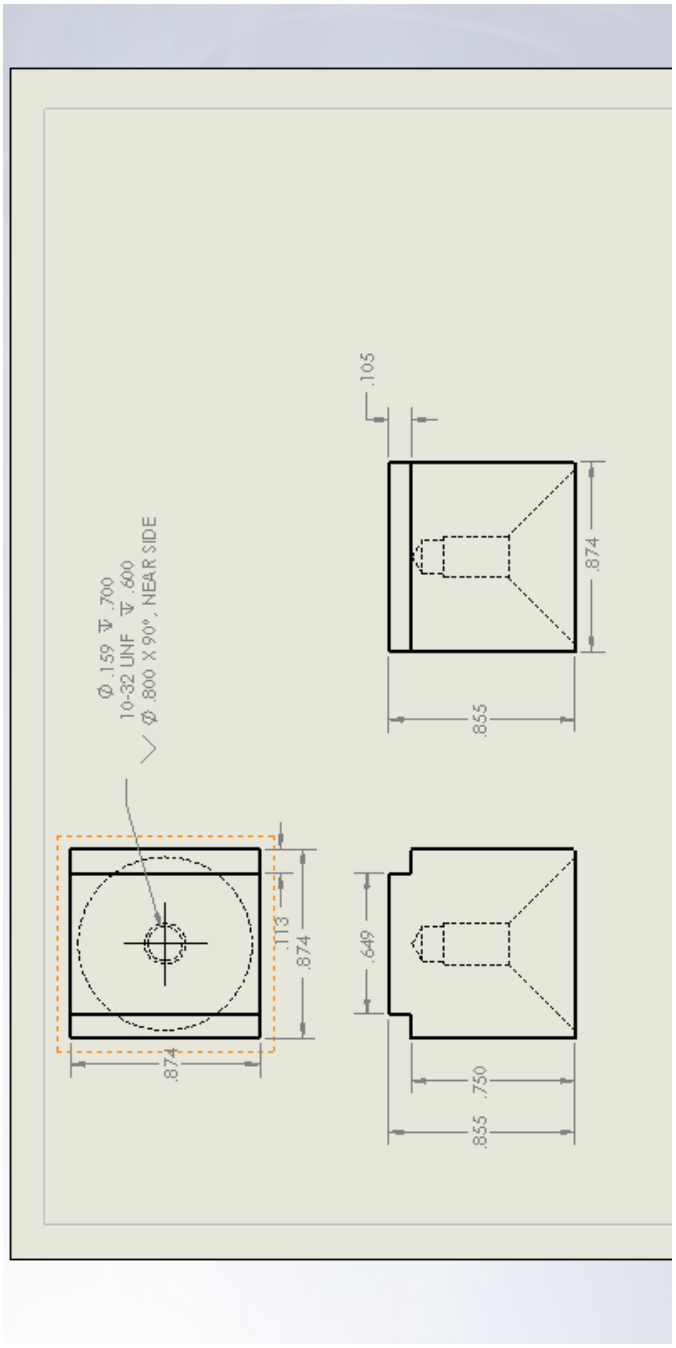

Figure B1. Sample cube without silicon wafer. Cubes may be prepared from brass or stainless steel.

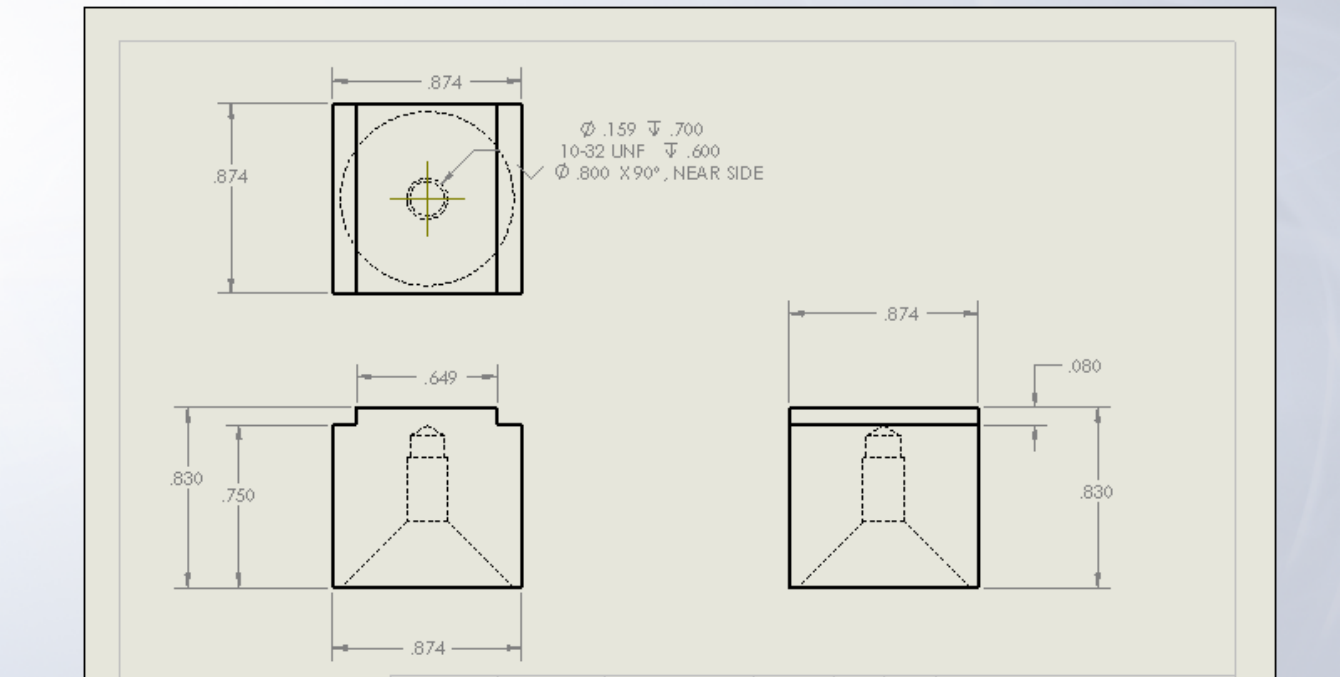

Figure B2. Sample cube for use with silicon wafer or other thick samples. Cubes may be prepared from brass or stainless steel.

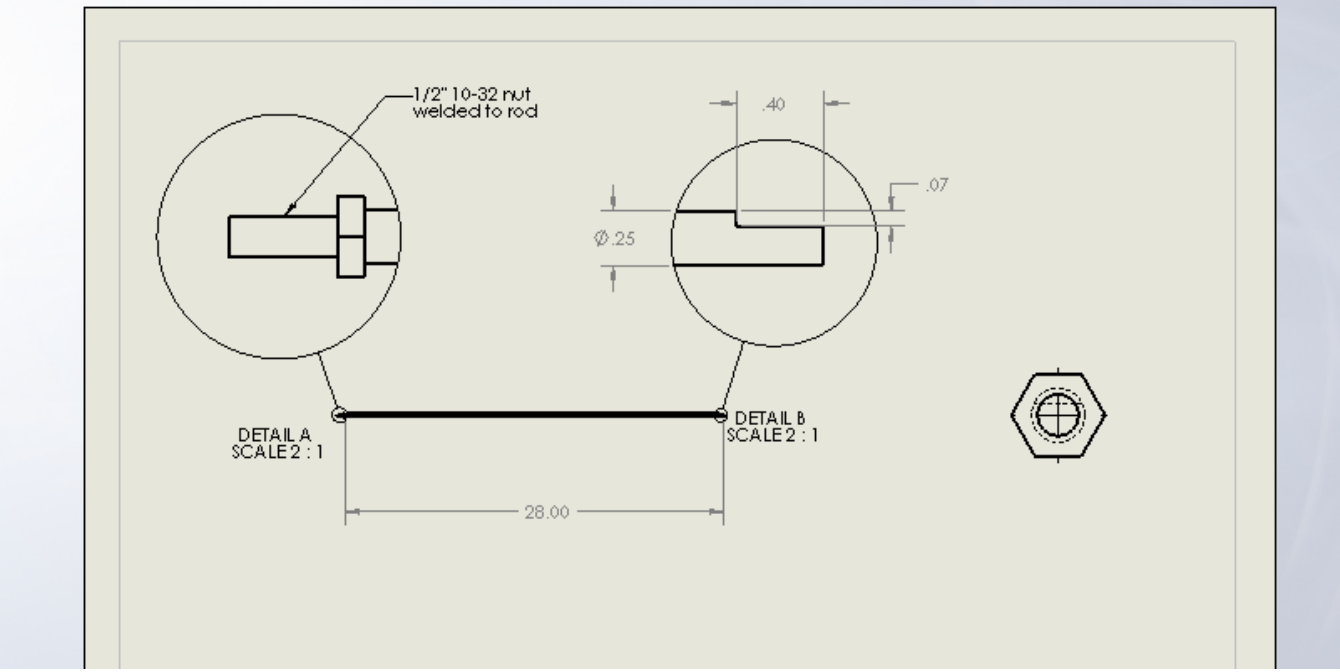

Figure B3. Sample introduction rod. Length of rod may vary depending on which system it will be used with. This rod is for the LMIS instrument.

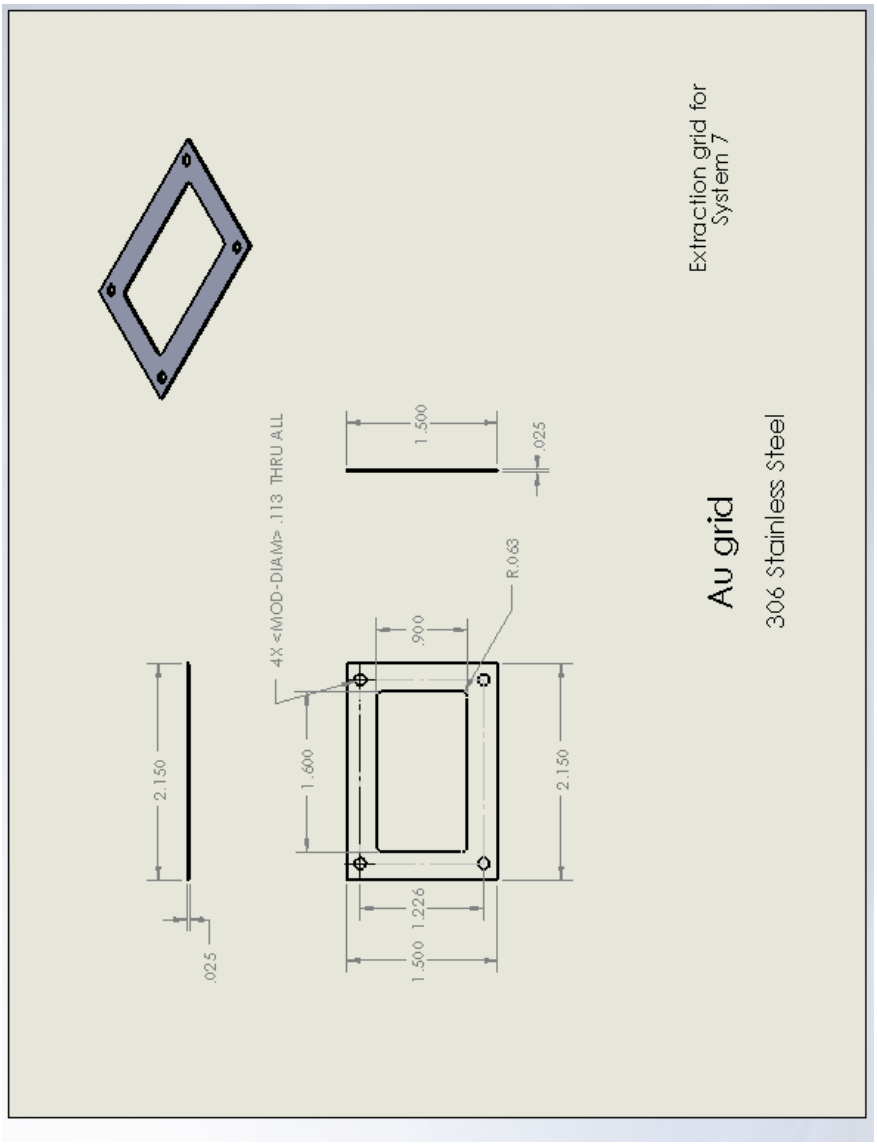

Figure B4. LMIS instrument extraction grid. This should be made from stainless steel. The dimensions of this grid apply only to system VII.

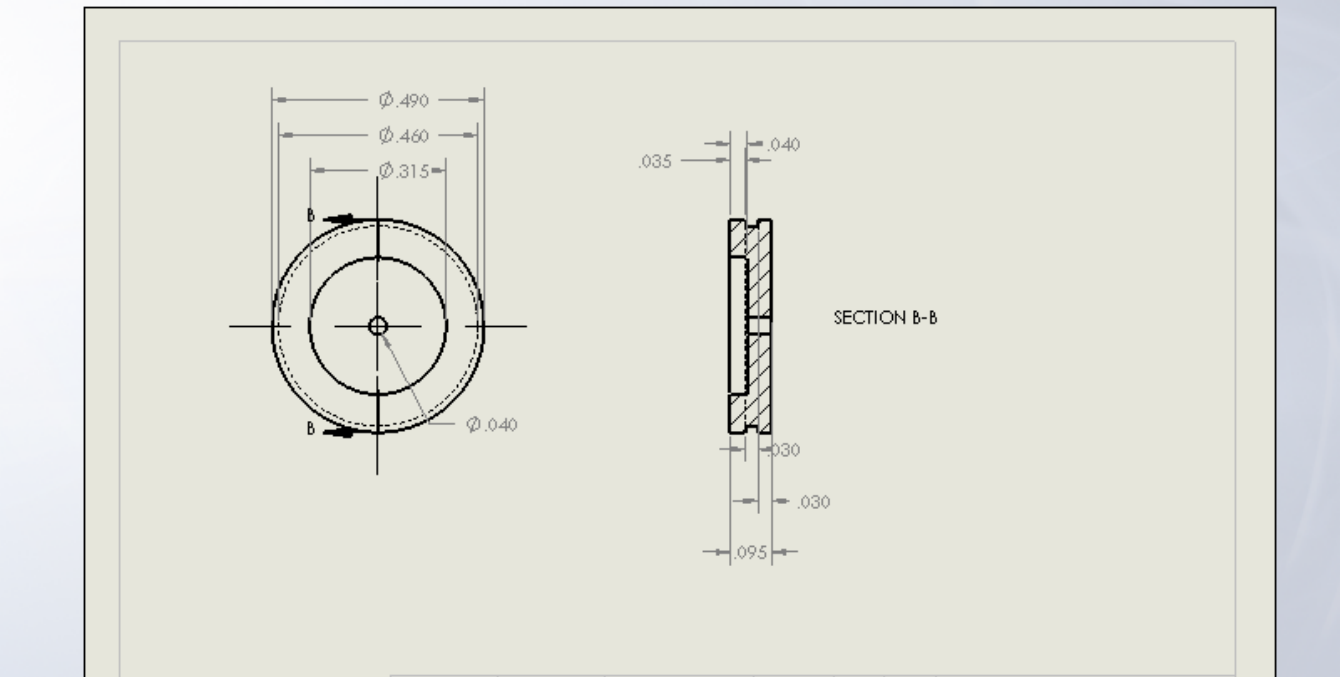

Figure B5. First LMIS extractor cap diaphragm. The dimensions are the same for all other diaphragms in system VII—the only difference being the diameter of the center hole.

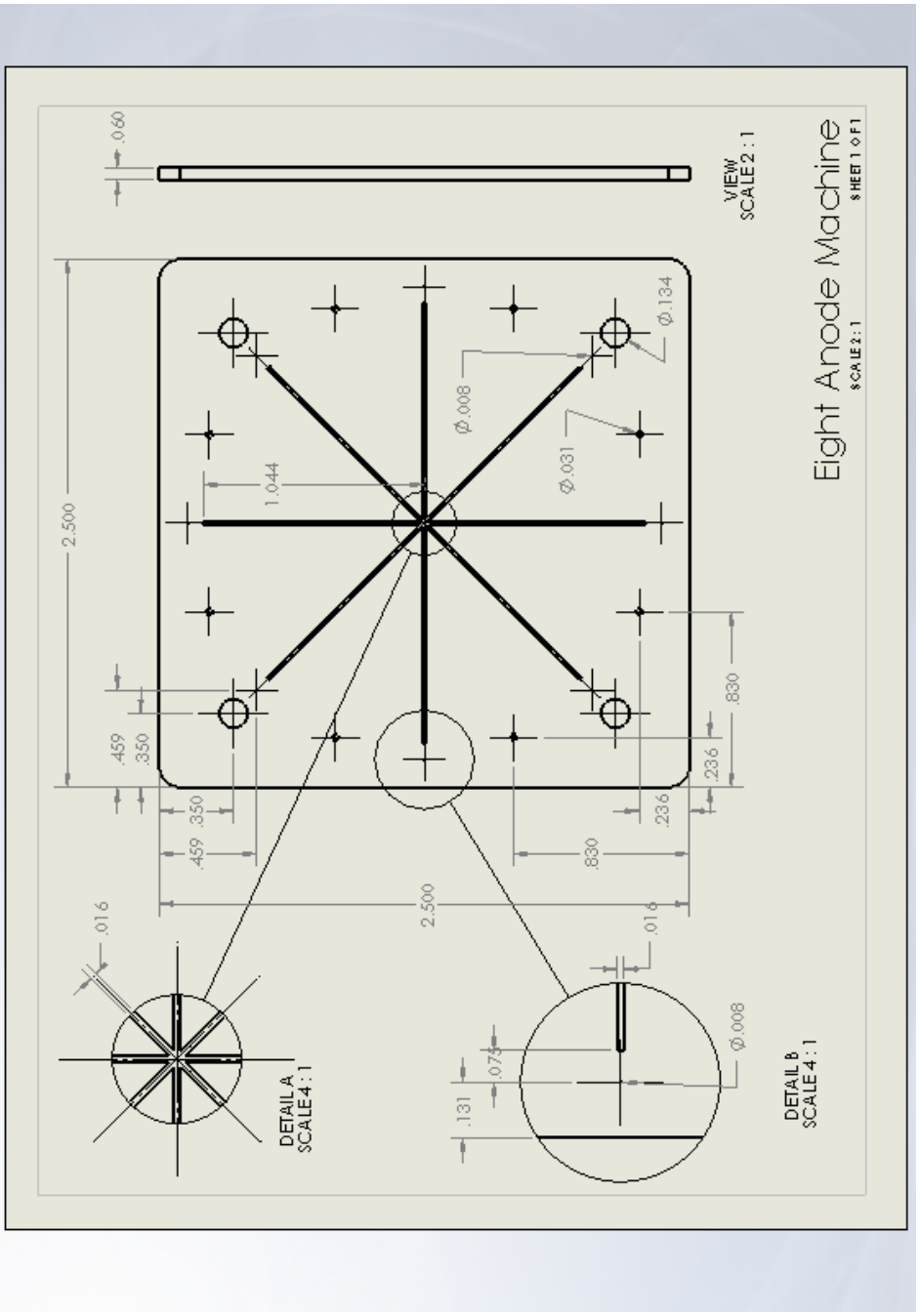

Figure B6. 8-anode detector machined part. Note, this is the current design as of the publication of this dissertation, however it was not used for the acquisition of the data presented here.

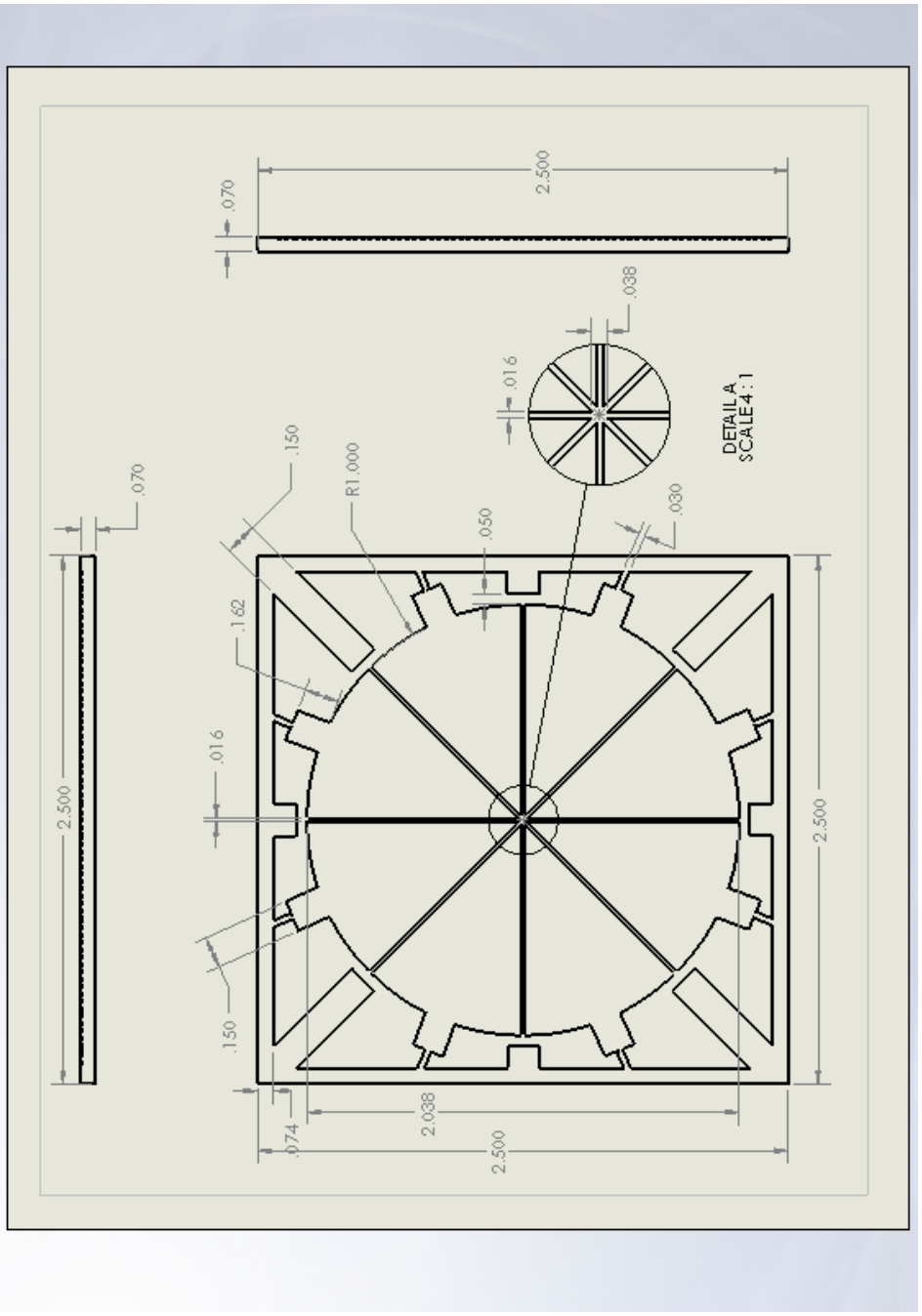

Figure B7. 8-anode detector total part diagram.

VITA

Name:	Veronica Tiffany Pinnick
Address:	Center for Chemical Characterization and Analysis (CCCA) Teague Building—Room G21 Texas A&M University College Station, Texas 77843-3144
Email Address:	VeronicaPinnick@gmail.com
Education:	B.A., Chemistry, Minot State University, 2004 Ph.D., Chemistry, Texas A&M University, 2009